

A Feasibility Study of the ($^3\text{He}, ^8\text{He}$) reaction with the K600 Magnetic Spectrometer

Jacobus Andreas Swartz



Thesis presented in partial fulfilment of the requirements for the Degree of Master of Science at
the University of Stellenbosch
Supervisor: Dr P. Papka
Co-supervisor: Dr R. Neveling
March 2010

Declaration

By submitting this thesis electronically, I declare that the entirety of the work contained therein is my own, original work, that I am the authorship owner thereof (unless to the extent explicitly otherwise stated) and that I have not previously in its entirety or in part submitted it for obtaining any qualification.

.....

Signature

.....

Date

Copyright 2010 Stellenbosch University

All rights reserved

ABSTRACT

Highly exotic nuclei can be studied in rare reactions using stable beams, with macroscopic intensities, and thick targets. Exotic nuclei are interesting for a number of reasons e.g. for testing nuclear models under conditions of high isospins. In the case of very neutron-deficient nuclei, two-proton decay is the most recently discovered nuclear decay mode and the subject of many theoretical investigations involving cluster and shell models.

This thesis presents a feasibility study of investigating light exotic nuclei near the proton drip line with the K600 magnetic spectrometer. The $^{27}\text{Al}(^3\text{He},^8\text{He})^{22}\text{Al}$ five-neutron pick-up reaction was investigated at a spectrometer angle of $\theta_{lab} = 8^\circ$ with a beam energy of $E_{lab} = 220$ MeV. This reaction can be used to populate highly neutron-deficient nuclei. Should the study of this reaction prove to be feasible, then a number of nuclei on the proton drip line or beyond could be investigated. A new data acquisition system, with VME electronics and MIDAS software, was used along with one new drift chamber, which consists of both an X wire plane and a U wire plane. The particles $^1,2,3\text{H}$ and $^3,4\text{He}$ were all identified as outgoing particles from the collision of ^3He with ^{27}Al . Cross section calculations were performed for these observed reactions. Discrete spectra for the $(^3\text{He},^6\text{He})$ and $(^3\text{He},^8\text{He})$ reactions could not be identified.

The mass calculation of $A \sim 20$ nuclei on the proton drip line depends on the determination of the Coulomb energy, which differs a lot between mirror nuclei. Mass calculations were performed for known nuclei in the mass region $A \leq 50$, using the Isobaric Multiplet Mass Equation. Agreement with experimental data was found to be far better in odd nuclei than in even nuclei. Hence mass predictions were performed for odd nuclei along the proton drip line.

OPSOMMING

Hoogs eksotiese kerne kan bestudeer word in seldsame reaksies deur middel van stabiele bundels, met makroskopiese intensiteite, en dik teikens. Eksotiese kerne is interessant om verskeie redes, onder andere om kernfisiese modelle te toets onder omstandighede van hoë isospin. In die geval van baie neutron-arm kerne is twee-proton verval die nuutste ontdekte tipe van kernverval. Dit is ook die onderwerp van vele teoretiese studies met betrekking tot bondel en skilmodelle.

Hierdie tesis beskryf 'n uitvoerbaarheidstudie vir die ondersoek van ligte eksotiese kerne naby die proton drup lyn met behulp van die K600 magnetiese spektrometer. Die $^{27}\text{Al}(^3\text{He}, ^8\text{He})^{22}\text{Al}$ vyf-neutron kaapreaksie is ondersoek by 'n spektrometer hoek van $\theta_{lab} = 8^\circ$ met 'n bundel energie van $E_{lab} = 220$ MeV. Sou die uitvoerbaarheidstudie van hierdie reaksie slaag, dan kan verskeie kerne op of anderkant die proton drup lyn ondersoek word. 'n Nuwe data verkrygingsstelsel, met VME elektronika en MIDAS sagteware, is gebruik saam met een nuwe dryfkamer, wat bestaan uit beide 'n X draadvlak en 'n U draadvlak. Die partikels $^{1,2,3}\text{H}$ en $^{3,4}\text{He}$ is almal geïdentifiseer as uitgaande partikels van die botsing van ^3He met ^{27}Al . Kansvlak-berekening is uitgevoer vir alle waargenome reaksies. Diskrete spektra kon nie gevind word vir die $(^3\text{He}, ^6\text{He})$ of $(^3\text{He}, ^8\text{He})$ reaksies nie.

Die massa berekening van $A \sim 20$ kerne op die proton drup lyn is afhanklik van die bepaling van die Coulomb energie, wat baie verskil tussen spieëlkerne. Massa berekeninge is uitgevoer vir bekende kerne in die massa gebied $A \leq 50$, deur die gebruik van die Isobariese Multiplet Massa Vergelyking. Die ooreenstemming met eksperimentele data was baie beter in die geval van onewe kerne as met ewe kerne. Daarom was die massa voorspellings uitgevoer vir slegs onewe kerne naby die proton drup lyn.

Acknowledgements

I would like to express my sincere gratitude towards

- The National Research Foundation and iThemba LABS for providing me with funding.
- iThemba LABS for allocating beam time to this project.
- My supervisors: Paul Papka and Retief Neveling. Their guidance in all the aspects of this arduous endeavour has been truly invaluable. Merci beaucoup! Baie dankie vir alles!
- The rest of the spectrometer team, especially those who were there for that epic experimental weekend: Ricky Smit, Siegie Förtsch, Iyabo Usman, Joele Mira and Zinhle Buthelezi.
- All my good friends from the eastern and western corners of my little world who have kept me ever within the “Valley of Stability” (see chapter 1).
- My ouers Pierre en Riana Swartz vir al die jare se liefde en ondersteuning.
- My grootouers Koos en Maryna Nel vir hul waardevolle ondersteuning hier in die Kaap.
- Meine schönsten Freundin, Estée Keyser, wie net so ‘n moeilike pad soos ek met hierdie tesis moes stap.
- The Lord God omnipotent, creator of all things bright and beautiful, wise and wonderful, stable and exotic.

Die spektrometer ken 'n proton
Veel beter as 'n Helium isotoop
Maar op 'n dag voel ons toe genoop
Om die fyn masjien daarmee te doop
En Aluminium te stroop
Vyf-neutron oordrag
Is wat ons wou vermag
'n Naweek gaan toe oop
Met die bundel aan die loop
Dag en nag het ons verwoed gejag
En uitgek...by een-neutron oordrag

CONTENTS

ABSTRACT	3
LIST OF TABLES	iv
LIST OF FIGURES	vi
1. Introduction	1
1.1 Exotic nuclei	1
1.2 About the experiment	8
1.3 Previous experiments with stable He beams	9
2. Mass predictions	12
2.1 The isobaric multiplet mass equation	12
2.2 The mass prediction code	15
2.3 Results of mass predictions	16
2.3.1 Calculations for $A = 19$ isobars	16
2.3.2 Calculations for $A = 22$ isobars	17
2.3.3 Calculations for $A = 43$ isobars	18
2.3.4 Calculations for $A = 45$ isobars	19
2.3.5 Calculations and predictions along the proton drip line	19
3. The Experiment	24
3.1 The particle beam and targets	24
3.2 The K600 magnetic spectrometer	26
3.3 The focal plane detector package	29
3.3.1 The vertical drift chamber	29
3.3.2 VDC design considerations	30
3.3.3 VDC construction	31
3.3.3.1 Stesalit chassis	31
3.3.3.2 Sense region	32
3.3.3.3 Printed circuit board	35
3.3.3.4 Wires	35
3.3.3.5 High voltage planes	37
3.3.3.6 Drift chamber gas	37
3.3.3.7 Sealing	37
3.3.4 Paddle scintillators	39
3.4 Electronics	41

3.4.1	Paddle signals	41
3.4.2	Dead time measurement	42
3.4.3	Pre-amplifier cards and TDCs	42
3.4.4	Current integration	42
3.5	Data acquisition	44
3.6	Experimental procedure	44
4.	Data analysis	47
4.1	Methods of particle identification	47
4.2	VDC operation	48
4.2.1	Determining the focal plane position	49
4.2.2	Vertical position determination	50
4.2.3	Position resolution	51
4.2.4	The lookup table shift	53
4.2.5	VDC efficiency	54
4.2.6	The position spectrum	56
4.3	Analysis of different fieldsets	57
4.3.1	Analysis of the $^{27}\text{Al}(^3\text{He},^3\text{He})^{27}\text{Al}$ fieldset	57
4.3.2	Analysis of the $^{27}\text{Al}(^3\text{He},d)^{28}\text{Si}$ fieldset	68
4.3.3	Analysis of the $^{27}\text{Al}(^3\text{He},t)^{27}\text{Si}$ fieldset	73
4.3.4	Analysis of the $^{27}\text{Al}(^3\text{He},^4\text{He})^{26}\text{Al}$ fieldset	78
4.3.5	Analysis of the $^{27}\text{Al}(^3\text{He},^6\text{He})^{24}\text{Al}$ fieldset	85
4.3.5.1	Paddles perpendicular to the beam	86
4.3.5.2	Paddles parallel to the VDC	90
4.3.6	Analysis of the $^{27}\text{Al}(^3\text{He},^8\text{He})^{22}\text{Al}$ fieldset	93
5.	Conclusion	99
6.	Bibliography	101

LIST OF TABLES

2.1	Calculations for the $A = 19$ isobars	16
2.2	Calculations for the $A = 22$ isobars	18
2.3	Calculations for the $A = 43$ isobars	19
2.4	Calculations for the $A = 45$ isobars	19
2.5	Calculations of odd nuclei along the proton drip line	21
2.6	Calculations of even nuclei along the proton drip line	22
2.7	Predictions of nuclei that have not yet been measured	23
3.1	The current settings which were applied to the magnets in order to produce the optimal magnetic fields for each particle	46
4.1	TOF and rigidity calculations for the ^3He fieldset	59
4.2	A summary of the materials seen in the focal plane by the particles exiting the K600 vacuum chamber	59
4.3	A summary of the calculated energy loss of various particles determined by the rigidity calculations of Table 4.1	61
4.4	The known experimental excitation energy values of the energy levels of ^{27}Al are matched to the positions of the discrete experimental peaks	65
4.5	TOF and rigidity calculations for the d fieldset	68
4.6	A summary of the calculated energy loss of various particles determined by the rigidity calculations of Table 4.5	68
4.7	The known experimental excitation energy values of the energy levels of ^{28}Si are matched to the positions of the discrete experimental peaks	71
4.8	TOF and rigidity calculations for the t fieldset	73
4.9	A summary of the calculated energy loss of various particles determined by the rigidity calculations of Table 4.8	73
4.10	The known experimental excitation energy values of the energy levels of ^{27}Si are matched to the positions of the discrete experimental peaks	76
4.11	TOF and rigidity calculations for the α fieldset	78
4.12	A summary of the calculated energy loss of various particles determined by the rigidity calculations of Table 4.11	78

4.13	The known experimental excitation energy values of the energy levels of ^{26}Al are matched to the positions of the discrete experimental peaks	82
4.14	TOF and rigidity calculations for the ^6He fieldset	85
4.15	A summary of the calculated energy loss of various particles determined by the rigidity calculations of Table 4.14	85
4.16	TOF and rigidity calculations for the ^8He fieldset	93
4.17	A summary of the calculated energy loss of various particles determined by the rigidity calculations of Table 4.16	94

LIST OF FIGURES

1.1	A section of the neutron-deficient side of the chart of nuclides illustrating the five-neutron transfer reaction that was investigated	2
1.2	The chart of all discovered nuclides [1]	4
1.3	A section of the chart of nuclides [1] illustrating some of the possible future 5-neutron transfer channels from stable nuclei	7
1.4	Position spectra from the $^{64}\text{Ni}(^3\text{He},^8\text{He})^{59}\text{Ni}$ experiment at Princeton [2]	10
2.1	Energy level scheme of two uneven A mirror nuclei	13
2.2	Plot of $E_c^{(0)}$ vs Z for mass calculation of ^{19}Mg	17
2.3	Plot of $E_c^{(0)}$ vs Z for mass calculation of ^{22}Al	17
2.4	Plot of $E_c^{(0)}$ vs Z for mass calculation of ^{43}Cr	18
2.5	Plot of $E_c^{(0)}$ vs Z for mass calculation of ^{45}Fe	20
2.6	Plot of deviation from experimentally measured values for mass calculations of odd nuclei.	22
2.7	Plot of deviation from experimentally measured values for mass calculations of even nuclei.	23
3.1	Floor-plan of the cyclotron facility	25
3.2	A schematic overview of the K600 magnetic spectrometer	28
3.3	Schematic overview of the HiP side of the new VDC design	31
3.4	Autocad image of the assembled new VDC	32
3.5	Top view of U-X wire chamber	33
3.6	Side view of U and X wires illustrating their different coordinate systems	33
3.7	GARFIELD models of the magnitude of the equipotential surfaces and the magnitude of the electric field for the VDC sense region	34
3.8	The soldered U-wire plane opened up to display its wires and PCB.	36
3.9	A section of the soldered X-wire plane illustrating the guard wires and the signal wires with their associated signal wire tracks.	36
3.10	The HV stretching procedure	38
3.11	The 1/2" and 1/4" paddle scintillators, illustrating the light guides	40

3.12	One side of a paddle scintillator, wrapped in aluminized mylar	40
3.13	Diagram of the trigger electronics	43
4.1	A two-dimensional PID spectrum for the $^{27}\text{Al}(^3\text{He},^3\text{He})^{27}\text{Al}$ reaction.	48
4.2	TOF spectrum for the $^{27}\text{Al}(^3\text{He},^3\text{He})^{27}\text{Al}$ reaction.	48
4.3	Particle trajectory through U and X planes, illustrating the offset in x between the two wire planes.	51
4.4	Illustration of how the offset in the U plane position u_{offset} , and the vertical position y may be determined	52
4.5	The lookup table.	53
4.6	Position resolution plots illustrating the projection of events on the Δ axis.	54
4.7	Position resolution plots illustrating the projection of Δ on $b - \text{int}(b)$	54
4.8	The raw wire hits per channel	55
4.9	The wire hits per event for both wire planes	55
4.10	The spectrum of all drift times measured by the X-wire plane for the ^4He fieldset	56
4.11	The horizontal focal plane position spectrum for the ^3He beam on the ^{27}Al target without any PID selection gates	56
4.12	PID spectra for the ^3He fieldset	58
4.13	The relative light outputs of different particles	60
4.14	The calculated and experimental energy-loss vs TOF spectra for the $^{27}\text{Al}(^3\text{He},^3\text{He})^{27}\text{Al}$ reaction	62
4.15	The calculated and experimental Paddle 1 vs Paddle 2 spectra for the $^{27}\text{Al}(^3\text{He},^3\text{He})^{27}\text{Al}$ reaction	63
4.16	Experimental focal plane position spectra for the ^3He fieldset	64
4.17	The energy calibration curve plotted from the observed ^{27}Al spectrum	66
4.18	The double differential cross section of the $^{27}\text{Al}(^3\text{He},^3\text{He})^{27}\text{Al}$ reaction	67
4.19	Calculated and experimental PID spectra for the d fieldset	69
4.20	Experimental focal plane position spectra for the d fieldset	70
4.21	The energy calibration curve plotted from the observed ^{28}Si spectrum	72
4.22	The double differential cross section of the $^{27}\text{Al}(^3\text{He},d)^{28}\text{Si}$ reaction	72
4.23	Calculated and experimental PID spectra for the t fieldset	74

4.24	Experimental focal plane position spectra for the t fieldset	75
4.25	The energy calibration curve plotted from the observed ^{27}Si spectrum	77
4.26	The double differential cross section of the $^{27}\text{Al}(^3\text{He},t)^{27}\text{Si}$ reaction	77
4.27	Calculated and experimental PID spectra for the ^4He fieldset	80
4.28	Experimental focal plane position spectra for the $^{27}\text{Al}(^3\text{He},^4\text{He})^{26}\text{Al}$ and $^{27}\text{Al}(^3\text{He},p)^{29}\text{Si}$ reactions	81
4.29	The energy calibration curve plotted from the observed ^{26}Al spectrum	83
4.30	The double differential cross section of the $^{27}\text{Al}(^3\text{He},^4\text{He})^{26}\text{Al}$ reaction	83
4.31	The double differential cross section of the $^{27}\text{Al}(^3\text{He},p)^{29}\text{Si}$ reaction	84
4.32	Calculated and experimental PID spectra for the 196 MeV ^6He fieldset	87
4.33	The experimental PID and position spectra for events that fall within the TOF gate in Fig. 4.32	88
4.34	The experimental PID and position spectra for events that do not fall within the TOF gate in Fig. 4.32	89
4.35	Calculated and experimental PID spectra for the 202 MeV ^6He fieldset	91
4.36	The experimental PID and position spectra for events that fall within the TOF gate in Fig. 4.35	92
4.37	Calculated and experimental PID spectra for the ^8He fieldset	95
4.38	PID spectra with TOF and paddle gates to select the most likely candidate for the $^{27}\text{Al}(^3\text{He},^8\text{He})^{22}\text{Al}$ reaction	96
4.39	Experimental position spectrum measured in TOF and paddle range where the $^{27}\text{Al}(^3\text{He},^8\text{He})^{22}\text{Al}$ reaction was expected.	96
4.40	The PID selection gates which were investigated for the ^8He fieldset	98

CHAPTER 1

Introduction

The study of exotic nuclei, which are situated far from the line stability on the chart of nuclides, is one of the most important topics of research in modern-day nuclear physics, with applications in fields such as nuclear structure and nuclear astrophysics. In studying light ($A \leq 50$) exotic nuclei, multi-nucleon transfer is a very useful reaction mechanism. This thesis considers five-neutron transfer as a tool to study light exotic nuclei, specifically along the proton drip line.

The $^{27}\text{Al}(^3\text{He},^8\text{He})^{22}\text{Al}$ reaction, which is illustrated on the chart of nuclides [1] by the red arrow in Fig. 1.1, was investigated experimentally. The aim of this study was to test the feasibility of using the iThemba LABS K600 magnetic spectrometer to perform experiments using five-neutron pick-up reactions with stable ^3He beams on nuclei in a mass region of $A \leq 50$. In the past, the experimental measurement of the $(^3\text{He},^8\text{He})$ reaction has been successfully performed only once [2].

This chapter begins with an overview of the physics of exotic nuclei and the study thereof in section 1.1, and then gives a short description of the experiment in section 1.2. The chapter is concluded with section 1.3, which briefly describes some previous experiments that were performed with stable He beams and similar objectives.

Chapter 2 describes some mass predictions which were performed for nuclei which have as yet not been measured around the proton drip line. Chapter 3 describes the experimental setup and procedure. Chapter 4 describes the data analysis and Chapter 5 provides a conclusion.

1.1 Exotic nuclei

In the very light mass region of $A \leq 20$, the number of protons and neutrons in stable nuclei are about equal. In heavier nuclei, the proportion of neutrons in stable nuclei becomes progressively greater, as can be seen from Fig. 1.2. There exists a tendency in nuclei to have a completed pair of nucleons of some kind [3]. This tendency, as well as the tendency of the number of neutrons to be equal to the number of protons, may be attributed to the existence of nuclear energy levels [4]. Nucleons are a subset of fermions, which are particles of half-integer spins that obey the Pauli Exclusion Principle, and as a result each energy level may be occupied by two neutrons of opposite spins and two protons of opposite spins. Energy levels in nuclei are filled in sequence to achieve configurations of minimum energy and maximum stability. A nucleus with an excess of neutrons or protons will generally have a higher mass excess and less stability. Such nuclei

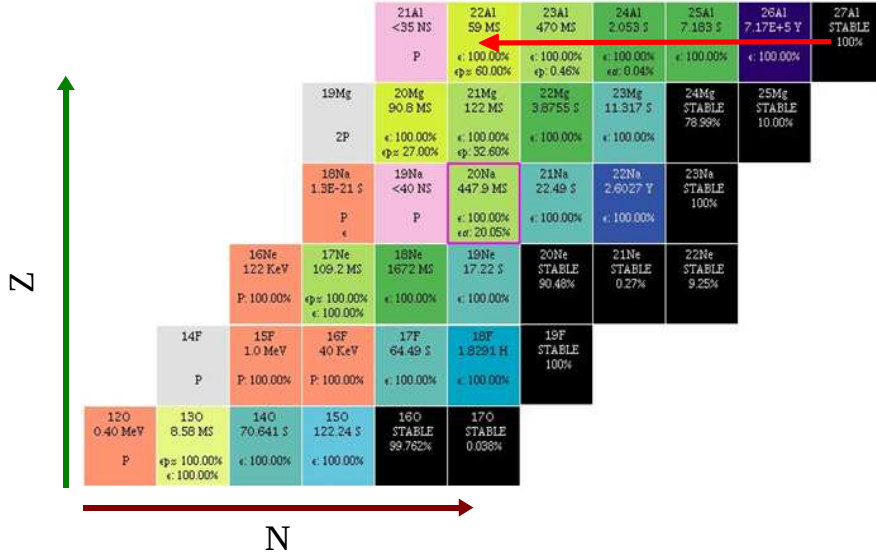
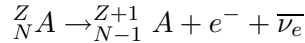
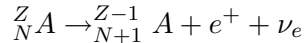


FIG. 1.1: A section of the neutron-deficient side of the chart of nuclides near the five-neutron transfer reaction that was investigated. The $^{27}\text{Al}(^3\text{He}, ^8\text{He})^{22}\text{Al}$ reaction, which was investigated experimentally in this feasibility study, is indicated by the bright red arrow.

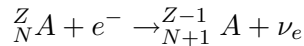
tend to move back to the bottom of the “Valley of Stability” in Fig. 1.2 by negative β -decay



from the neutron-rich side, and by positive β -decay



or electron capture



from the neutron-deficient (or proton-rich) side. Negative β -decay is illustrated on the chart of nuclides by the orange arrow in Fig. 1.3, while positive β -decay or electron capture may be represented by the yellow arrow in the same figure. The reason for the greater number of neutrons in stable heavy nuclei is the effect of the Coulomb repulsion between protons. In nuclei with $Z \geq 10$ this repulsion becomes too great and an excess of neutrons is required to maintain

stability. The excess of neutrons contributes to the attractive strong interaction between nucleons and moderates the Coulomb repulsion between the protons. This effect also accounts for the fact that there are more neutron-rich than neutron-deficient nuclear species.

About 60% of stable nuclides have both even Z and even N . They are known as even-even nuclei. The majority of the rest have either even Z and odd N (even-odd nuclides) or odd Z and even N (odd-even nuclides), with the numbers of the two kinds being almost the same. There are only five odd-odd nuclei that are known to be stable: ${}^2\text{H}$, ${}^6\text{Li}$, ${}^{10}\text{B}$, ${}^{14}\text{N}$ and ${}^{180}\text{Ta}$ which are mostly very light nuclei [4]. Nuclei with filled energy levels are far more abundant than the ones without.

The idea of nuclear energy levels is analogous to that of atomic energy levels. In atomic physics, atoms with 2, 10, 18, 36, 54 and 86 electrons have all their electron shells completely filled and therefore have high binding energies and stability. Nuclei with certain special numbers of protons or neutrons, namely 2, 8, 20, 28, 50, 82 and 126, are more abundant than other nuclei with similar masses, suggesting that their structures are more stable and that an effect similar to that of electron shells in atoms is also present in nuclei with nuclear shells. Furthermore, nuclei with these so-called “magic numbers” have been found to have zero nuclear electric quadrupole moments. The quadrupole moment of a nucleus is a measure of how far its charge distribution departs from sphericity. Hence a magic number nucleus may be expected to have a spherical shape. A nucleus shaped like a rugby ball (prolate) has a positive quadrupole moment and one shaped like a pumpkin (oblate) has a negative moment.

The nuclear shell model arose as an attempt to account for the magic numbers and certain other nuclear properties in terms of nucleon behaviour in a common force field. It describes the nucleus in terms of levels with increasing energies, with the outermost level determining most of the properties of the nucleus.

The regions on the chart of nuclides where the proton and neutron separation energies equal zero delineate the proton and neutron drip lines. While only 263 stable isotopes exist, the heaviest of which is ${}^{209}\text{Bi}$, there are another approximately 3 000 unstable isotopes which have been observed and 7 000 unstable isotopes which have been predicted to exist between these drip lines [5].

Nuclei in the vicinity of these drip lines are known as drip-line or exotic nuclei. Along the drip lines, the usual Z and N numbers corresponding to closed shells do not always exhibit the expected nuclear properties. The effect of shell quenching occurs in these drip-line nuclei, which necessitates that the shell model must be revised at times to incorporate new magic numbers for such cases.

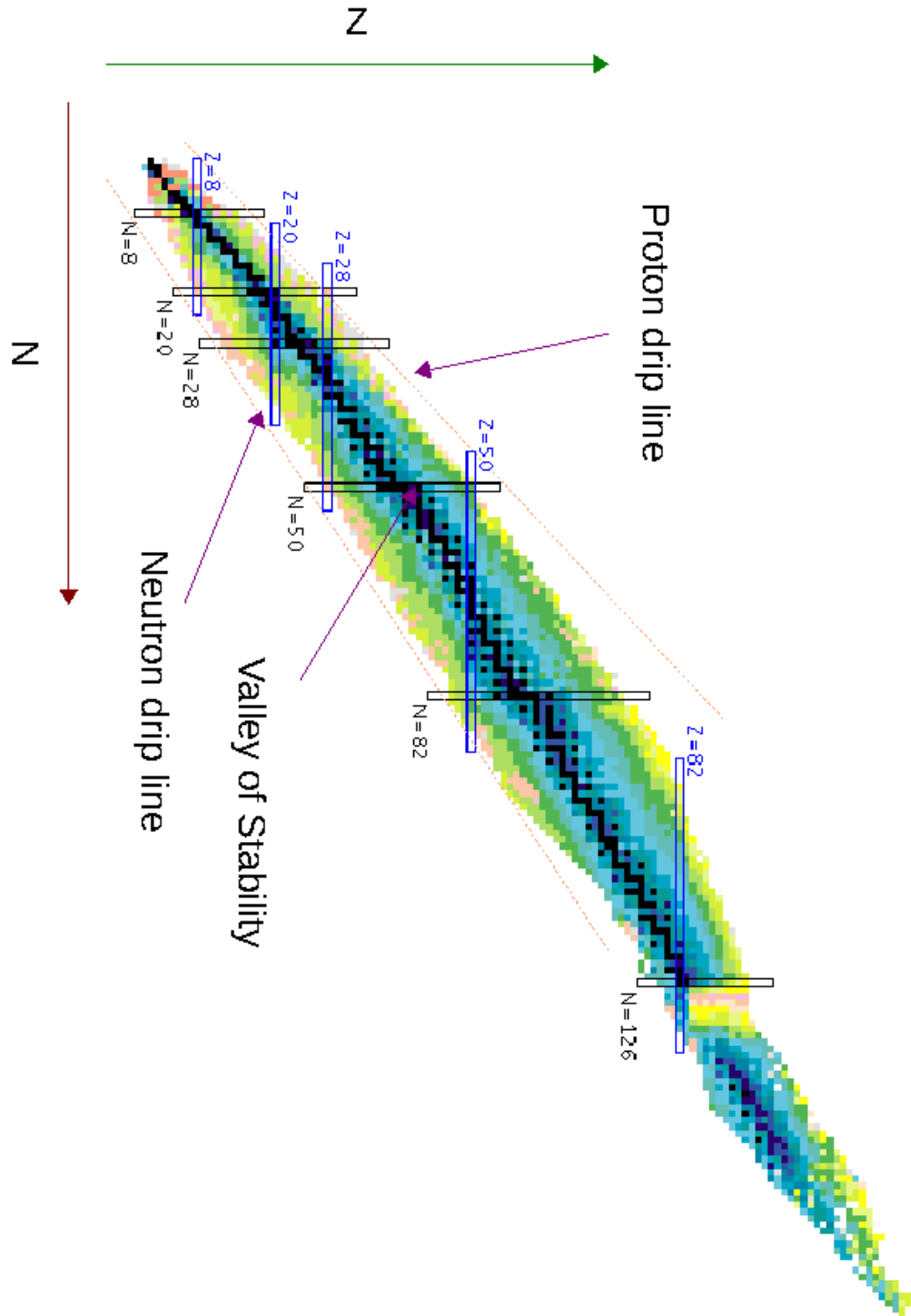
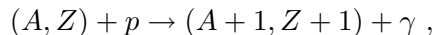
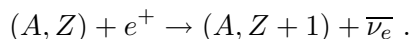


FIG. 1.2: The chart of all discovered nuclides [1]. The black squares represent stable isotopes which form the bottom of the Valley of Stability, also known as the line of β -stability. The orange lines represent the proton and neutron drip lines which are at the ends of the Valley of Stability. The blue rectangles indicate regions of proton shell closure and the black rectangles indicate regions of neutron shell closure.

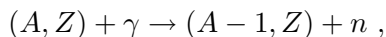
Exotic nuclei are not naturally found on earth since they are highly unstable to β -decay. In nature, they are formed mainly in astrophysical processes such as the rapid r - and the slow s -neutron capture processes on the neutron-rich side. The β^- -decay which follows neutron capture must stop at the line of β -stability, therefore it will not form neutron-deficient nuclei. Possible reactions for the formation of neutron-deficient nuclei include the (p, γ) reaction by which the rp -process functions:



and positron capture:



Other possibilities for the formation of neutron-deficient nuclei are the (γ, n) reactions which occur in the p -process:



and spallation of heavier nuclei by a proton or an α -particle [6].

By measurement of the masses, half-lives and decay energy levels of drip line nuclei with high isobaric spins (isospins), valuable information is gained pertaining to existing nuclear models and to nuclear astrophysical processes, such as the r - and rp -processes, which generate energy in stars and contribute to the nucleosynthesis of the elements in the universe [7].

Advances in particle accelerators and experimental techniques have been beneficial to the study of the physics of nuclei lying far from the line of β -stability. Such studies have provided scientists with insight into the properties of nuclei with extreme Z/N ratios [8], and have pushed the frontier of knowledge about nuclei further away from the line of β -stability to regions nearer to the proton and neutron drip lines. Producing and identifying such nuclei is difficult from an experimental point of view, but reaction mechanisms such as deep inelastic heavy ion reactions [9, 10, 11, 12, 13], multi nucleon transfer reactions [14, 15], fusion evaporation reactions [16] and, most of all, the use of radioactive ion beams (RIBs) [17], along with the appropriate beam energies and intensities, have acted as efficient probes of exotic nuclei.

The continuing investigations of highly unstable nuclei provide not only a test for nuclear models, but also a window through which profound structural effects may be observed. One example of this is the onset of prolate deformation which was found along the magic number line $N = 20$ around the neutron-rich isotones ^{31}Na and ^{32}Mg . Here, one would normally expect to find a spherical shape for the ground state due to the completion of the $N = 20$ closed shell [18, 19, 20], but $N = 20$ is no longer a “magic number” for such neutron-rich nuclei. This came as a surprise since this deformation could not have been predicted from what was known about

other nearby nuclei lying closer to β -stability [8].

Another example of a profound nuclear structure effect seen in exotic nuclei is that of halo nuclei which have been observed in a number of cases near the neutron drip line. Examples include ^{11}Be which has a one-neutron halo, ^{17}B and ^6He which have two-neutron haloes, and ^8He which has a four-neutron halo [5, 21]. Such nuclei are broken up into a core system A , and a neutron halo system which extends radially very far from the core. For a two-neutron halo nucleus, one may plot the strength of the neutron-neutron interaction V_{nn} against the strength of the interaction between the core A and each neutron V_{An} . This plot is separated by a line for each two-body system nn and An , above which they are bound and below which they are unbound. The region beneath both of these lines may be split into two parts:

- One where none of the two-body systems nor the three-body system is bound, and
- one where none of the two-body systems are bound, but the three-body system is bound.

The last mentioned region is known as the Borromean region, and a nucleus for which such a region may be found is known as a Borromean nucleus [5]. Examples of Borromean two-neutron halo nuclei include ^6He and ^{11}Li [21].

Due to the presence of the Coulomb barrier, halo nuclei are less prevalent near the proton drip line. Nevertheless, there are candidates such as ^8B and ^{17}F for one-proton halo nuclei, and ^{17}Ne and ^6Be , which is the mirror nucleus of ^6He , for two-proton halo nuclei [5].

The determination of the masses of drip-line nuclei provide a quantitative test for our understanding of nuclear binding and nuclear structure [8]. This information is of relevance to various nuclear phenomena which were mentioned earlier in this section, and to the testing of current mass models. Defining the ground state mass of a nucleus consists of locating its ground state and measuring its energy, therefore of finding its mass excess. The masses of many proton-rich nuclei along the proton drip line have not been determined yet, whereas, in almost all cases, their neutron-rich mirrors have well-determined masses [22]. The mass calculation of light ($A \approx 20$) nuclei on the proton drip line depends heavily on the determination of the Coulomb energy, which differs a great deal between mirror nuclei. There exists much disagreement between the existing models which are used to predict the masses of drip-line nuclei. All of them still show divergence from experimental data at certain intervals and specific regions on the nuclear mass surface [23, 24, 25, 26]. Hence mass calculations are performed in Chapter 2 for nuclei in the vicinity of the proton drip line.

Along the drip lines, direct nucleon or dinucleon emission is an important field of study. Many of these decay processes provide nuclear structure information that cannot be obtained in other

way [8]. In the case of the proton drip line, one-proton emission is a known mode of decay, and two-proton ($2p$) radioactivity specifically is the most recently discovered nuclear disintegration mode [27]. It was reported to have been observed for the first time in 2002, more than 40 years after it was predicted for a number of proton-rich isotopes that lie beyond the proton drip line [28]. The observed emission was from ^{45}Fe with a half-life of $T_{1/2} = 4$ ms, which is about a thousand times longer than the quasiclassical estimate of di-proton emission [29, 30]. It has since been observed in isotopes such as ^{19}Mg , ^{54}Zn , ^{94}Ag and most recently in ^6Be [27, 31, 32, 33]. Two-proton emission is a subject of many theoretical studies involving cluster and shell models [22, 27, 34, 35, 36].

The proton drip line lies much closer to the nearest β -stable isotope of each element than does the neutron drip-line as one can see from Fig. 1.2. This is due to the increased Coulomb energy that arises from the addition of each proton to a nucleus. This proximity makes it experimentally easier to reach the proton drip line, but the fact that proton (or two-proton) emission can be significantly delayed by the Coulomb barrier makes the true establishment of the proton drip line more difficult [8].

1.2 About the experiment

Fusion evaporation involving compound nucleus formation and the subsequent evaporation of neutrons is the most often used reaction mechanism for populating neutron-deficient nuclei in the region of heavy nuclei $A \geq 100$. In the kind of fusion evaporation that is referred to, a compound nucleus is produced in which the identities of the projectile and the target are lost. Residues are then produced by the evaporation of light particles from the highly excited compound nucleus. This reaction mechanism may be used to populate neutron-deficient nuclei with stable beams and targets in mass regions where the cross sections are high for evaporating only neutrons. In the region of $A \leq 50$, however, the light charged particles are not strongly bound to the nucleus, and so the cross sections for evaporating only neutrons tend to zero as one approaches the proton drip line [8, 35, 37].

On the other hand, nuclei in the vicinity of the proton drip line in the mass region $A = 15-30$ have been investigated extensively by deep inelastic scattering and beam fragmentation via β -decay starting from the residues [35]. The deep inelastic (DI) scattering referred to involves two nuclei having a grazing collision, which means that the overlap of the ions is much less than in the case of fusion reactions. Nevertheless, it is sufficient to produce a strong interaction between the two nuclei which transforms a significant amount of the kinetic energy into internal excitation energy [38]. This is not the High Energy type of DI scattering, which may be used to probe the

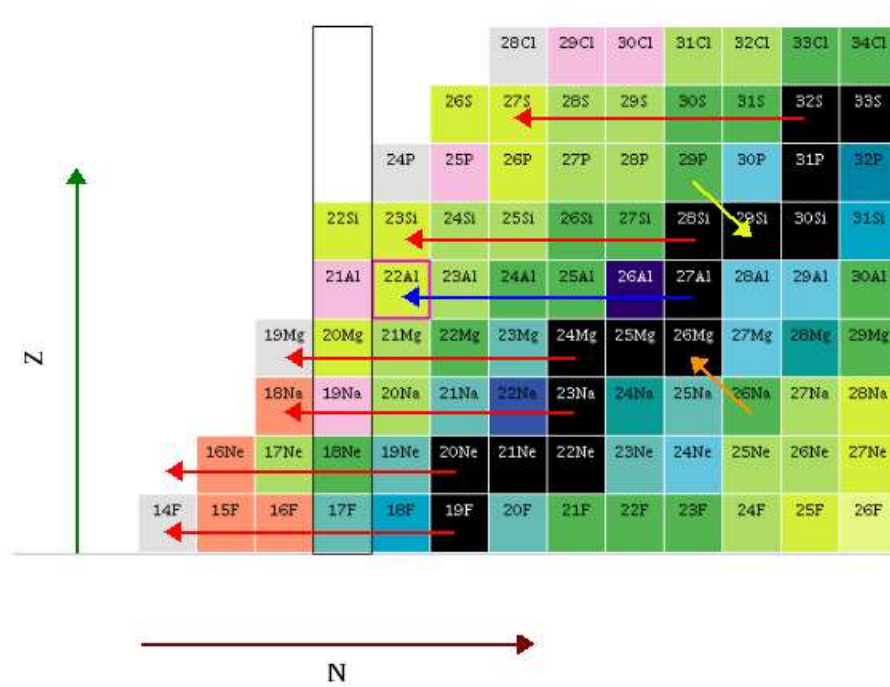


FIG. 1.3: A section of the chart of nuclides [1] illustrating some of the possible future 5-neutron transfer channels from stable nuclei with the red arrows. The blue arrow indicates the $^{27}\text{Al}(^3\text{He}, ^8\text{He})^{22}\text{Al}$ reaction. The yellow arrow indicates either β^+ -decay wherein a proton is converted into a neutron, or electron capture where a proton absorbs an electron. The orange arrow indicates β^- -decay wherein a neutron is converted into a proton.

structure of nucleons.

Beam fragmentation refers to the process where the projectile nucleus undergoes nuclear collision with the target nucleus and is broken apart into several daughter nuclei. These residual daughter nuclei emerge from the target with a momentum similar to that of the projectiles, while the target nuclei fragments have much lower energies and therefore do not travel with the beam. The kind of exotic nucleus that this study is concerned with cannot be investigated via the β -decay starting from these residual particles, since it is generally the first bound (if it is bound) nucleus of its isobaric series.

The use of radioactive ion beams (RIBs), obtained from primary beam fragmentation, is generally the most efficient method of populating exotic nuclei. This method has been used to produce many exotic nuclei, especially on the neutron-rich side [8, 17]. Unfortunately, RIBs are not available at iThemba LABS. However, adequate reaction rates may be obtained by using stable beams with macroscopic intensities and exotic reactions, namely multi-nucleon transfer, as was the aim of this study.

The $^{27}\text{Al}(^3\text{He},^8\text{He})^{22}\text{Al}$ reaction was investigated in this study with the K600 magnetic spectrometer at iThemba LABS. A beam of ^3He impinged on a target of ^{27}Al at an incident energy of $E_{lab} = 220$ MeV. Five-neutron pick-up allows us to populate very neutron deficient nuclei. It is therefore considered as a tool for investigating exotic nuclei specifically along the proton drip line.

The ^{22}Al isotope is a highly neutron deficient, and therefore exotic, nucleus. It has a high isobaric spin ($T = 2$) and lies near the proton drip line, so its Z/N ratio is pushed to the limit imposed by nuclear binding [8].

Should the study of the $(^3\text{He},^8\text{He})$ reaction prove to be feasible with an ^{27}Al target, then five-neutron pick-up can be used to study more exotic light nuclei close to or on the proton drip line e.g. $^{4,5}\text{Be}$, $^{5,6}\text{B}$, ^7C , $^{9,10}\text{N}$, ^{11}O , ^{14}F , ^{15}Ne , ^{18}Na , ^{19}Mg , ^{23}Si and ^{27}S . Some of these possible reaction channels are illustrated by Fig. 1.3.

1.3 Previous experiments with stable He beams

The only valid measurement of the $(^3\text{He},^8\text{He})$ reaction to date was performed with a Q3D (one quadrupole and three dipoles) spectrometer at Princeton University in 1977 [2]. A ^{64}Ni target was used, hence the reaction $^{64}\text{Ni}(^3\text{He},^8\text{He})^{59}\text{Ni}$, which has a Q-value of $Q = -22.62$ MeV, was measured.

The experiment was performed with a beam energy of $E_{lab} = 75.3$ MeV. A spectrometer angle of $\theta_{lab} = 10^\circ$ to the beam and the full aperture of 14.5 msr were used. A proportional counter-and-plastic scintillator telescope, as well as a resistive-wire proportional counter, were employed in the focal plane [39]. Each counter was 1.27 cm thick and 20 cm long, and the distance between anodes was 1.27 cm. An additional counter provided both a second energy-loss and a second position signal. The additional position signal was very important since it enabled for the determination of the particle angle through the focal plane. Thus an angle cut could be applied to the focal plane events.

A beam with an intensity of $I_{beam} = 375$ pA impinged on a 1.04 mg/cm² Ni target for a period of 24 hours. An E- Δ E particle identification (PID) spectrum was plotted with the scintillator signal on the y-axis, and the signal from the proportional counter, which was placed downstream of the scintillator, on the x-axis. The scintillator signal was related to particle energy E and the proportional counter signal to energy loss Δ E in this experiment. In this spectrum, the $^6\text{He}^{2+}$, $^3\text{He}^{1+}$ and $^4\text{He}^{1+}$ event-groups stood out clearly from the background and distinctly from one another. The position spectrum of Fig. 1.4 in

- (a) is for all the events which were measured in the PID spectrum.

- (b) is for the events that fall within the window that was predicted for ^8He in the $E-\Delta E$ spectrum, and also within a TOF gate that was set for ^8He .
- (c) is for events that remain after an angle cut is added to all the particle gates in (b).

Already almost all the background events from contaminants in the ^8He spectrum are eliminated in (b). Only eight “true” counts for ^{59}Ni were found in the position spectrum in (c). Six of these events were assigned to the $3/2^-$ ground state and two of them to the $5/2^-$ excited state which occurs at 340 keV. A cross section of $\sigma = 230$ pb/sr was reported.

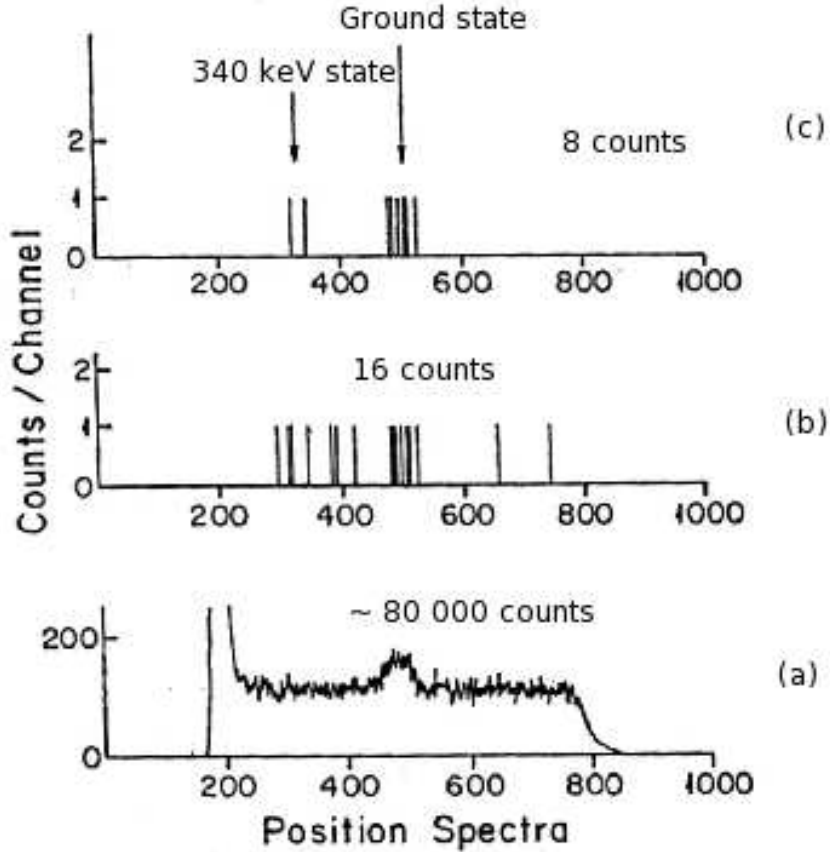


FIG. 1.4: Position spectra from the $^{64}\text{Ni}(^3\text{He}, ^8\text{He})^{59}\text{Ni}$ experiment at Princeton [2]. A position spectrum of all events is shown in (a), with a peak from ^6He particles around channel 500. A position spectrum from events in the ^8He window with a TOF gate is shown in (b). A position spectrum of all true events for ^{59}Ni , which fall within an additional angle gate, is shown in (c).

Targets of ^{58}Ni and ^{50}Ti were also investigated for the $(^3\text{He}, ^8\text{He})$ reaction, and upper limits of $\sigma \leq 35$ pb/sr and $\sigma \leq 100$ pb/sr were set for their cross sections at $\theta_{lab} = 10^\circ$. In the same paper, a work is reported without reference on the $^{27}\text{Al}(^3\text{He}, ^8\text{He})^{22}\text{Al}$ reaction, which has a much larger Q-value ($Q = -52.047$ MeV), at $E_{lab} = 76$ MeV with $\theta_{lab} = 10^\circ$. The measurement was

unsuccessful, but an upper limit of $\sigma \leq 50$ pb/sr could be set on the cross section. The beam energy was very low compared to the Q-value, so one could expect a relatively low cross section compared to a high background due to the low recoil energy of the ^8He [35].

It was concluded in Ref. [2] that higher ^3He beam energies (150-200 MeV) might significantly increase the cross section of the ($^3\text{He},^8\text{He}$) five-neutron pick-up reaction so it may be used to determine the masses of various neutron-deficient nuclei.

The ($^3\text{He},^6\text{He}$) three-neutron pick-up reaction has been successfully measured and used on occasions [40, 41] to populate light exotic nuclei such as ^4Li and ^{11}N , while the ($^4\text{He},^8\text{He}$) four-neutron pick-up reaction has been used to populate nuclei such as ^9C , ^8C , ^{20}Mg and ^{24}Si [14, 15, 42, 43]. In a recent experiment, the ($^4\text{He},^8\text{He}$) reaction was investigated at RCNP in Osaka, Japan, with an experimental setup similar to that of the K600. A test run of 2 hours with a ^4He beam current of 300 nA incident on a 1.5 mg/cm^2 ^{13}C target yielded a position spectrum of ^9C in which the ground state could be clearly seen. The cross section of this reaction is 20 nb/sr [44].

CHAPTER 2

Mass predictions

This chapter describes the calculation concerning the masses of known nuclei along the proton drip line with a mass prediction code based on the Isobaric Multiplet Mass Equation (IMME), and then makes a few predictions of the masses of unknown nuclei which may be populated in future by five-neutron pick-up reactions.

2.1 The isobaric multiplet mass equation

Shortly after the discovery of the neutron, Werner Heisenberg proposed a new quantum number which described the proton and the neutron as two different states of the same particle [45, 46]. This quantum number was once often referred to as the isotopic spin [47]. Today, nuclear physicists prefer to call this quantum number T the isobaric spin, which is less confusing since T remains constant between isobars, but not between isotopes. It is also often referred to as the isospin.

The isobaric spin quantum number arose from the observation that protons and neutrons have the same spins ($S = \frac{1}{2}$) and nearly the same masses, and that the level schemes of lower lying states of mirror nuclei, which have the same A -numbers, but Z -numbers $Z_1 = \frac{1}{2}(A - k)$ and $Z_2 = \frac{1}{2}(A + k)$ where k is some integer, are very similar, as is illustrated by Fig. 2.1.

If the interaction between protons and neutrons was fully charge independent, then the energy spectra of mirror nuclei would be identical. The fact that they are not is an example of isobaric spin symmetry breaking caused by the Coulomb interaction between nucleons. The interaction between nucleons is mostly charge independent, and isobaric spin may be regarded as an approximate quantum number [46].

The proton and the neutron are associated with the isobaric spin projections $T_z = +\frac{1}{2}$ and $T_z = -\frac{1}{2}$ respectively. Hence the isobaric spin projection of a nucleus may be calculated using $T_z = \frac{1}{2}(Z - N)$. With the development of the quark model [48], the following relation was found between the isospin projection T_z and the up and down quark content of particles:

$$T_z = \frac{1}{2}[(n_u - n_{\bar{u}}) - (n_d - n_{\bar{d}})] \quad (2.1)$$

where n_u and n_d are the numbers of up and down quarks respectively, and $n_{\bar{u}}$ and $n_{\bar{d}}$ are the numbers of anti-up and anti-down quarks. From Eq. 2.1, a value of $T_z = \frac{1}{2}$ can be assigned to a proton, which has an (uud) quark configuration, and $T_z = -\frac{1}{2}$ to a neutron with its

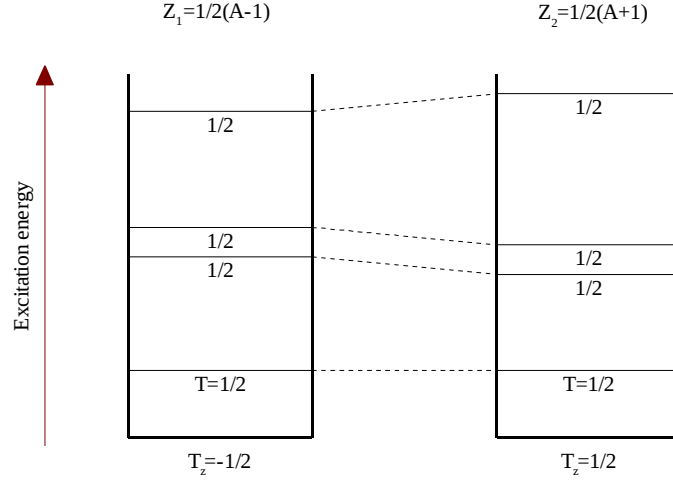


FIG. 2.1: Energy level scheme of two uneven A mirror nuclei. The energy level schemes are very similar, but not the same due to the differing Z -numbers.

(udd) configuration.

The isobaric spin T remains constant for all the members of an isobaric multiplet. The term $T = T_{z \max}$ indicates the isobaric spin of an isobaric multiplet, which runs from $-T = -T_{z \max}$ to $+T = +T_{z \max}$. An isobaric multiplet is a series of $2T+1$ nuclei of successively increasing charges but with identical nuclear wavefunctions such that the conversion of neutrons to protons along the series does not distinguish the neutrons from the protons, except in the overall charge of the nucleus [49].

If the wavefunctions of the members of an isobaric multiplet may all be regarded as identical, and if any charge dependences are of a two-body nature and may be treated as perturbations, then the nuclear mass of any member of the multiplet is given by [49, 50]:

$$M(A, T, T_z) = a(A, T) + b(A, T)T_z + c(A, T)T_z^2. \quad (2.2)$$

Eq. 2.2 is the quadratic form of the Isobaric Multiplet Mass Equation (IMME) [51]. This equation is implicit in the earliest work of Eugene Wigner [47], and was stated explicitly by him at the first Robert A. Welch Conference on Chemical Research in 1957 [52]. It is considered as a tool for predicting the masses of weakly bound nuclei. It may be used along with the known

masses of the stable members of an isobaric multiplet to make predictions about the masses of unstable members.

No higher powers of T_z and no odd-even alternations due to pairing or such causes are included in Eq. 2.2 [49]. The first term in the IMME is responsible for most of the nuclear binding. It is isoscalar in nature and is due to the strong interaction. The second is due to the Coulomb interaction and the third is due to the charge non-symmetric parts of the nucleon-nucleon interaction [46]. They are the isovector and isotensor terms.

The two-body electrostatic interaction between nucleons may be written as the sum of an isoscalar, isovector and isotensor operator [50]:

$$H_c = H_c^{(0)} + H_c^{(1)} + H_c^{(2)} . \quad (2.3)$$

This expansion does not go beyond the second rank, therefore in first order perturbation theory one obtains the expectation value [50]:

$$E_c(A, T, T_z) = E_c^{(0)}(A, T) - T_z E_c^{(1)}(A, T) + [3T_z^2 - T(T+1)]E_c^{(2)}(A, T) , \quad (2.4)$$

where $E_c^{(0)}$, $E_c^{(1)}$ and $E_c^{(2)}$ represent the scalar, vector and tensor Coulomb energies [53], which are independent of T_z . The mass of any member of an isobaric multiplet is given by

$$M(A, T, T_z) = M_0(A, T) + E_c(A, T, T_z) + T_z \Delta_{nH} , \quad (2.5)$$

where $\Delta_{nH} = 782.354$ keV is the neutron-hydrogen mass difference and M_0 represents the charge-free nuclear mass [50, 53].

By substituting the Coulomb energy term from Eq. 2.4 into Eq. 2.5, one obtains the coefficients of the IMME [50]:

$$a = M_0 + E_c^{(0)} - T(T+1)E_c^{(2)} , \quad (2.6)$$

$$b = \Delta_{nH} - E_c^{(1)} , \quad (2.7)$$

$$c = 3E_c^{(2)} . \quad (2.8)$$

If one considers the atomic nucleus as a classical, homogeneously charged sphere with radius $R = r_0 A^{1/3}$ where $r_0 = 1.2$ fm, then one may write the following [50]:

$$E_c = \frac{3e^2 Z^2}{5r_0 A^{1/3}} , \quad (2.9)$$

$$E_c^{(1)} = \frac{3e^2 A^{2/3}}{5r_0}, \quad (2.10)$$

$$E_c^{(2)} = \frac{e^2}{5r_0 A^{1/3}}. \quad (2.11)$$

E_c in the above represents the Coulomb energy, while $E_c^{(1)}$ and $E_c^{(2)}$ represent the vector and tensor Coulomb energies.

Clearly the b and c coefficients will be the same for any nucleus in an isobaric multiplet. They may be obtained using Eqs. 2.7, 2.8, 2.10 and 2.11 for any nucleus in a multiplet simply by knowing the atomic mass number of the nucleus. The a coefficient from Eq. 2.6 is less trivial to predict, since it is also dependent on the charge-free nuclear mass M_0 and the isoscalar Coulomb energy $E_c^{(0)}$. The scalar Coulomb energy $E_c^{(0)}$ represents an average Coulomb energy for a given multiplet. It cannot be separated from the nuclear energy M_0 , because both should exhibit the same A and T dependence [50, 53].

2.2 The mass prediction code

The mass prediction code IMME.C, which uses the quadratic IMME, was written with C++ programming language in ROOT version 5 [54]. The code predicts the mass of an unknown nucleus as follows:

- The known masses of experimentally observed nuclei are used for M and M_0 to calculate $E_c^{(0)}$ for each mass number Z in an isobaric multiplet by combining Eqs. 2.2 and 2.6.
- The mass of some nucleus in the same isobaric multiplet as the proton-rich nucleus of interest is used for M , and the mass of the nucleus with just one less proton and one more neutron than M is used for M_0 .
- This calculation is done with each member of the multiplet used once as M , except for the one with the lowest mass number.
- The different values of $E_c^{(0)}$ are plotted against the corresponding mass numbers Z for which they were calculated.
- If a linear plot is yielded, then an accurate value of $E_c^{(0)}$ can be extrapolated for the nucleus of interest.
- With M_0 and $E_c^{(0)}$ known, it is possible to calculate the a coefficient from Eq. 2.6.

- One now has a value for all the coefficients in the IMME for the nucleus of interest. The projection of its isobaric spin T_z may be easily calculated, therefore the mass M of the nucleus may be calculated using the IMME in Eq. 2.2.

2.3 Results of mass predictions

2.3.1 Calculations for $A = 19$ isobars

The first task of the mass prediction code was to calculate the ground state (g.s.) mass of ^{19}Mg , which is known to be a two-proton emitter [27], with the ground state mass known for all its isobars from ^{19}N through to ^{19}Na . A linear plot, which is illustrated in Fig. 2.2, was generated for $E_c^{(0)}$ vs Z which indicates that an accurate value of $E_c^{(0)}$ could be extrapolated for ^{19}Mg in (a) of Table 2.1. A mass excess of 32.3201 MeV was found, which is within 1 MeV of the value provided by the American National Nuclear Data Center (NNDC) [1], as one can see in the second column of Table 2.1. Recently, the mass of ^{19}Mg has been measured at 30.5466 MeV [55]. The calculated mass is still within 2 MeV of this value [55].

The same procedure was followed in (b) with a value of $E_c^{(0)}$ obtained from an extrapolation using all the isobars of ^{19}Mg from the highly neutron-rich ^{19}B . The value obtained, which is indicated by (b) in Fig. 2.1, is within 0.5 MeV of the value provided by the NNDC.

The next step was to put the code to a more rigorous test by attempting to calculate the mass of ^{19}O from the masses of ^{19}B , ^{19}C and ^{19}N . The value yielded in the third column of Table 2.1 does not show good agreement with the experimental value provided by the NNDC, apparently too few data points were used. A fairly good agreement (within 0.5 MeV of the experimental) was found for ^{19}F from its four more neutron-rich isobaric neighbours, and ^{19}Ne was calculated with an even better agreement with the experimental value from its five more neutron-rich isobaric neighbours. By using the value calculated by the code for ^{19}Ne , both ^{19}Na and ^{19}Mg in (c) could be calculated with a fairly good agreement with experimental values.

Nucleus	Experimental value [MeV]	Calculated value [MeV]
^{19}Mg (a)	33.040	32.320
^{19}Mg (b)	33.040	32.632
^{19}O	3.335	10.479
^{19}F	-1.487	-1.0878
^{19}Ne	1.751	2.0139
^{19}Na	12.927	14.077
^{19}Mg (c)	33.040	34.837

TABLE 2.1: Calculations for the $A = 19$ isobars in the 3rd column are compared to the experimentally measured values in the 2nd column.

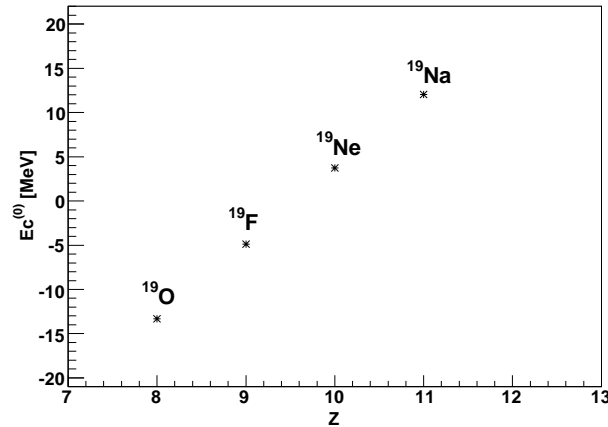


FIG. 2.2: Plot of $E_c^{(0)}$ vs Z for first calculation of ^{19}Mg . A linear plot was yielded, which means that an accurate value of $E_c^{(0)}$ could be extrapolated for ^{19}Mg .

2.3.2 Calculations for $A = 22$ isobars

The ground state mass of ^{22}Al in (a) of Table 2.2 was calculated by using the known masses of all its isobars from the line of stability to the neutron-deficient side, and in (b) it was calculated by using the known masses of all its isobars from the neutron-rich to the neutron-deficient side. An attempt at calculating the even more exotic ^{22}Si was also made by using the same method as in (a). The plot in Fig. 2.3 for the calculation of ^{22}Al (a) is not linear, therefore an accurate value for $E_c^{(0)}$ could not be extrapolated. Hence it is not surprising that the calculated values shown in Table 2.2 do not show the same agreement with experimental data as those in Table 2.1. This result is probably related to the difference in pairing energies between even and odd nuclei (see section 2.3.5).

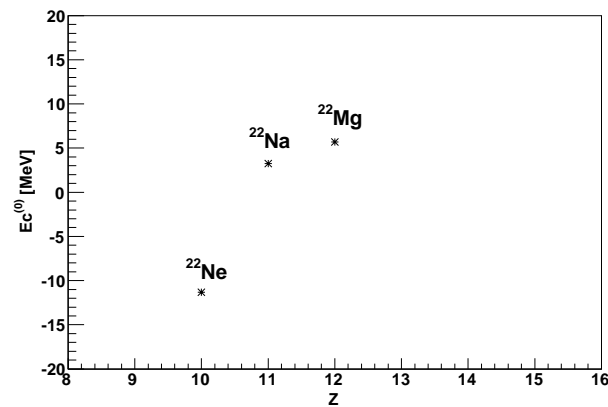


FIG. 2.3: Plot of $E_c^{(0)}$ vs Z for first calculation of ^{22}Al . This plot is not linear which means that an accurate value of $E_c^{(0)}$ could not be extrapolated for ^{22}Al .

Nucleus	Experimental value [MeV]	Calculated value [MeV]
^{22}Al (a)	18.183	12.796
^{22}Al (b)	18.183	10.803
^{22}Si	32.164	46.961

TABLE 2.2: Calculations for the $A = 22$ isobars in the 3rd column are compared to the experimentally measured values in the 2nd column.

2.3.3 Calculations for $A = 43$ isobars

The ground state mass of ^{43}Cr in (a) of Table 2.3 was calculated by using the known masses of all its isobars from the line of stability to the neutron-deficient side, and in (b) it was calculated using the known masses of all its isobars from the neutron-rich to the neutron-deficient side. A linear plot was yielded for the calculation of ^{43}Cr in (a), therefore the agreement of the calculated value to the measured data is not surprising. The mass of ^{43}Ti was calculated from those of ^{43}K , ^{43}Ca and ^{43}Sc with an impressive agreement with experimental data. Its calculation was then used to calculate the masses of ^{43}V and ^{43}Cr in (c), both with reasonable although decreasing agreement with data.

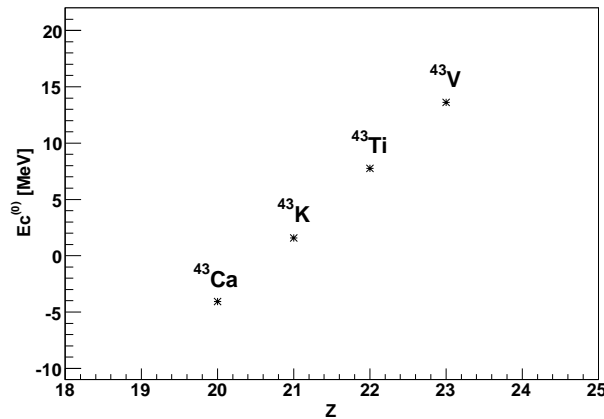


FIG. 2.4: Plot of $E_c^{(0)}$ vs Z for first calculation of ^{43}Cr . This plot is linear which means that an accurate value of $E_c^{(0)}$ could be extrapolated for ^{43}Cr .

Nucleus	Experimental value [MeV]	Calculated value [MeV]
^{43}Cr (a)	-2.133	-2.174
^{43}Cr (b)	-2.133	-1.444
^{43}Ti	-29.321	-29.724
^{43}V	-18.024	-18.906
^{43}Cr (c)	-2.133	-3.696

TABLE 2.3: Calculations for the $A = 43$ isobars in the 3rd column are compared to the experimentally measured values in the 2nd column.

2.3.4 Calculations for $A = 45$ isobars

The ^{45}Fe isotope is the first nucleus in which two-proton radioactivity was measured [29, 30]. Its ground state mass in (a) of Table 2.4 was calculated by using the known masses of all its isobars from the line of stability to the neutron-deficient side, and in (b) it was calculated using the known masses of all its isobars from the neutron-rich to the neutron-deficient side. The same procedure that was followed for calculating (a) and (b) in Table 2.2 of section 2.3.2 was used for calculating the ground state mass of ^{45}Fe in (a) and (b) of Table 2.4. The plot in Fig. 2.5 was used for the extrapolation of $E_c^{(0)}$, which was used for the calculation of ^{45}Fe in (b). The value of ^{45}Fe in (b), which was generated from the masses of 11 isobars, is within 0.2 MeV of the experimental value. The mass of ^{45}Cr was calculated from the more neutron-rich isobars ^{45}V , ^{45}Ti and ^{45}Sc , and a value within 1 MeV of the experimental value was found. This value was used to calculate the masses of the increasingly neutron-deficient isobars ^{45}Mn and ^{45}Fe in (c), with values that increased exponentially in divergence from the experimental values.

Nucleus	Experimental value [MeV]	Calculated value [MeV]
^{45}Fe (a)	13.597	12.616
^{45}Fe (b)	13.597	13.785
^{45}Cr	-18.965	-19.689
^{45}Mn	-5.114	-2.435
^{45}Fe (c)	13.579	19.883

TABLE 2.4: Calculations for the $A = 45$ isobars in the 3rd column are compared to the experimentally measured values in the 2nd column.

2.3.5 Calculations and predictions along the proton drip line

This subsection presents calculations and predictions which were made by the code for various light nuclei in the vicinity of the proton drip line. The calculations in Tables 2.5 and 2.6

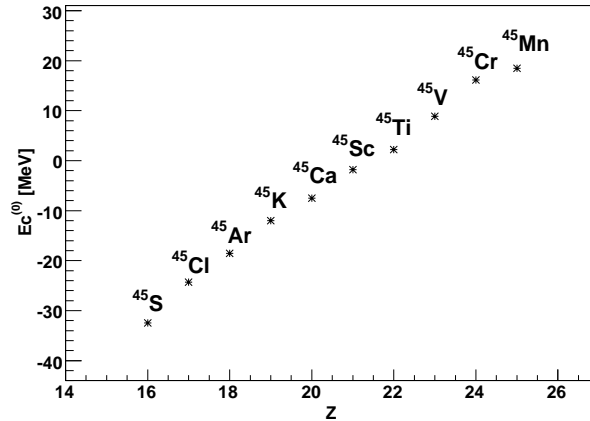


FIG. 2.5: Plot of $E_c^{(0)}$ vs Z for first calculation of ^{45}Fe . All the isobars of ^{45}Fe , from the neutron-rich ^{45}S to the neutron-deficient ^{45}Mn were used for this plot. It has a linear shape which means that an accurate value of $E_c^{(0)}$ could be extrapolated for ^{45}Fe .

are respectively for odd and even nuclei that have been determined experimentally, while the predictions in Table 2.7 are for nuclei yet to be measured. The plots in Figs. 2.6 and 2.7 are associated with the data in Tables 2.5 and 2.6 respectively.

The calculations which were made for odd nuclei, shown in Fig. 2.6, show far better agreement with the experimental data than the ones which were made for even nuclei, shown in Fig. 2.7. Furthermore, the predicted values of the even-even nuclei in Fig. 2.6 are all much larger than the experimental values, while the opposite is true for all the odd-odd nuclei. This phenomenon may be attributed to the fact that nuclei with even numbers of protons or neutrons are more stable than those with odd numbers are. Both odd-odd and even-even nuclei were used in the determination of the masses of each of these nuclei, with the effect of the pairing energy not taken into account. The pairing energy adds to the binding energy in even-even nuclei, thus decreasing its mass excess. This may account for the fact that the values predicted for the masses of the even-even nuclei in Table 2.6 and Fig. 2.7 are all much larger than the experimental values. The opposite must then be true for odd-odd nuclei where the pairing energy lowers the binding energy and thus increases the mass excess. Hence the predictions for odd-odd nuclei are all lower than the experimental values.

Odd nuclei must have either even-odd or odd-even nucleon compositions, therefore pairing has a negligible effect in them [3]. Hence the values obtained for odd nuclei, shown in Table 2.5 and Fig. 2.6, show good agreement with the experimental values. Following this good agreement with experimental data for the odd nuclei, some mass predictions were performed for odd nuclei

along the proton drip line. The results of these predictions are shown in Table 2.7. According to these predictions, all of the nuclei shown in Table 2.7 are unbound to one-proton ($1p$) decay. The value of Δ_{1p} could not be found for ^{21}Si , since the mass of ^{20}Al , which would be the product of its decay by $1p$, is also not known. All of the nuclei, except for ^7C and ^{21}Si , are also predicted to be unbound to two-proton ($2p$) decay. The ^7C isotope is unbound to $1p$ decay by merely about 300 keV, hence one would expect to measure an unbound ground state for this nucleus. The same might also be true for ^{25}S , while ^{33}Ca represents a possible candidate for $2p$ decay. However, these nuclei are very close to the thresholds for $1p$ and $2p$ decay and the states of the daughter nuclei are often very broad. The sequential decay through the tails of these broad states is possible [56, 57], which makes it very difficult to make predictions about the decay modes of these exotic nuclei. As the nuclei become heavier, the mass excess tends to decrease due to the increase in binding energy.

Nucleus	Experimental value [MeV]	Calculated value [MeV]
^5Be	37.996	33.771
^7B	27.868	28.580
^9C	28.910	28.158
^{11}N	24.624	23.935
^{15}F	16.775	16.535
^{19}Mg	33.040	32.632
^{21}Al	26.119	31.073
^{23}Si	23.772	27.320
^{27}S	17.543	17.014
^{31}Ar	11.293	11.643
^{33}K	8.170	6.763
^{35}Ca	4.602	6.735
^{39}Ti	1.500	5.773
^{43}Cr	-2.133	-2.174
^{45}Fe	13.597	13.785

TABLE 2.5: Calculations of odd nuclei along the proton drip line in the 3rd column are compared to the experimental values in the 2nd column.

Nucleus	Experimental value [MeV]	Calculated value [MeV]
${}^6\text{Be}$ (e-e)	18.375	31.339
${}^8\text{C}$ (e-e)	35.094	55.217
${}^{10}\text{N}$ (o-o)	38.800	31.392
${}^{12}\text{O}$ (e-e)	32.048	49.199
${}^{14}\text{F}$ (o-o)	32.658	26.044
${}^{16}\text{Ne}$ (e-e)	23.997	37.811
${}^{20}\text{Mg}$ (e-e)	17.570	29.589
${}^{22}\text{Al}$ (o-o)	18.183	12.796
${}^{22}\text{Si}$ (e-e)	32.164	46.961
${}^{26}\text{S}$ (e-e)	25.970	35.443
${}^{30}\text{Ar}$ (e-e)	20.083	30.085
${}^{32}\text{K}$ (o-o)	20.418	-0.141
${}^{34}\text{Ca}$ (e-e)	13.153	21.117
${}^{38}\text{Ti}$ (e-e)	9.101	17.789
${}^{42}\text{Cr}$ (e-e)	5.990	15.609

TABLE 2.6: Calculations of even nuclei along the proton drip line in the 3rd column are compared to the experimental values in the 2nd column. Even-even nuclei are indicated by (e-e), and odd-odd nuclei are indicated by (o-o).

Deviation [MeV] vs A

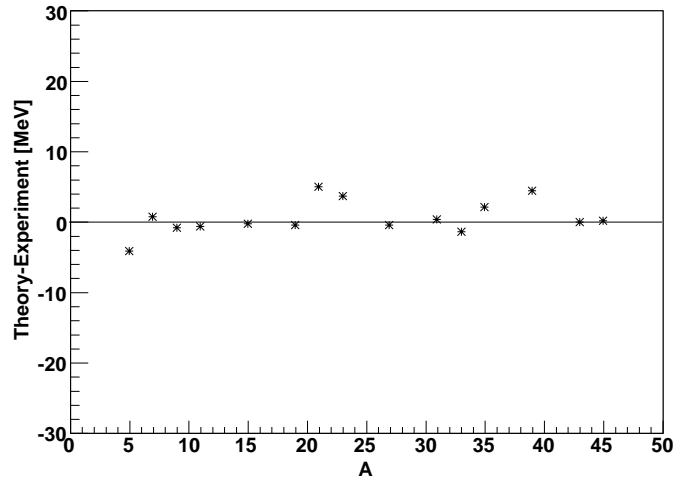


FIG. 2.6: Plot of deviation from experimentally measured values for mass calculations of odd nuclei.

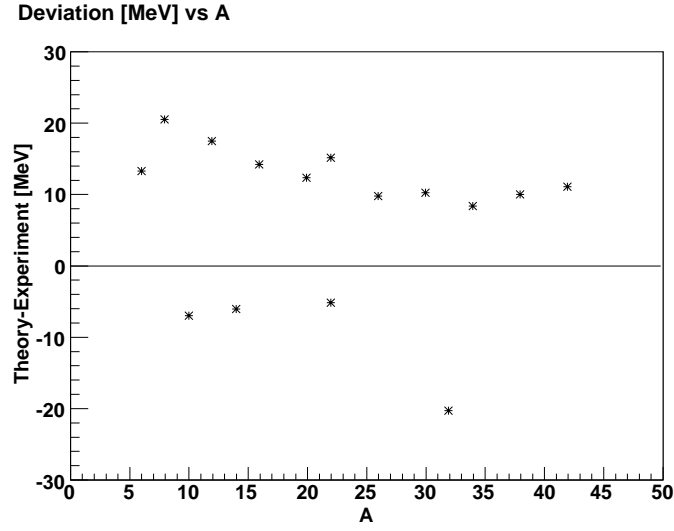


FIG. 2.7: Plot of deviation from experimentally measured values for mass calculations of even nuclei.

Nucleus	Theoretical value [MeV]	Δ_{1p} [MeV]	Δ_{2p} [MeV]
^5B	88.225	51.780	44.980
^7C	51.203	0.311	-1.371
^9N	60.456	18.073	18.010
^{11}O	50.129	4.041	6.641
^{13}F	56.481	17.144	17.280
^{15}Ne	41.702	1.755	4.012
^{21}Si	47.157	-	-0.461
^{23}P	47.901	8.448	7.204
^{25}S	39.305	0.019	0.955
^{31}K	36.270	8.898	8.549
^{33}Ca	28.375	0.668	2.504
^{41}Cr	20.315	2.696	4.237

TABLE 2.7: Predictions of nuclei that have not yet been measured are shown in the 2nd column, and the Δ_{1p} and Δ_{2p} values which were calculated from these predicted values are shown in the 3rd and 4th columns. Predictions are included for odd nuclei only, since the values generated by the code for even nuclei are not yet to be trusted.

CHAPTER 3

The Experiment

The experiment was conducted at iThemba Laboratory for Accelerator Based Sciences (iThemba LABS) Western Cape. iThemba LABS is a multidisciplinary institute which provides particle beams for basic and applied research, radionuclide production and particle radiotherapy [58].

The aim of the experiment was to measure the $^{27}\text{Al}(^3\text{He},^8\text{He})^{22}\text{Al}$ reaction, but for reasons to be explained in later chapters only the following reactions could be measured:

1. $^{27}\text{Al}(^3\text{He},p)^{29}\text{Si}$
2. $^{27}\text{Al}(^3\text{He},d)^{28}\text{Si}$
3. $^{27}\text{Al}(^3\text{He},t)^{27}\text{Si}$
4. $^{27}\text{Al}(^3\text{He},^3\text{He})^{27}\text{Al}$
5. $^{27}\text{Al}(^3\text{He},^4\text{He})^{26}\text{Al}$.

All these reactions were investigated in order to gain confidence in the experimental setup and to understand the different reactions measured with the ^3He beam. The K600 light ion spectrometer was used to perform the experiment. A new drift chamber, designed and manufactured at iThemba LABS, was used for the first time during this experiment. This newly installed drift chamber allows for improved vertical position determination.

This is also the first experiment performed with the new data acquisition system (DAQ), which uses VME (Versa Modula Europa) electronics and MIDAS (Maximum Integration Data Acquisition System) software [59]. The previous DAQ, which used CAMAC (Computer Automated Measurement and Control) electronics and XSYS software, had to be replaced because of the increase in time to digital converter (TDC) channels associated with the new drift chambers, and because Lecroy, the manufacturer of the electronics for the previous DAQ, no longer exists. It is envisaged that, for the same dead time, the new DAQ may obtain a much higher count-rate than what was possible with the previous DAQ.

3.1 The particle beam and targets

The ^3He beam used in this experiment was produced in an ECR (Electron Cyclotron Resonance) ion source. The ^3He gas, which was obtained from the β^- decay of tritium, was purchased from a French company known as Chemgas [60]. Particle beams at iThemba LABS are

pre-accelerated by one of two Solid Pole injector Cyclotrons (SPCs). The ^3He beam from the ion source was delivered to the one referred to as SPC2 in Fig. 3.1, where it was accelerated to an energy of about 10.4 MeV. The particle beam was then steered through the K beam line and injected into the Separated Sector Cyclotron (SSC) where it was accelerated to the desired energy, which was 220 MeV in the case of this experiment. From here the beam was steered along the X, P1, P2 and S lines and delivered to the spectrometer vault.

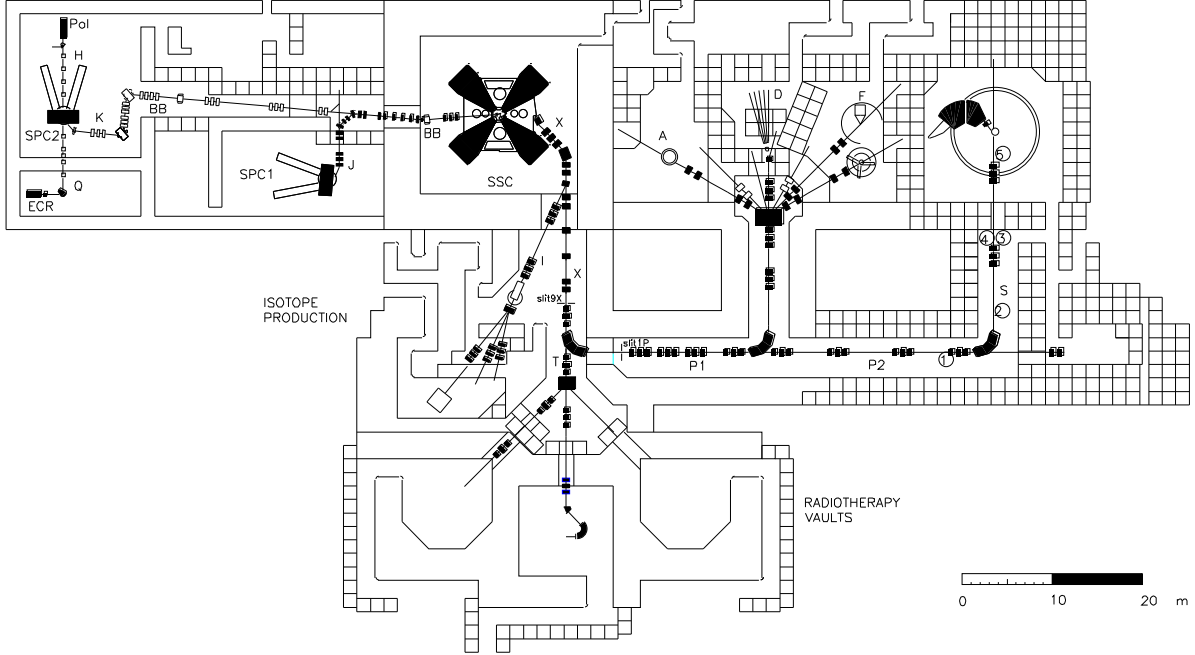


FIG. 3.1: Floor-plan of the cyclotron facility

The targets were mounted on a target ladder inside a 524-mm-diameter scattering chamber which is situated at the turning axis of the spectrometer (see Fig. 3.2). The ladder is mounted perpendicularly to the beam direction and can hold six targets simultaneously. For this measurement, it contained an empty frame to measure the background, a viewer to help in focusing the beam, a ^{64}Ni target with a thickness of $2.43 \text{ mg}\cdot\text{cm}^{-2}$ to attempt to replicate the results from the Princeton experiment, and three ^{27}Al targets of thicknesses $4.43 \text{ mg}\cdot\text{cm}^{-2}$, $5.83 \text{ mg}\cdot\text{cm}^{-2}$ and $8.19 \text{ mg}\cdot\text{cm}^{-2}$. The different thicknesses of the Al targets were required to enable for the optimisation of peak width and count rate during data taking.

The maximum cross section for the $(^3\text{He},^8\text{He})$ reaction is expected at an angle of $\theta_{lab} = 1^\circ$. The spectrometer angle of $\theta_{lab} = 8^\circ$ was used as it was the minimum attainable angle of the spectrometer at the time of the measurement. Beam intensities on target varied from 1 to 20 nA.

Count rates with an Al target of thickness $4.43 \text{ mg}\cdot\text{cm}^{-2}$ and a beam of 10 nA were typically of the order of 2 kHz. For an empty frame and a beam current of 10 nA, a rate of roughly 200 Hz was commonly measured.

3.2 The K600 magnetic spectrometer

The K600 magnetic spectrometer at iThemba LABS is based on the design of the former K600 magnetic spectrometer at the Indiana University Cyclotron Facility [61]. The energy constant K for the magnetic spectrometer or any magnetic device is defined as

$$K = \frac{mE}{q^2} . \quad (3.1)$$

The mass m of the particle is measured in atomic mass units, its charge q in units of proton charge and its kinetic energy E in MeV [62]. The K -value of the spectrometer is defined as the maximum possible value of K , as calculated in Eq. 3.1, that the spectrometer is designed for. For example, the K600 spectrometer, which derives its name from its K -value of 600, is capable of detecting protons or α particles of up to 600 MeV kinetic energy, deuterons of up to 300 MeV kinetic energy, tritons of up to 200 MeV and helions of up to 800 MeV kinetic energy.

The magnetic Lorentz force

$$\vec{F} = q\vec{v} \times \vec{B} , \quad (3.2)$$

where q represents the particle charge, \vec{v} represents the particle velocity, \vec{B} represents the constant magnetic field in the spectrometer and \vec{F} represents its force on the particle moving through it, is exploited by the spectrometer to distinguish between particles of different magnetic rigidities. The charged particle enters the spectrometer in a direction perpendicular to its magnetic field, which then acts on the particle as a centripetal force. A centripetal acceleration is induced, which causes the particle to make a circular orbit of radius r inside the magnetic field. This radius r defines the radius of curvature of the particle. Hence it follows that

$$qvB = \frac{mv^2}{r} \quad (3.3)$$

$$\Rightarrow rB = \frac{p}{q} , \quad (3.4)$$

where the quantity p denotes the magnitude of the particle momentum. The magnetic rigidity R is defined as

$$R = rB , \quad (3.5)$$

where r represents the radius of curvature of the particle through the spectrometer, and B represents the magnitude of the constant magnetic field, so that

$$R = \frac{p}{q} . \quad (3.6)$$

In a constant magnetic field, a unique relationship between the charge and the momentum of a particle may be associated with a unique radius of curvature, and therefore also to a unique angle of incidence on the focal plane. Measurement of the radius of curvature can thus yield information about the momentum of the particle, provided that the charge and the mass of the particle is known [63]. In the non-relativistic limit, one may write

$$R = \frac{\sqrt{2mE}}{q} . \quad (3.7)$$

Thus it follows, from Eq. 3.7 and the definition of the energy constant K given in Eq. 3.1, that

$$R = \sqrt{2K} . \quad (3.8)$$

Hence two particles with the same K -value will have the same rigidity and therefore end up at the same position in the focal plane, but they will not necessarily have the same mass, charge or energy [64]. Diagnostic methods such as looking at the time-of-flight (TOF) of different particles can be used to separate different particles in such cases.

For a given magnetic field setting of the K600 one can only look at a relatively narrow momentum region, which translates into a narrow energy region in the focal plane, so that

$$\frac{P_{max}}{P_{min}} = 1.097 . \quad (3.9)$$

K -value calculations were performed for different reactions in order to determine, for the magnet settings that were used to observe a specific particle, which other particles fall within the narrow energy region that reaches the focal plane. The results of these calculations will be shown in the next chapter.

The K600 consists of five active elements, namely a quadrupole (Q), two dipoles (D1 and D2) and two trim coils (K and H), as shown in Fig. 3.2. The quadrupole provides vertical focusing of the beam, while the two dipoles are the main dispersion elements. The two trim coils provide the final focusing at the focal plane [65]. The K-coil provides for first-order focusing or correction of the $(x | \theta)$ - aberration as it is denoted by Enge [65], while the H-coil provides for second-order focusing or correction of the $(x | \theta^2)$ aberration. The term $(x | \theta)$ refers to the sensitivity of the

focal plane position x_{fp} to the scattering angle θ_{scat} of the reaction products, while the term $(x | \theta^2)$ provides a measure of the dependence of x_{fp} on θ_{scat}^2 .

In front of the quadrupole is a carousel which houses six collimators. After scattering, the particles pass through one of these collimators which then defines the angular acceptance of the spectrometer. In this experiment a collimator with a diameter of 55 mm was used for all data taking. The distance from the target to the back of the collimator is 735.5 mm, which implies that a solid angle of 4.39 msr was subtended by the collimator [66].

After reacting with the target, charged particles follow a curved path through the K600 vacuum chamber before exiting through a Kapton window in the focal plane. Particles of different magnetic rigidities, hence of different momentum to charge ratios, are focused at different positions and incident angles in the focal plane of the spectrometer. The focal plane position-sensitive detector package is situated just downstream of the Kapton exit window, behind the second dipole. It is positioned at an angle of 35.75° with respect to the central ray through the spectrometer. The spectrometer can be operated in the low, high or medium momentum dispersion modes, and has corresponding focal planes for each of these. During this experiment, the medium dispersion mode was used.

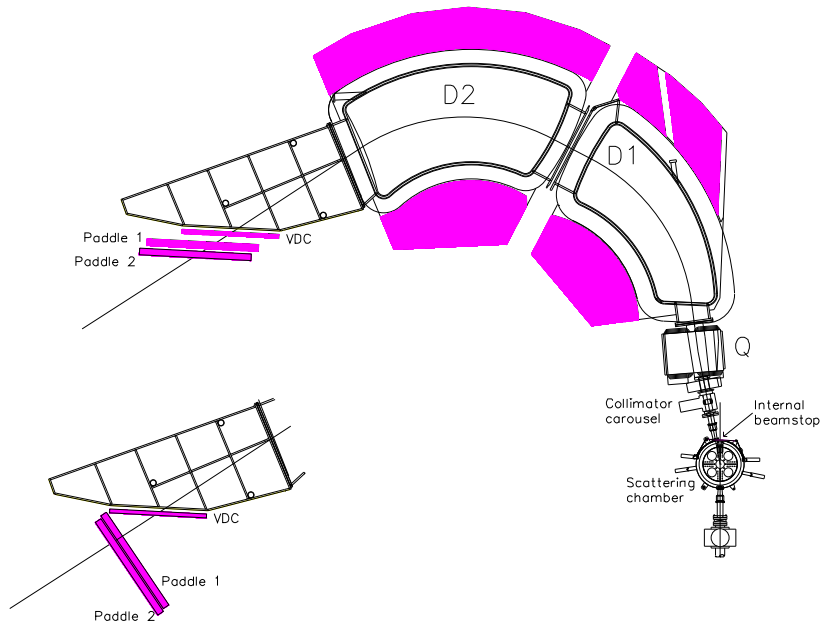


FIG. 3.2: A schematic overview of the K600 magnetic spectrometer. The focal plane detector package is illustrated twice on the left of this diagram in order to illustrate the two different paddle angles which were used (see section 3.3.4).

3.3 The focal plane detector package

After traveling through a flight path of approximately 8 m from the target to the focal plane, reaction products are detected by the vertical drift chamber (VDC) and scintillation detectors (Paddle 1 and Paddle 2) shown in Fig. 3.2. The VDC used in this experiment was of the so called U-X configuration, which is new to the K600. It contains a U-wire plane followed by an X-wire plane, as opposed to the previous VDC model which contained only an X-wire plane. In the previous model, the VDC was used in tandem with a Horizontal Drift Chamber (HDC) in order to obtain both horizontal (x) and vertical (y) resolution. In the new model of VDC, the U plane is used to obtain much improved y resolution. In the U-wire plane the wires are inclined at 50° with respect to the horizontal, while in the X-wire plane they are at 90° . The VDC was placed upstream of the scintillation detectors, which were used as trigger detectors. This way the scintillation detectors could not have an effect on the resolution obtainable with the VDC. The focal plane detectors were positioned along the focal plane of the spectrometer on steel support rails.

3.3.1 The vertical drift chamber

There are two main types of wire chambers. Both rely on the ionization of gas molecules by each incident particle to cause a cascade of electrons in a uniform electric field to drift towards its wires. In the first type of wire chamber, the multi-wire proportional counter (MWPC), the energy deposited in the detector may be determined since the number of cascades and therefore the signal size should be proportional to the energy of the incident particle. The position may be determined with a limited accuracy by looking at the wire number where a hit was registered.

This experiment employed the second type of wire chamber, a multi-wire drift chamber (MWDC). In a drift chamber it is possible to measure the times of the current pulses from the wires precisely and then to use this information along with the characteristic drift velocity of the chamber to determine the path of each incident particle far more accurately. For the drift chamber used drift velocities are of the order of $4\text{-}6 \times 10^4 \text{ m}\cdot\text{s}^{-1}$, therefore drift times of 133-200 ns may be expected for 8 mm, which is the maximum geometrically possible drift distance [66].

The drift chamber used for this experiment is known as a vertical drift chamber. In a vertical drift chamber (VDC), the drift direction of the electrons is perpendicular to the wire plane, whereas it would be parallel to the wire plane in a horizontal drift chamber (HDC) [66]. A vertical drift chamber has three unique features which are advantageous to position detection at the focal plane of a spectrometer:

1. Its geometry provides a very small region of non-uniform field around its sense wires.

2. It is possible to achieve both cell identification and drift time measurement.
3. The additional ability to measure angle enables the code for on-line data analysis to correct for spectrometer aberrations and other effects that limit resolution when only particle position is determined [67].

The new VDCs were designed mainly to meet the needs of the 0° setup in the high dispersion focal plane, while still being capable of replacing the previous medium dispersion focal plane detectors. The drift chamber mainly consists of three high-voltage cathode planes (HV planes), placed parallel to each other, and two signal wire anode planes (U and X) placed in between them as in Fig. 3.3. The U-wire plane lies between the upstream and the middle HV planes, while the X-wire plane lies between the middle and the downstream HV planes. The main drift direction of the secondary electrons is perpendicular to these signal wire planes. Two $25\text{-}\mu\text{m}$ -thick mylar planes are used to isolate the interior of the VDC from the atmosphere.

3.3.2 VDC design considerations

One very important design consideration of the new VDC was that of whether to place the U plane upstream or downstream of the X plane. In the case where the X plane is placed upstream of the U plane, there would be a bigger restriction over the focal plane area for which the full x and y coordinates can be established, than the case where the U plane is placed upstream of the X plane as in Fig. 3.3. This makes it more desirable to place the U plane upstream of the X plane.

There were concerns, however, that placing the U plane upstream of the X plane might have a negative impact on the accuracy of the determination of the horizontal position due to multiple scattering caused mainly by the signal and guard wires of the U plane. Hence the effect of multiple scattering was investigated with two different codes:

- LISE [68] was used to calculate the angular and positional straggling,
- while SRIM [69] was used only to calculate the positional straggling that could be expected.

The calculations indicated that, even with the loss in angular and positional resolution due to multiple scattering, the detectors can, in principle, still measure scattered particles with an energy resolution better than the K600 design limit.

Hence it was decided to design the VDC with the U-X wire plane configuration. The possibility still exists that the VDC might yield bad resolution unforeseen by the multiple scattering estimations. Therefore the VDC was designed so that it is still possible to rotate it to have the

X plane upstream of the U plane. The low momentum (LoP) side of the detector was designed to be the inverse of its high momentum (HiP) side, so the VDC is symmetrical with respect to rotation by 180° .

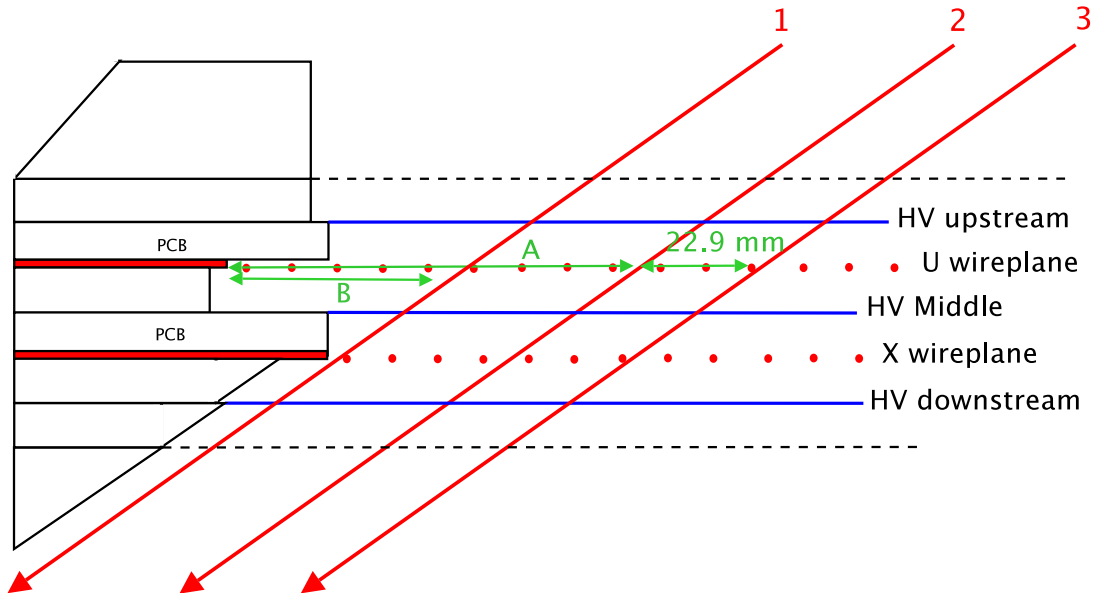


FIG. 3.3: Schematic overview of the HiP side of the new VDC design which has the U plane upstream of the X plane. A ($= 89.12$ mm) indicates the region where there will not be full coverage of the y coordinate due to the slanted nature of the U wires. B ($= 47.17$ mm) indicates the region where less than half of the y coordinate may be established. The distance of 22.9 mm is what would be lost for measuring full x and y coordinates if the X plane was placed upstream of the U plane instead. The numbers 1, 2 and 3 indicate different particles coming from the target and entering the drift chamber at roughly 35° with respect to the wire planes.

3.3.3 VDC construction

This subsection describes aspects of the construction of the new drift chamber, which is illustrated diagrammatically in Fig. 3.4.

3.3.3.1 Stesalit chassis

Stesalam EP107-M950-40 [70], formerly known as Stesalit 4411W, was used as base material for the VDC frame. Stesalam EP107-M950-40, which is a glass fibre and epoxy composite, is a very good insulator and also a very rigid material. It is proven to have low out-gassing properties, which is crucial for high-rate detectors where low pollutant out-gassing is a priority. Its glass fibres are very small and randomly oriented, so that precision machining is made possible without inducing flaking or chafing [71]. All the stesalit frames, except those fixed to the Printed Circuit



FIG. 3.4: Autocad image of the assembled new VDC with the wires not yet inserted in the sense region.

Board (PCB), are $8 \text{ mm} \pm 0.05 \text{ mm}$ thick.

3.3.3.2 Sense region

The sense region of the VDC consists of signal wires with guard wires interspersed between them. The guard wires provide field shaping and define drift cells, associated with each signal wire, of about 4 mm wide [71]. Both the U and the X planes have a separation of 4 mm between their signal wires, which have guard wires midway between them. The distance from the cathode high-voltage plane to the anode signal wire plane is 8 mm. Hence the drift cells have a width of 4 mm and a cell length of 16 mm.

Fig. 3.5 illustrates that, at the nominal trajectory angle for the central beam ray, which was calculated at 35.75° , particles should cross 3 or 4 drift cells while passing through the U plane, and 5 or 6 drift cells while passing through the X plane. This difference occurs because the horizontal signal wire to signal wire spacing will be 4 mm in the X plane and 5.22 mm in the U plane where the wires are inclined at 50° with respect to the horizontal, as is illustrated by Fig. 3.6.

In a wire chamber, it is important for accurate time-to-position information to have an electric field that remains nearly constant between the HV planes and the wire plane, but increases very sharply in the regions around the sense wires where the electron avalanching must occur [72]. GARFIELD models of the magnitude of the equipotential surfaces and the magnitude of the electric field for the VDC sense region are shown in Fig. 3.7 [73].

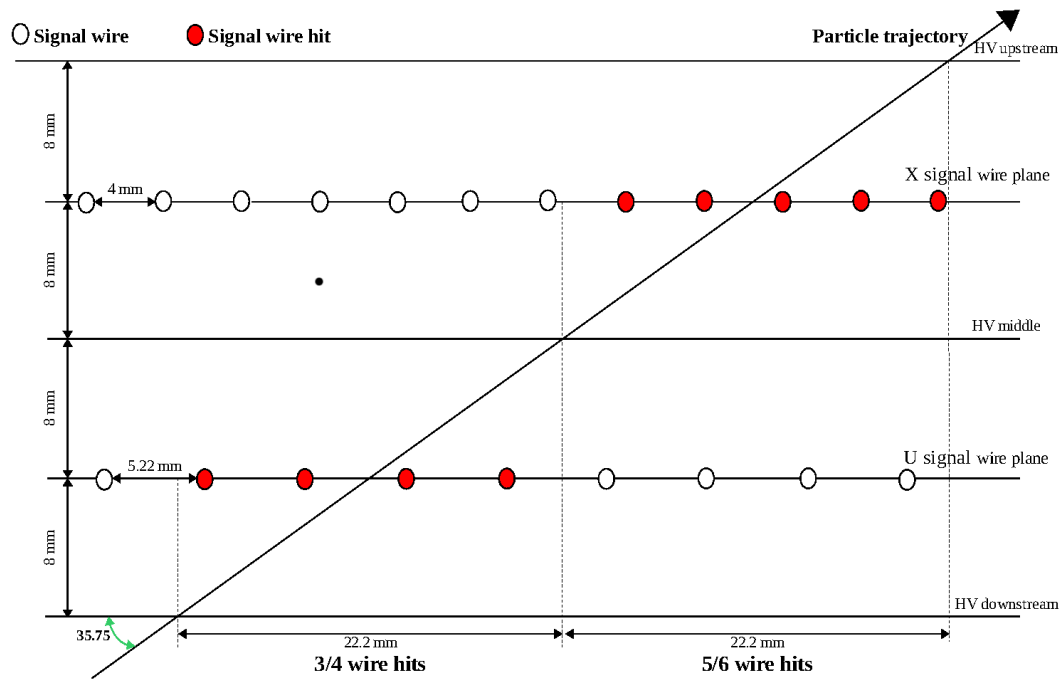


FIG. 3.5: Top view of U-X wire chamber illustrating a typical track of a particle through the wire chamber system with $\theta = 35.75^\circ$ for the central ray. Guard wires are not included in this figure.

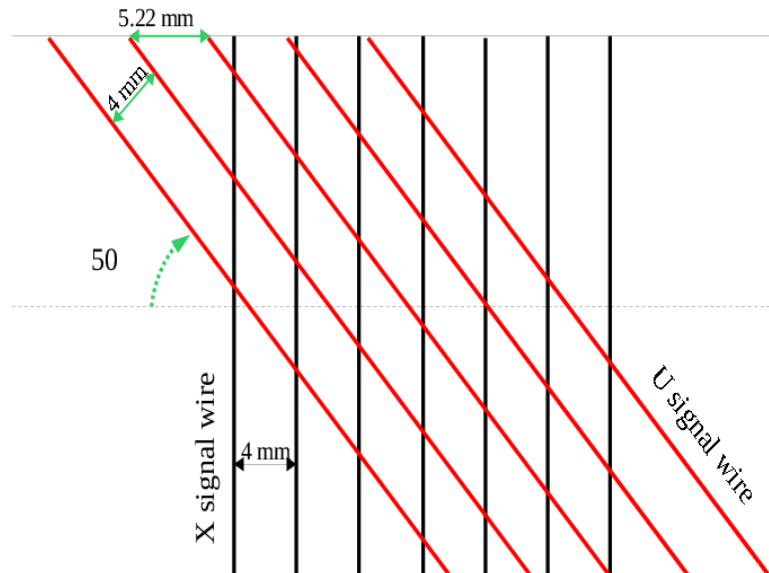


FIG. 3.6: Side view of U and X wires illustrating their different coordinate systems, and how the horizontal spacing between the U wires is 5.22 mm while the perpendicular wire spacing is still 4 mm for both planes.

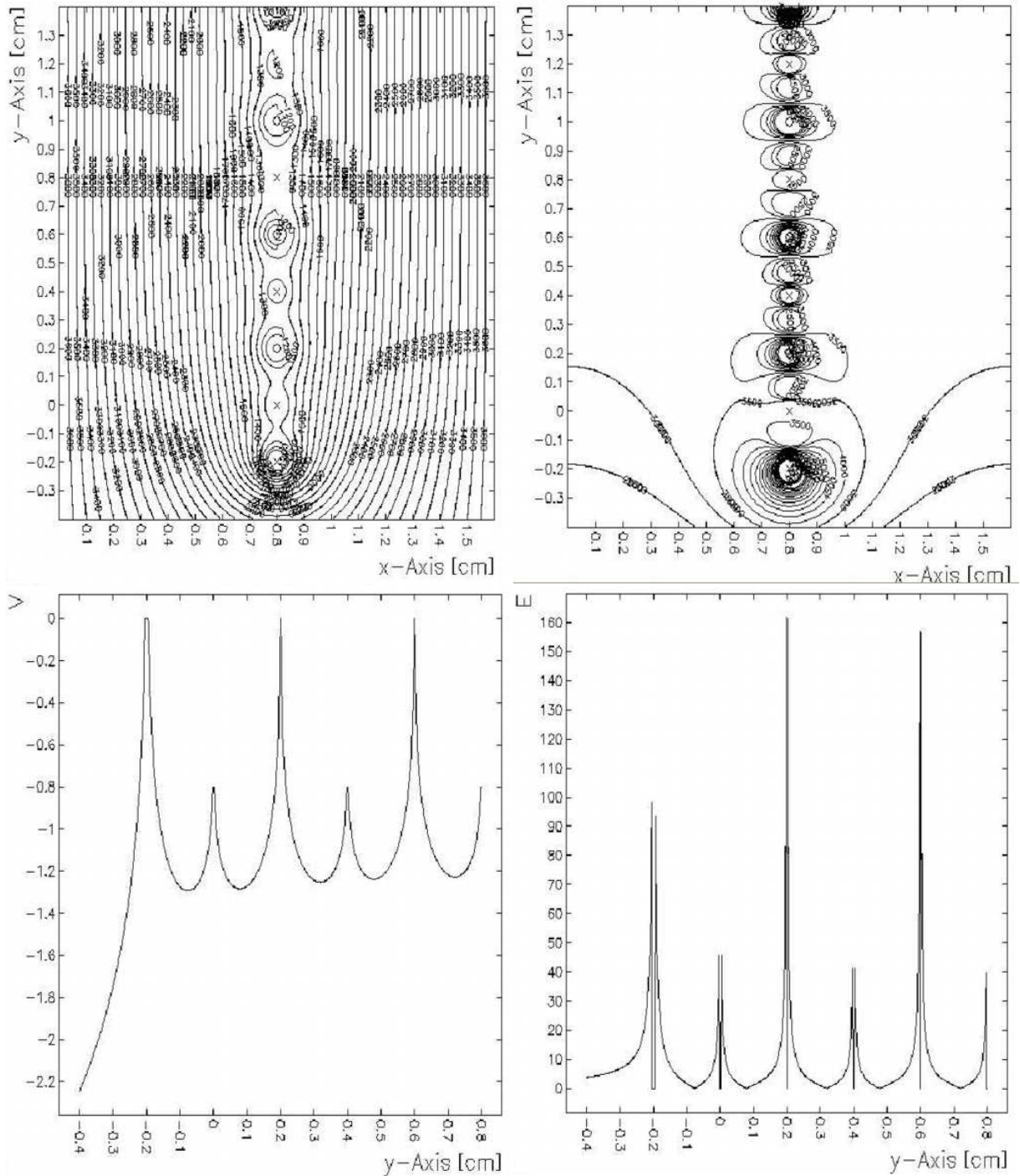


FIG. 3.7: Top left shows contours of V , and top right shows contours of E (in V/cm) around the guard and signal wires at one edge of the wire plane. Note that the wire plane starts with two guard wires before the alternating pattern starts. Guard wires are marked with crosses and signal wires are marked with circles. Bottom left shows the electric potential and bottom right shows the electric field in the plane of the wires. The signal wires are situated at the taller peaks, while the guard wires are situated at the shorter peaks. All was calculated with GARFIELD for -3.7 kV on the high voltage planes and -800 V on the guard wires. Signal wires are $20 \mu\text{m}$ and guard wires $50 \mu\text{m}$ in diameter, with the last guard wire $100 \mu\text{m}$ in diameter and grounded.

3.3.3.3 Printed circuit board

The design of the printed circuit board (PCB), which was made by the electronic department at iThemba LABS, follows that of the original VDC. Both the X and the U PCBs were made to be of length 936 mm and width 417 mm. They were manufactured by CIREP, a French company, and fixed to the stesalit chassis with araldite glue. The PCB is 2.5 mm thick, while the stesalit was originally 6.2 mm thick. The stesalit side was machined to provide a uniform overall thickness of 8 mm in order to fit between the HV and the signal wire planes.

3.3.3.4 Wires

The majority of the guard wires, used to make the electric field in the drift region more uniform and to reduce cross talk between adjacent drift cells [71], are made of 50- μm -diameter gold-plated tungsten. However, the first guard wire on each end has a diameter of 100 μm . The signal wires, which are interspersed between the guard wires, are made of 20- μm -diameter gold-plated tungsten. Both wire planes start with two guard wires, and then have alternating signal and guard wires until they end off with two guard wires. The U plane in Fig. 3.8 [74] contains a total of 146 guard wires and 143 signal wires, while the X plane in Fig. 3.9 [74] contains a total of 201 guard wires and 198 signal wires. Geometrical considerations, namely that the size of the medium dispersion focal plane is 800 mm \times 100 mm, led to the decision to make both the X and the U wire frames of length 800 mm and height 100 mm in order to cover this area. The wires were correctly spaced and fixed to wire transfer frames at the Research Centre for Nuclear Physics (RCNP) in Osaka, Japan. This was done with the correct tension of 110 g on the 50- μm guard wires and 50 g on the 20- μm signal wires to prevent wire sagging. The wires were then soldered onto the PCB at iThemba LABS. A negative voltage of about 500 V was applied to all the guard wires.

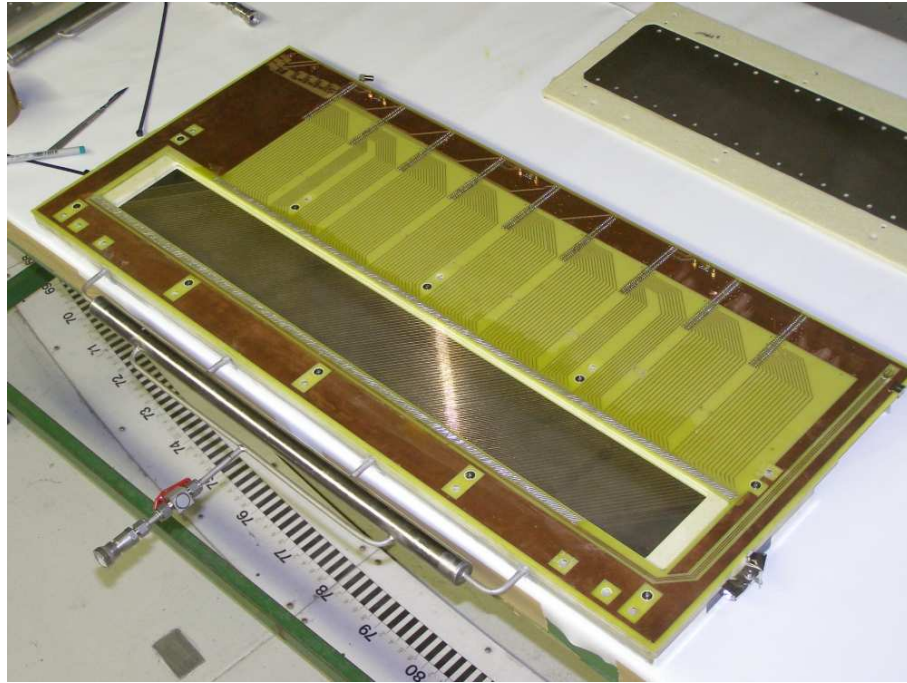


FIG. 3.8: The soldered U-wire plane opened up to display its wires and PCB.

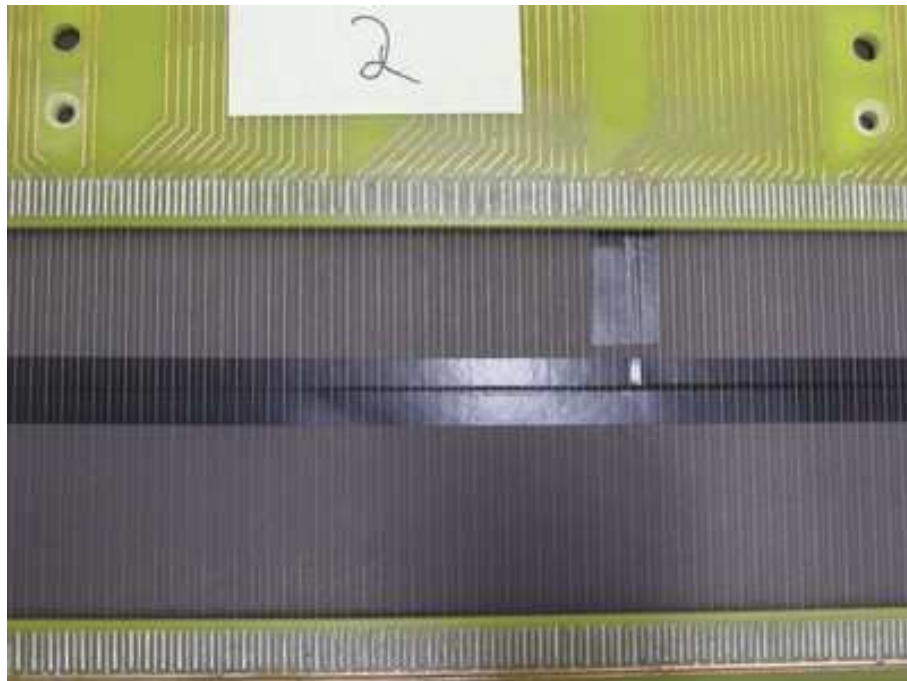


FIG. 3.9: A section of the soldered X-wire plane illustrating the guard wires and the signal wires with their associated signal wire tracks.

3.3.3.5 High voltage planes

The three high voltage (HV) planes were made of 20- μm thick aluminium foil and separated from each other by a distance of 16 mm. These HV planes have to be flat without any surface irregularities to ensure spark-free operation at voltages of 3 kV and higher. The Al foil stretching procedure is outlined below and illustrated in Fig. 3.10:

1. The Al foil is fixed to the stretching frame with duct tape.
2. Around the outer edge of the stretching frame is a groove which is connected to a vacuum pump. Switching on the pump results in the Al foil being pulled in all directions, thus smoothing out creases and other surface imperfections.
3. In the meantime Araldite glue is applied to the stesalit frame on which the Al plane is to be fixed.
4. The stretching frame with the stretched Al foil is then placed on top of the stesalit frame and thus the Al foil is glued to the stesalit frame. Lead weights are added to ensure proper glueing.
5. The weights are removed, and the final, stretched Al HV frame is ready.

During this experiment, a high voltage of 3.6 kV was applied to this plane.

3.3.3.6 Drift chamber gas

Two 25- μm -thick mylar planes were used to isolate the interior of the VDC from the atmosphere. The volume between the cathode planes is filled with a gas mixture of 90% Argon and 10% CO_2 . The Ar- CO_2 gas mixture is cheap, non-flammable and poses no possibility of polymerization endangering the long-term properties of the drift chamber. It is also possible to buy high-pressure bottles filled with the correct gas mixture of Ar- CO_2 . For a gas mixture of Ar- CO_2 at voltages between 3.5 and 4 kV, one may vary the composition of CO_2 over a reasonably wide range around 10% and still have the same efficiency. For a gas mixture of Ar-isobutane, which is also commonly used in drift chambers even though it is flammable and expensive, this efficiency plateau is much narrower. These effects are clearly illustrated in Ref. [75], and have influenced the choice of gas mixture used at iThemba LABS.

3.3.3.7 Sealing

Gas leakage is a major concern in drift chambers as it can lead to leakage current and sparking in the detector. Therefore effective sealing of the gas chamber and pipes is of utmost importance.



FIG. 3.10: The HV stretching procedure. Top left and right the Al foil is being prepared and fixed to the stretching frame. Middle left is shown the vacuum stretching of the Al. In the middle right the glue is being applied. At bottom left the weights are applied. Bottom right shows the final product. Dr Ricky Smit and Dr Hiro Fujita are the two scientists who feature in this figure.

O-rings are used to provide sealing between the stesalit frame components. Those used were made of Angst & Pfister natural sponge rubber, which is a very soft material.

The VDC was tested for gas leaks by flowing the chamber gas through the detector and applying soapy water to the outsides with a small brush to see where bubbles form. These places were then sealed with normal Silicon sealer. With gas flowing through the detector, high voltage testing could be performed on the detector.

3.3.4 Paddle scintillators

The BC-408 plastic scintillator material manufactured by Saint Gobain Crystals [76] was employed in the focal plane detector package. The scintillating material BC-408 was used because it is suitable for detecting α -particles, protons and other charged particles, and also because its principal applications are for large area and time of flight (TOF) measurements.

Three 122 cm \times 10.2 cm plastic scintillator detectors of different thicknesses (also referred to as paddle detectors because of their geometry) were positioned close to the focal plane just downstream from the drift chambers. The scintillators were wrapped in sheets of aluminized mylar, as shown in Fig. 3.12, in order to make them light tight. A photomultiplier tube was connected via adiabatic light guides as in Fig. 3.11, to both ends (left and right) of each paddle scintillator. The light guides were also made by Saint Gobain Crystals [76].

The plastic scintillators are used for particle identification (PID) through ΔE - ΔE PID spectra and to provide the common time signals for the collection of drift-time data. Particles incident on the focal plane first pass through the VDC, where gas molecules are ionized, and then reach the paddle scintillators within an extremely short time. Three different thicknesses of scintillator were available for the experiment: 1/8", 1/4" and 1/2". These were arranged in the following different configurations during the course of the experiment:

- The 1/8"-thick scintillator, referred to as Paddle 1, was positioned behind the VDC followed by a 1/4"-thick scintillator (Paddle 2) and a 1/2"-thick scintillator (Paddle 3). Paddle 1 and Paddle 2 were used together as trigger detectors, while Paddle 3 was used to veto energetic particles that passed through the first two scintillators. In this configuration, the paddles were placed at an angle of 56.25° with respect to the VDC, so that they were perpendicular to the particles passing through them (see Fig. 3.2). In this way, the minimum effective thickness of material is presented for the particles to pass through. This is important since the energy loss of some particles may be too high to allow for passing through the first scintillator if the effective thickness is too large.
- In another setup, data were recorded with valid events triggered only by Paddle 1, with the paddles still perpendicular to the particle ray. This was to test whether some particles still failed to reach Paddle 2 in the initial setup.
- For the final part of the experiment, the paddles were placed parallel to the VDC and Paddle 3 was removed, so there was no veto paddle in place. This new paddle angle was used to increase the effective thickness of material to look for particles that are energetic enough to pass through all the paddles with an increased effective thickness. Data were

recorded with Paddle 1 (1/8") and Paddle 2 (1/4") as trigger detectors, and also with Paddle 1 only. For the runs with only Paddle 1 as trigger, 1/2"- and 1/8"-thick scintillators were used on different occasions.

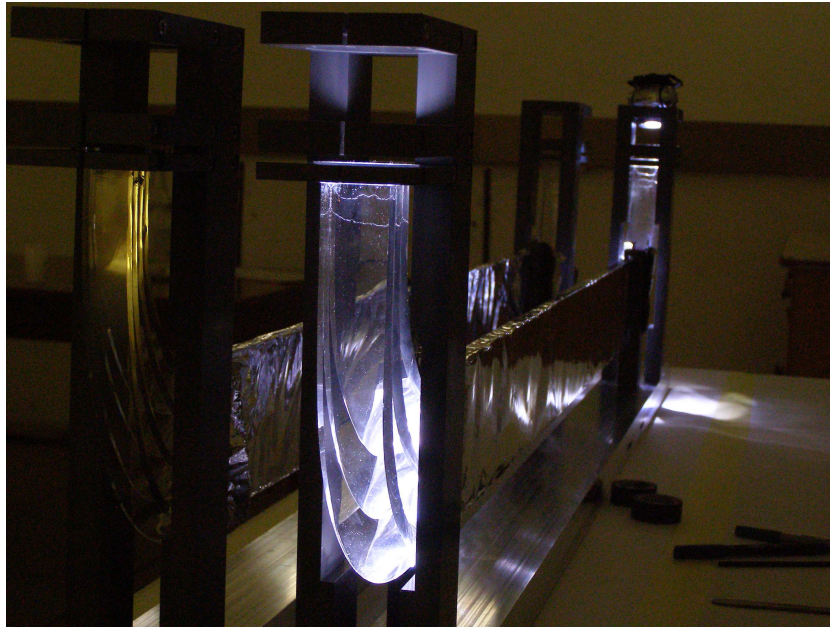


FIG. 3.11: The 1/2" and 1/4" paddle scintillators, illustrating the light guides. The photomultiplier tubes are not yet installed in this figure.



FIG. 3.12: One side of a paddle scintillator wrapped in aluminized mylar with a photomultiplier tube connected to the light guide.

3.4 Electronics

Electronic modules adhering to the Nuclear Instrumentation Module (NIM) and VME standards were used in the electronic setup to convert detected events into electronic signals that could be processed by the MIDAS computer software [59]. Signals from the paddles and the VDC were processed in the spectrometer vault, while the measurement of beam current was performed with modules in the data room.

3.4.1 Paddle signals

A block diagram of the trigger logic electronics used to process events in the spectrometer vault is presented in Fig. 3.13. The output pulse from each of the six photomultiplier tubes associated with the three paddle scintillators was fed into a linear fan-out (Lin Fan). For the first two paddles, Paddle 1 and Paddle 2, one of the two outputs associated with the linear fan was delayed by 150 ns before serving as an input to a QDC, while the other served as an input to a constant fraction discriminator (CFD). For the third paddle, the veto paddle, there was only the output that served as an input to the CFD. In order to obtain accurate timing for the events from the paddles, the outputs from the two CFDs associated with each of the paddles were both fed into a single mean timer. The output from the mean timer then served as an input to a discriminator, after a delay of 20.5 ns in the case of Paddle 2. The outputs from the discriminators were all fed to a four-fold logic unit (4FLU), where paddle coincidence events were selected with the following logic requirements:

- For most of the recording of data, an event trigger was generated whenever the paddle coincidence pulse fulfilled the logic requirement of $(P1 \cdot P2) \cdot \overline{P3}$ where $P1$ is Paddle 1, $P2$ is Paddle 2 and $P3$ is the veto paddle.
- This was later changed to $(P1 \parallel P1 \cdot P2) \cdot P3$ in order to see whether some events triggered $P1$ and reached $P3$, but somehow did not trigger $P2$.
- For the final setup, after the paddles were adjusted to be parallel with the VDC, $P1 \cdot P2$ was used as a trigger.
- $P1$ only was also used on occasions before and after the paddles were placed in parallel with the VDC.

The output from the 4FLU, which selected paddle coincidence, was fed through two discriminators to another 4FLU. This second 4FLU received the RF signal after it had passed through an attenuator and a discriminator. Whenever this 4FLU registered paddle coincidence together

with the RF signal, it sent an output to the time-of-flight (TOF) time digitizer channel (TDC). The second output from the first 4FLU served as the trigger input for TDC counting, while the other was sent to the TDC channels associated with the VDC signals. The trigger input for TDC counting opened a gate of 20 μs within which the TDCs could register RF and VDC signals and assign times to them. From the difference between the time of the trigger signal and that of the RF and VDC signals, the TOF and drift times could be established.

3.4.2 Dead time measurement

The DAQ dead time measurement was achieved with a pulser and two scaler modules, the inhibited and the uninhibited. The DAQ effective dead time was measured by comparing the amount of inhibited and uninhibited pulses recorded by the two scalars.

3.4.3 Pre-amplifier cards and TDCs

The signal wires were connected via signal wire tracks on the PCB (see Figs. 3.8 and 3.9) to the Technoland PTM 005 16-channel pre-amplifier cards. These pre-amplifier (pre-amp) cards amplify the signals from the signal wires and perform a discriminatory function to ensure that only the proper signals go through to the TDCs. The pre-amp cards were connected to 16-channel twisted pair ribbon cables which were connected via CAEN A967 cable adapters to the CAEN V1190A 128-channel multihit TDC. Altogether 13 pre-amp cards were used for the 198 signal wires in the X-wire plane, while 9 pre-amp cards were required for the 143 signal wires in the U-wire plane. The X-plane pre-amp cards were placed on the same side as the signal wire tracks, while the U-plane pre-amp cards were placed on the opposite side of the signal wire tracks.

3.4.4 Current integration

The current at the beam stop was sent through to the dataroom where it was fed into the Brookhaven Instruments Corporation Model 1000C Current Integrator (CI). At full-scale current setting, the CI generates output pulses at a frequency of 1 kHz. The digital output from the CI was sent through a timing single channel analyser (Timing SCA), to a discriminator. The output from the latter formed the input to a VME scaler module. The scaler, in conjunction with the known CI full-range setting, was used to calculate the integrated current, corrected for the data acquisition dead time.

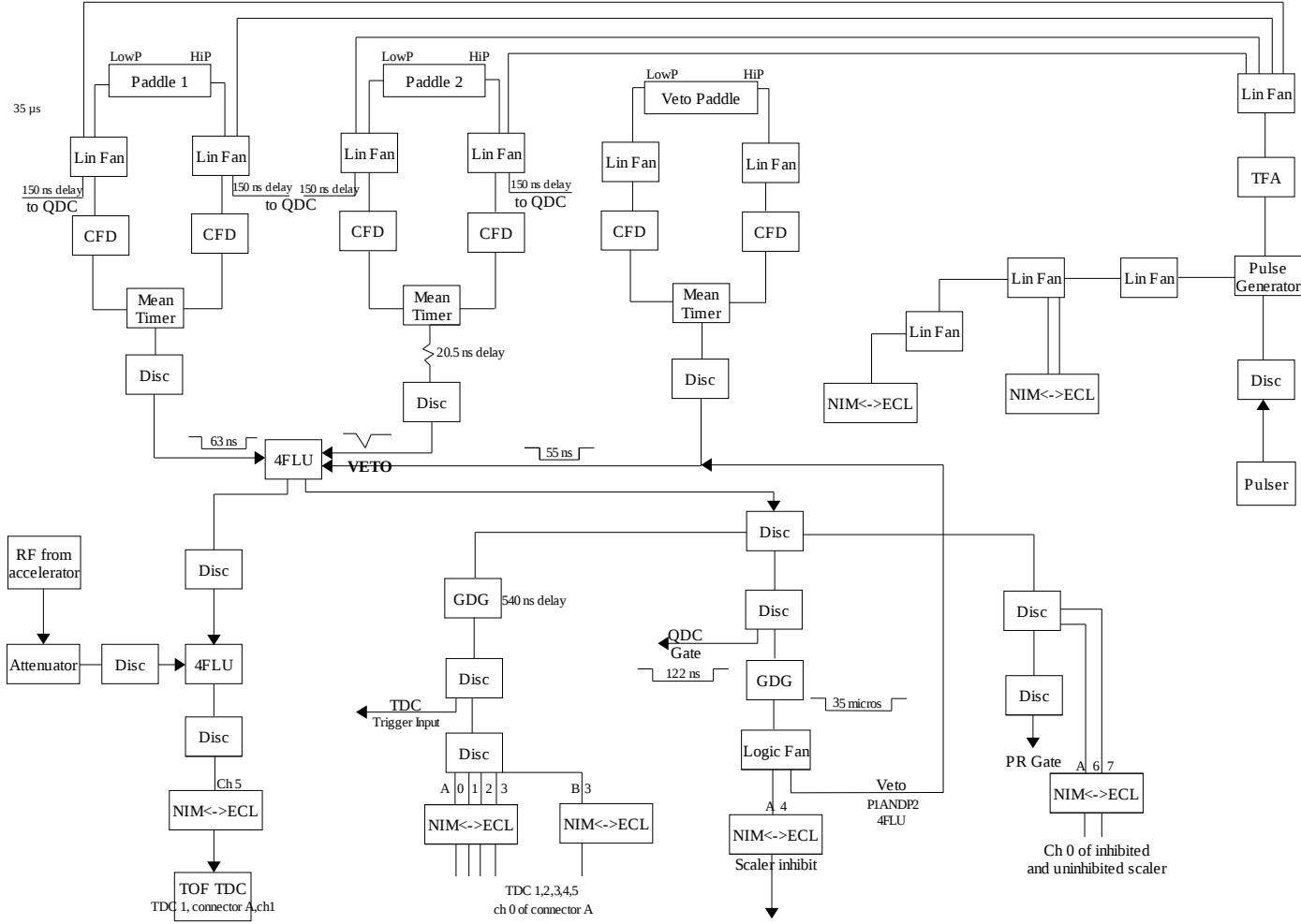


FIG. 3.13: Diagram of the trigger electronics

3.5 Data acquisition

VME hardware was used for capturing the electronic signals. VME scaler and CAEN V792 QDC modules, and the TDC modules described in section 3.4.3 were used. The 12-bit QDC has a full scale range of 400 pC spread over $2^{12} = 4\,096$ channels. Each TDC has a resolution of 100 ps.

MIDAS software was used to process the electronic signals. MIDAS is a data acquisition package which was written in C++ under the GPL (General Programming License), and is used in nuclear and particle physics experiments. The MIDAS software package consists of a library which can be used for data transport and a set of programs for data logging and system management. Valuable features include a fast online database, on which experimental configuration can be stored, and a web interface, which makes the experiment remotely controllable. Additionally, a slow control system is integrated for setting and measuring variables such as detector HV. MIDAS software may be used for purposes covering a wide range of complexity i.e. for test systems with only one PC connected to the hardware, or for experiments where several front-end and analysis computers are involved. MIDAS is mostly used with VME, CAMAC or FASTBUS hardware [59].

3.6 Experimental procedure

The spectrometer and its electronics were set up as described in the previous sections. The scattering chamber was pumped down to the required vacuum ($P \sim 10^{-5}$ mbar). The magnetic fields were set by adjusting the currents in the electromagnets via remote control from the data room. The appropriate currents for the six different types of field settings (fieldsets), each associated with their own reaction products, namely d , t , ${}^3\text{He}$, ${}^4\text{He}/p$, ${}^6\text{He}$ and ${}^8\text{He}$, were calculated using the DELPHI program SPEXCIT [77], which was written at iThemba LABS. Table 3.1 shows the currents which were calculated and the magnetic fields which should be generated by these currents according to SPEXCIT. Paddle and VDC high voltages were also set remotely from the data room. A scintillating viewer known as a Hatanaka “mesh”, together with the ZnS screen in the target ladder, was used to align and focus the beam on target [66].

During the experiment, the paddle and veto combinations were changed on a few occasions as described in section 3.3.4. After the first good pulser run was obtained, data were taken with the beam on the ${}^{27}\text{Al}$ target for a duration of roughly 21 hours, with typical run times of about 30 minutes. Different field settings for measuring reactions with higher cross sections than that of the (${}^3\text{He}, {}^8\text{He}$) reaction were investigated in order to gain confidence in the experimental setup and to understand the detector response when measuring different particles. This step

was necessary since this was the first experiment performed on the K600 light ion spectrometer with a ^3He beam, and the $(^3\text{He}, ^8\text{He})$ reaction is very difficult to measure. The first measurement was of the elastic $^{27}\text{Al}(^3\text{He}, ^3\text{He})^{27}\text{Al}$ reaction, which is the easiest because it has the highest cross section. The field setting was then changed to measure the $^{27}\text{Al}(^3\text{He}, ^4\text{He})^{26}\text{Al}$ and the $^{27}\text{Al}(^3\text{He}, p)^{29}\text{Si}$ reactions. These two reactions have very similar optimal field settings since the K-values of their reaction products were found to be very close, hence both the ^4He and the p particles were measured with the same field settings. The field settings were adjusted for a range of energies to ensure that a wide enough total energy range was covered to observe both particles. The veto was switched on and off on occasions in order to understand its effect, and the empty target frame was used along with the beam blocker collimator to check for background from the frame. After a successful measurement of ^4He particles, the field setting was changed and the veto left unchanged for measuring the $^{27}\text{Al}(^3\text{He}, ^6\text{He})^{24}\text{Al}$ reaction. A thicker target was also used in order to increase the count rate, but still no conclusive measurement of ^6He could be attained with the paddles perpendicular to the beam direction. The $^{27}\text{Al}(^3\text{He}, d)^{28}\text{Si}$ reaction was measured with the paddles still at the same inclination. Data were taken with this setup and the optimal field settings for measuring the $^{27}\text{Al}(^3\text{He}, ^8\text{He})^{22}\text{Al}$ reaction.

A successful measurement of the ^6He particles could not be attained with the paddles perpendicular to the beam, therefore the paddles were moved to be parallel with the VDC and at an angle of 56.25° with respect to the beam, thus increasing the effective thickness of the paddles in order to see whether some high energy particles could be more clearly observed. Measurements were made with this paddle setup and the optimal ^6He field setting. The $^{27}\text{Al}(^3\text{He}, t)^{27}\text{Si}$ reaction was measured with this paddle setup, and measurements of all the previously measured reactions (for ^3He , $^4\text{He}/p$, d) were also taken with this setup in order to understand the effect of the change in paddle angle.

Particle	Magnet	Current [A]	Field [T]
${}^3\text{He}$	D1	344.41	0.86654
Q = 0	D2	342.62	0.88022
	Quadrupole	-425.9	
d	D1	582.94	1.45037
Q = 6.091 MeV	D2	581.6	1.47458
	Quadrupole	-715.87	
t	D1	726.04	1.71246
Q = -4.8 MeV	D2	754.11	1.75035
	Quadrupole	-847.72	
${}^4\text{He}, p$	D1	400.83	1.00753
Q = 7.52 MeV	D2	398.49	1.02341
	Quadrupole	-495.39	
196 MeV ${}^6\text{He}$	D1	455.76	1.14350
Q = -19.8 MeV	D2	453.01	1.16159
	Quadrupole	-561.99	
202 MeV ${}^6\text{He}$	D1	462.91	1.16118
Q = -19.8 MeV	D2	460.1	1.17956
	Quadrupole	-570.86	
${}^8\text{He}$	D1	496.82	1.24487
Q = -52.047 MeV	D2	493.64	1.26459
	Quadrupole	-612.53	

TABLE 3.1: This table shows the current settings which were applied to the magnets, in the 3rd column, in order to produce the optimal magnetic fields for each particle in the 4th column. D1 refers to dipole 1 and D2 refers to dipole 2. The dipole ratio D1/D2 was kept at 0.99 throughout.

CHAPTER 4

Data analysis

Off-line data analysis was performed with a C++ code developed at iThemba LABS which translates the raw MIDAS files into ROOT files. This code was written especially for the new focal plane detector package of the K600 spectrometer. The code, f-plane.c, populates histogram and TTree data structures for ROOT. Subroutines are defined for associating a wire number with each TDC channel number from the raw data, calculating the horizontal and vertical positions of particles at the focal plane and tracing the exact paths of particles through the wire plane. In the “init” routine, folders are prepared for all the histograms and ROOT trees are defined for the variables that are most important for the data analysis, e.g. time-of-flight (TOF), paddle output and wire-plane position, resolution, efficiency, etc. In the “event” routine, the histograms are filled with experimental data that satisfy all logical requirements.

4.1 Methods of particle identification

Identification of particles observed in the focal plane detectors may be achieved by obtaining energy-loss and time-of-flight (TOF) information with the paddle scintillation detectors. Obtaining energy-loss information is a useful method of particle identification (PID), since different types of particles lose different amounts of energy in a medium. According to the Bethe-Bloch equation [78], the rate of energy loss with respect to distance travelled of a charged particle moving through a material is proportional to its charge squared and inversely proportional to its velocity squared:

$$-\frac{dE}{dx} \propto \frac{(Ze)^2}{v^2} . \quad (4.1)$$

Hence, any particle with a characteristic charge and velocity will have its own characteristic energy-loss in the paddle scintillation detectors. For paddle 1 and paddle 2, the pulse heights of the left (Pad1left and Pad2left) and right (Pad1right and Pad2right) photomultiplier tubes were measured. By plotting (Pad1left) \times (Pad1right) vs (Pad2left) \times (Pad2right), a two-dimensional PID histogram as shown in Fig. 4.1 was generated. Different loci on this PID spectrum represent different particles (p , d , t , α , etc.). Each locus can be selected and investigated by setting a software gate around the relevant region.

Each reaction product that leaves the target with its own characteristic mass and energy has its own characteristic velocity. This logically implies a unique time-of-flight (TOF) range for each type of particle travelling through the same flight path. Thus for a given magnetic field a

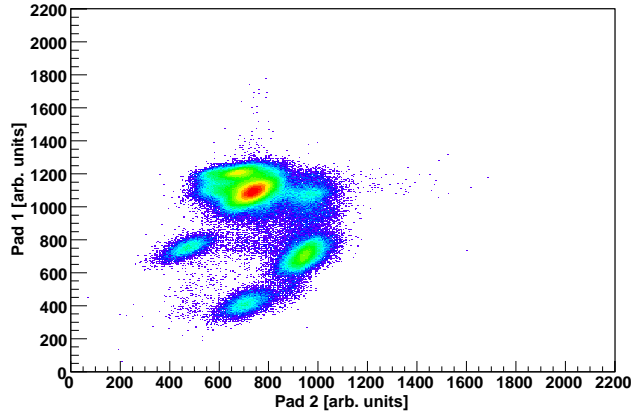


FIG. 4.1: A two-dimensional PID spectrum for the $^{27}\text{Al}(^3\text{He},^3\text{He})^{27}\text{Al}$ reaction.

minimum and maximum possible TOF may be assigned to any particle for which the velocity may be deduced from its known mass and energy. An example of a TOF spectrum with peaks of different particles corresponding to their TOF ranges is shown in Fig. 4.2. Minimum and maximum possible flight paths for a particle from the target to the focal plane of 7.78 m and 8.87 m are estimated for the spectrometer.

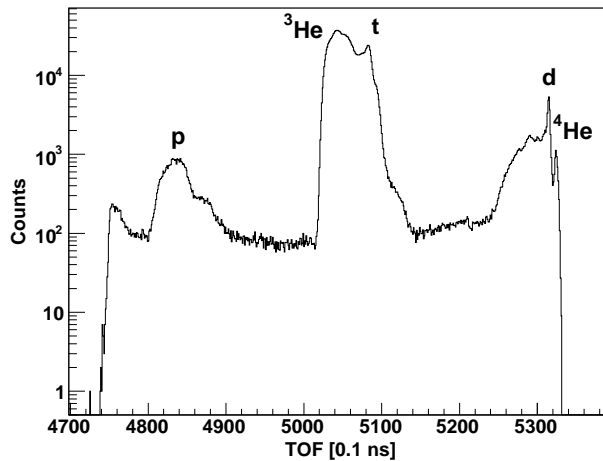


FIG. 4.2: TOF spectrum for the $^{27}\text{Al}(^3\text{He},^3\text{He})^{27}\text{Al}$ reaction.

4.2 VDC operation

Focal-plane coordinates are determined for all valid VDC events by using drift time and wire position information for these events. The drift times, which are measured from the point of primary ionization to the point where avalanching occurs in each cell, are used together with the

known average drift velocity to determine the drift distance. Hence the distance from the signal wire to the position where the particle first passes through the drift cell is determined. High voltage is applied to the HV planes, thus providing an electric field that causes the electrons to drift towards the anode signal wire plane. The electric field is constant, except for the regions very near to the signal wires. This constant electric field over the drift region ensures a linear time-to-position relationship.

Drift distance and wire position information for the signal wires situated around the wire that is associated with the minimum drift time is then used to determine focal plane coordinates for all valid VDC events. A valid VDC event is defined in section 4.2.5.

4.2.1 Determining the focal plane position

In order to determine accurate position information for particles in a VDC, the drift time characteristics of the VDC must first be known. Once the characteristic drift time distribution $\frac{dN}{dt}$ is known, it is possible to determine the distance from the signal wire to the position where the particle passed through the drift cell, hence the drift distance of the electrons. The drift distance for each signal wire is calculated as

$$y(t) = \left(\frac{dN}{dy}\right)^{-1} \int_{t_0}^t \left(\frac{dN}{dt'}\right) dt' , \quad (4.2)$$

where

- t_0 is the arrival time of the particle in the drift cell,
- t is the time at which the pulse appears at the anode, and
- $\frac{dN}{dy}$ is a measure of the spatial distribution of events in the drift cell, obtainable from wire position information.

A characteristic drift time distribution may be obtained by uniformly illuminating the focal plane with particles so that the average timing response of all the signal wires can be measured. A so-called “white spectrum” is generated. This distribution of drift times will be proportional to the average drift velocity

$$\frac{dN}{dt} \propto \omega(t) . \quad (4.3)$$

The uniformity of the spatial distribution of the events ensures that $\frac{dN}{dy}$ remains constant. Hence it is possible to set up a lookup table (LUT) which links any drift time to a corresponding drift distance.

This method, the so-called integral-time-spectrum method [79], is not perfect since it has two inherent inaccuracies, namely that:

1. It is impossible to obtain perfect uniformity in this white spectrum.
2. It is assumed that the maximum measured drift time corresponds to the maximum geometrically possible drift distance (8 mm in this case), which is not true in practice with a drift cell width of 4 mm [79].

In the case of the U plane, one must take into account the fact that the wires are inclined at 50° with respect to the horizontal in order to obtain horizontal (x) and vertical (y) focal plane position information.

4.2.2 Vertical position determination

Vertical (y) position determination is achieved by applying U- and X- wire plane information to the following equation:

$$y = \left(x - \frac{u}{\sin\theta_U} - \frac{d}{\tan\theta_{fp}} \right) \tan\theta_U , \quad (4.4)$$

where u and x represent U- and X-wire plane position information, $\theta_U=50^\circ$ is the U-wire angle, θ_{fp} is the incident angle of a particle on the focal plane, and $d=16$ mm is the separation between the U- and the X-wire planes. A derivation of Eq. 4.4 follows in the next paragraph.

After passing through the U-wire plane, the incident particle must first travel a distance of 16 mm before reaching the X-wire plane. In order to overlap the U-wire and the X-wire planes to calculate y , an offset in the calculated X-wire position is required. It can be seen from Fig. 4.3 that the horizontal offset should be

$$x_{offset} = \frac{d}{\tan\theta_{fp}} . \quad (4.5)$$

Using the information in Fig. 4.4, it can be shown that the offset in the U-plane position may be calculated from x_{offset} as

$$u_{offset} = x_{offset} \cdot \sin\theta_U , \quad (4.6)$$

which with Eq. 4.5 means that

$$u_{offset} = \frac{d \cdot \sin\theta_U}{\tan\theta_{fp}} . \quad (4.7)$$

In Fig. 4.4, x is the calculated horizontal position. Clearly $AB = x - AD$ and

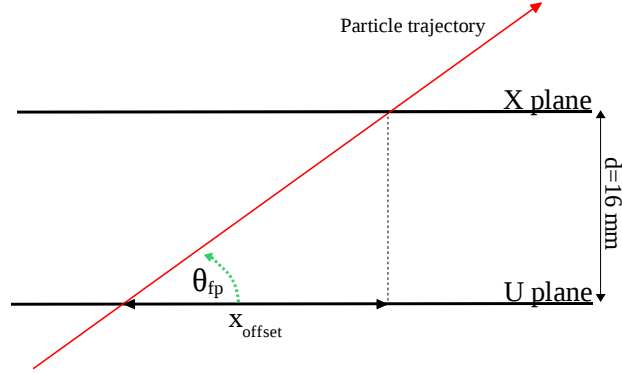


FIG. 4.3: Particle trajectory through U and X planes, illustrating the offset in x between the two wire planes.

$$\frac{u + u_{offset}}{AD} = \sin\theta_U , \quad (4.8)$$

which leads to

$$AB = x - \frac{u + u_{offset}}{\sin\theta_U} . \quad (4.9)$$

The vertical position must be

$$y = BC = AB \cdot \tan\theta_U , \quad (4.10)$$

which yields with Eq. 4.9 that

$$y = \left(x - \frac{u + u_{offset}}{\sin\theta_U} \right) \tan\theta_U . \quad (4.11)$$

By substituting from Eq. 4.7 into Eq. 4.11,

$$y = \left(x - \frac{u + \frac{d \cdot \sin\theta_U}{\tan\theta_{fp}}}{\sin\theta_U} \right) \tan\theta_U , \quad (4.12)$$

the vertical position is obtained.

4.2.3 Position resolution

The usual figure of merit for a drift chamber in terms of position resolution is the position accuracy σ_x obtainable in a single drift cell [67]. Consider any n -wire VDC event. The track is

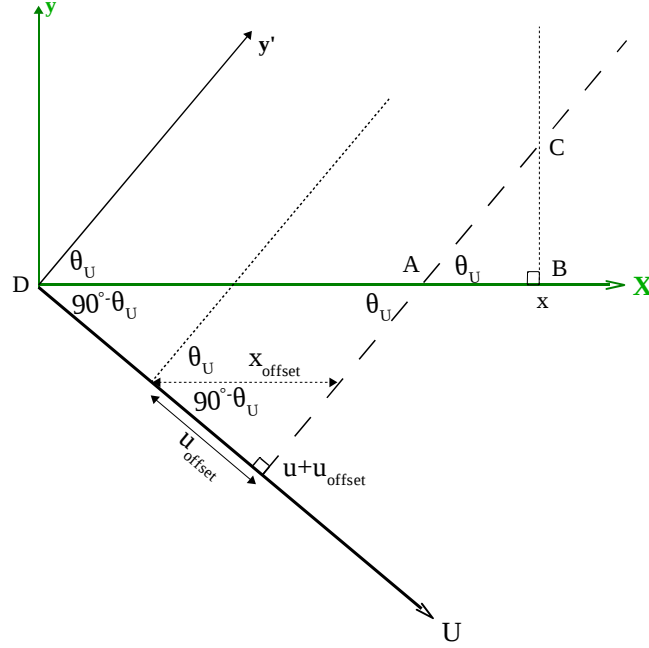


FIG. 4.4: X and U position axes with real y axis and tilted y' axis respectively at right angles with them. This figure illustrates how the offset in the U plane position u_{offset} , and the vertical position y may be determined.

at a constant angle on both sides of the wire plane, hence the difference in the slopes

$$D = \frac{d_{t(1)} - d_{t(2)}}{\text{wire separation}} - \frac{d_{t(n-1)} - d_{t(n)}}{\text{wire separation}} , \quad (4.13)$$

where $d_{t(i)}$ denotes the drift distance as calculated from the drift time t of wire i , should equal zero. In reality, however, because of statistical fluctuations, a distribution centred around zero is obtained if one calculates the difference in the slopes for a number of events [72]. The standard deviation of

$$D = (d_{t(1)} - d_{t(2)}) - (d_{t(n-1)} - d_{t(n)}) , \quad (4.14)$$

is related to the standard deviation of the drift distance (σ_{dd}) [67], as follows:

$$\sigma_D = 2\sigma_{dd} , \quad (4.15)$$

assuming that

$$\sigma_{dd} = \sigma_{d_{t(1)}} = \sigma_{d_{t(2)}} = \sigma_{d_{t(n-1)}} = \sigma_{d_{t(n)}} . \quad (4.16)$$

The standard deviation of the drift distance is referred to as the ‘intrinsic cell accuracy’. The intrinsic position resolution of the drift chamber is calculated as

$$FWHM_{pos} = 2.35 \times \sigma_{pos} = 2.35 \times \frac{\sigma_{dd}}{\sqrt{n}} , \quad (4.17)$$

$$\Rightarrow FWHM_{pos} = 2.35 \times \frac{\sigma_D}{2\sqrt{n}} . \quad (4.18)$$

where n is the number of wires used to determine the position [67].

4.2.4 The lookup table shift

It is unavoidable that there will be delays in the trigger signal that serves as a common signal for determining drift times in each of the drift cells. Therefore the drift times measured cannot be entirely correct. Incorrect drift times translate into incorrect drift distances in the lookup table. In Fig. 4.5, it can be seen that a shift towards shorter drift times translates into longer drift distances, whereas a shift towards longer drift times translates into shorter drift distances.

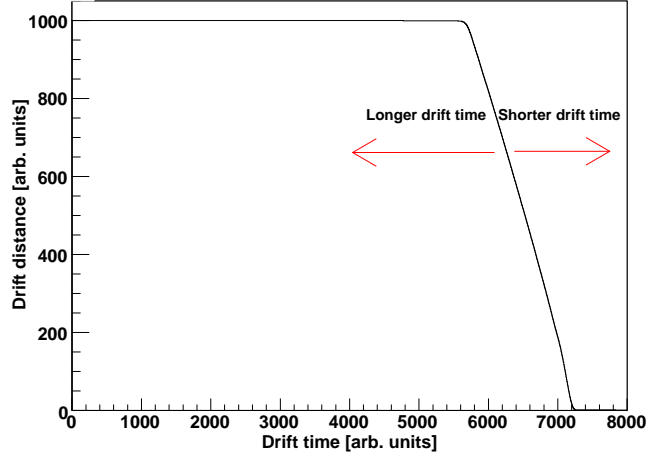


FIG. 4.5: The lookup table.

For good resolution, the projection of events on the Δ axis, where the term Δ is defined in terms of the drift times d_{i-1} , d_i and d_{i+1} for three consecutive wires $i-1$, i and $i+1$ associated with a specific event as

$$\Delta = \frac{d_{i+1} - d_{i-1}}{2} - d_i , \quad (4.19)$$

should be centred around zero. The spectra in Fig. 4.6 represent the projection of events on the

Δ axis where they are centred around zero (left), representing a properly shifted lookup table, and at two different maxima (right), representing a lookup table with an offset.

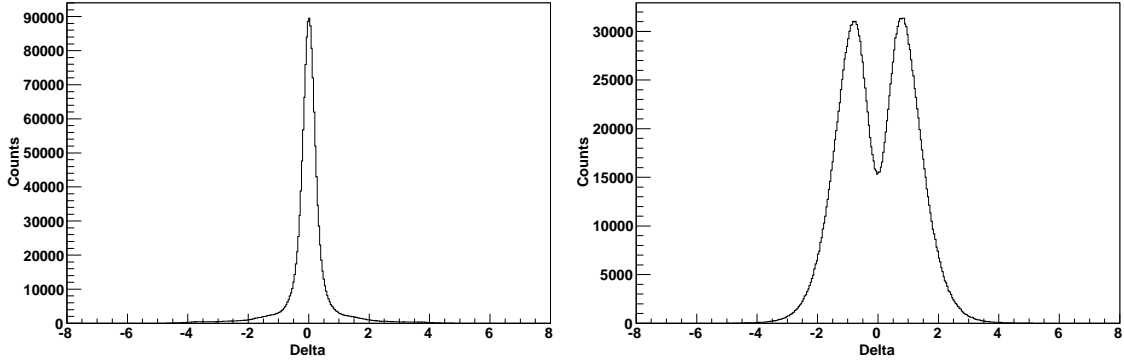


FIG. 4.6: Position resolution plots illustrating the projection of events on the Δ axis.

The spectra in Fig. 4.7 correspond to the spectra of Δ vs $b - b(int)$, where b represents the actual position where the particle crossed the wire plane, and $b(int)$ represents the integer position or the signal wire number where the particle crossed the wire plane.

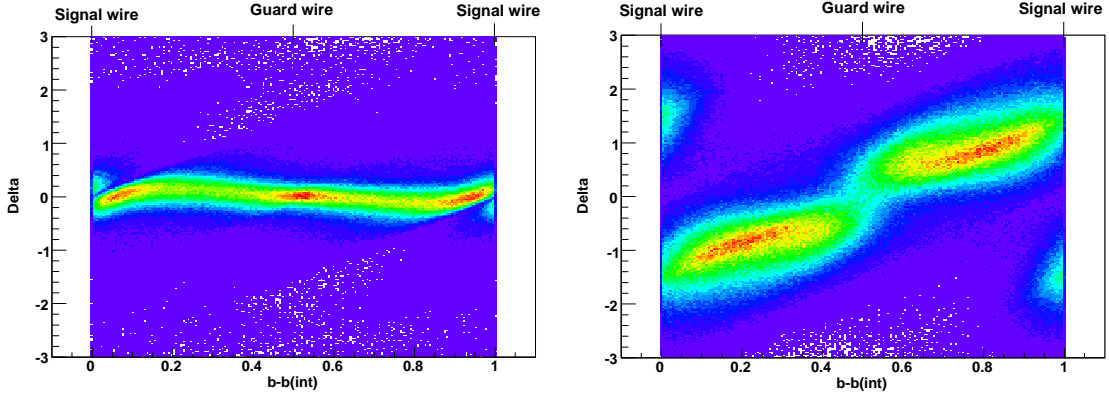


FIG. 4.7: Position resolution plots illustrating the projection of Δ on $b - b(int)$.

4.2.5 VDC efficiency

The raw wire hits per channel measured with the ^3He magnetic field settings is shown in Fig. 4.8. The good events were selected from all these wire hits and used to generate the position spectrum. The VDC efficiency ϵ was calculated as the product of the ratios of the good events to all the events registered by the two wire planes for a specific PID selection gate:

$$\epsilon = \frac{X1_{good}}{X1_{all}} \times \frac{U1_{good}}{U1_{all}} . \quad (4.20)$$

A good, or valid, event was defined as an event where, among other requirements, a minimum of three and a maximum of eight consecutive signal wires registered a hit as shown in Fig. 4.9. If these wires were not consecutive, a valid event could still be recorded if the gap in between wires did not contain more than three wires. A further constraint was that the drift times shown in Fig. 4.10 had to fall within a specified range. Efficiencies of 80-90% were typically measured during the experiment. In the case of the ^3He fieldset, efficiencies of about 82% in the X plane and 86% in the U plane were obtained. Under normal operating conditions with (p,p') reactions, efficiencies of 90-94% are usually obtained.

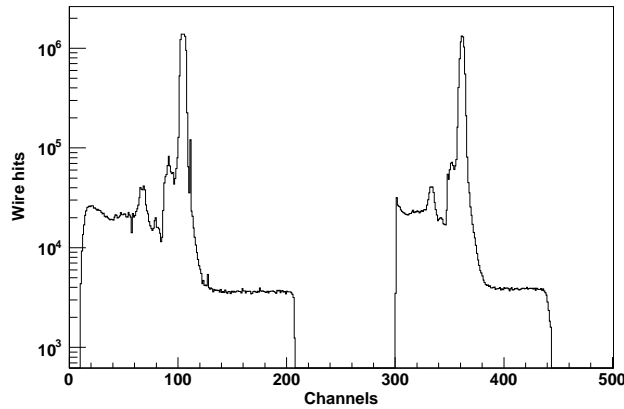


FIG. 4.8: The raw wire hits per channel is shown for both the X-wire plane (channel 0-208) and the U-wire plane (channel 300-445) for the ^3He fieldset.

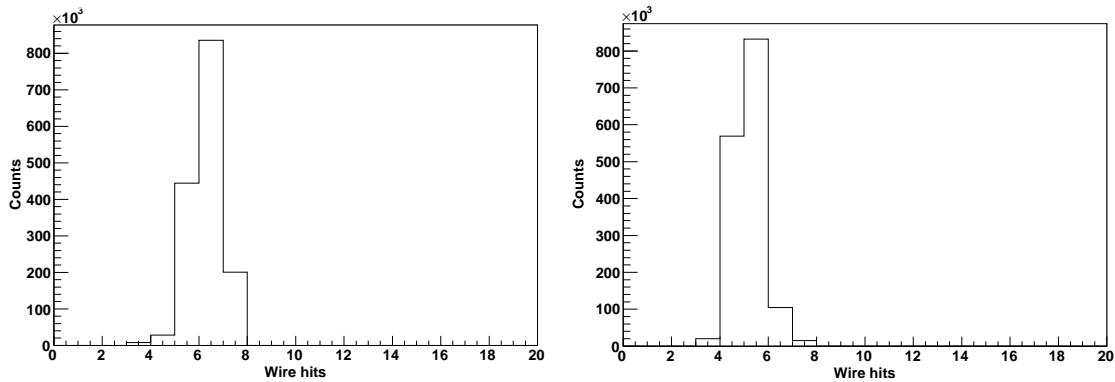


FIG. 4.9: The wire hits per event in the X plane is shown on the left, and in the U plane is shown on the right, indicating the events that fulfilled the minimum of three and maximum of eight signal wires requirement. The ^3He fieldset was used.

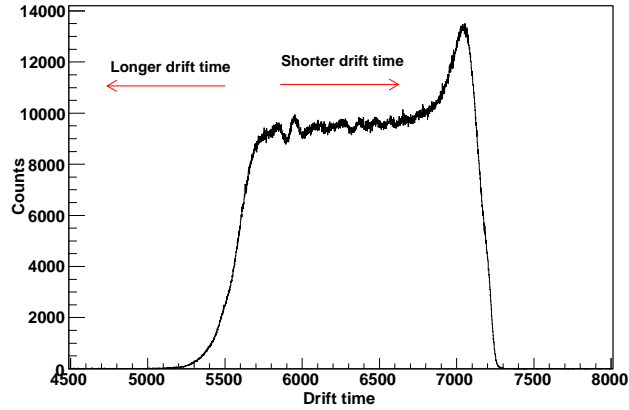


FIG. 4.10: The spectrum of all drift times measured by the X-wire plane for the ^4He fieldset. The peak to the right is for small drift times very close to the wires. It occurs because more electrons will have faster drift velocities in the regions radially near to the signal wires where the electron avalanching takes place. Faster drift velocities translate into shorter drift times.

4.2.6 The position spectrum

The position spectrum obtained with the ^3He magnetic field setting is shown in Fig. 4.11. The x-axis in Fig. 4.11 corresponds to focal plane position. Particles with different momenta, and therefore different kinetic energies, will end up at different positions in the focal plane of the spectrometer. From right to left, in focal plane position, the energy decreases and one sees higher excited states of the target nucleus. There exists an almost linear relationship between particle energy and focal plane position in the K600 spectrometer.

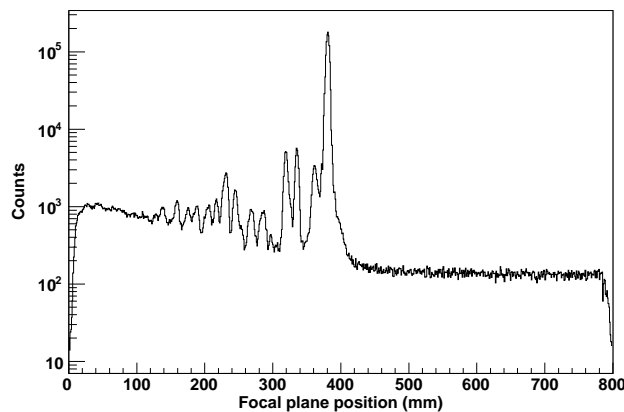


FIG. 4.11: The horizontal focal plane position spectrum for the ^3He beam on the ^{27}Al target without any PID selection gates. The prominent peak in this spectrum corresponds to the ground state of ^{27}Al .

4.3 Analysis of different fieldsets

This section presents the experimental results and interpretation thereof for each of the six different magnetic field settings which were investigated. The optimal field settings for measuring the different particles were investigated. This was done to gain confidence in the experimental setup and to understand the different reactions expected with the ^3He beam, which was not previously used together with the K600 spectrometer. The measurement with the ^8He field setting, which represents the aim of the experiment, is described last.

4.3.1 Analysis of the $^{27}\text{Al}(^3\text{He},^3\text{He})^{27}\text{Al}$ fieldset

Experimental data measured with the ^3He fieldset, and the paddles perpendicular to the beam, are shown in Fig. 4.12. The data were obtained with an 1/8" scintillator in paddle position 1 (Pad 1), a 1/4" scintillator in paddle position 2 (Pad 2), and a 1/2" scintillator in paddle position 3 (Pad 3). Events were recorded for Pad 1 triggering in coincidence with Pad 2. Pad 3 was used as a veto detector in order to eliminate the lighter hydrogen particles from the PID spectra. The K600 magnetic field, summarised in Table 3.1, was set to observe the elastic $^{27}\text{Al}(^3\text{He},^3\text{He})^{27}\text{Al}$ reaction for an incident beam energy of $E_{lab}=220$ MeV.

Of all the reactions investigated, the $^{27}\text{Al}(^3\text{He},^3\text{He})^{27}\text{Al}$ reaction was expected to have the highest cross section. Therefore it was investigated first as a basic test of the experimental setup. Rigidity calculations showed that, for the K600 magnetic field setting optimised for seeing the elastic ^3He particle as well as its low-lying states, no other prominent particles associated with low excitation energies were expected to fall within the same narrow rigidity range as ^3He which translates into the ^3He energy range of 211.93 - 248.24 MeV. The results of the rigidity calculations are summarised in Table 4.1.

Time-of-flight (TOF) calculations were performed using

$$TOF = \frac{d}{v}, \quad (4.21)$$

where d is the distance travelled by the particle and v is its velocity. In all the calculations that follow $d = 8.14$ m was used. A ^3He particle with a kinetic energy of 220 MeV will travel at a velocity of $0.37c$, where c represents the speed of light. Hence the particle velocity must be calculated relativistically

$$v = \sqrt{1 - \left(\frac{M}{E_{total}}\right)^2} \cdot c, \quad (4.22)$$

where $M = mc^2$ represents the rest mass energy and $E_{total} = M + E_{kinetic}$. For a 220 MeV ^3He beam, the time interval between different beam packets is 58.2 ns. The detector thus provided

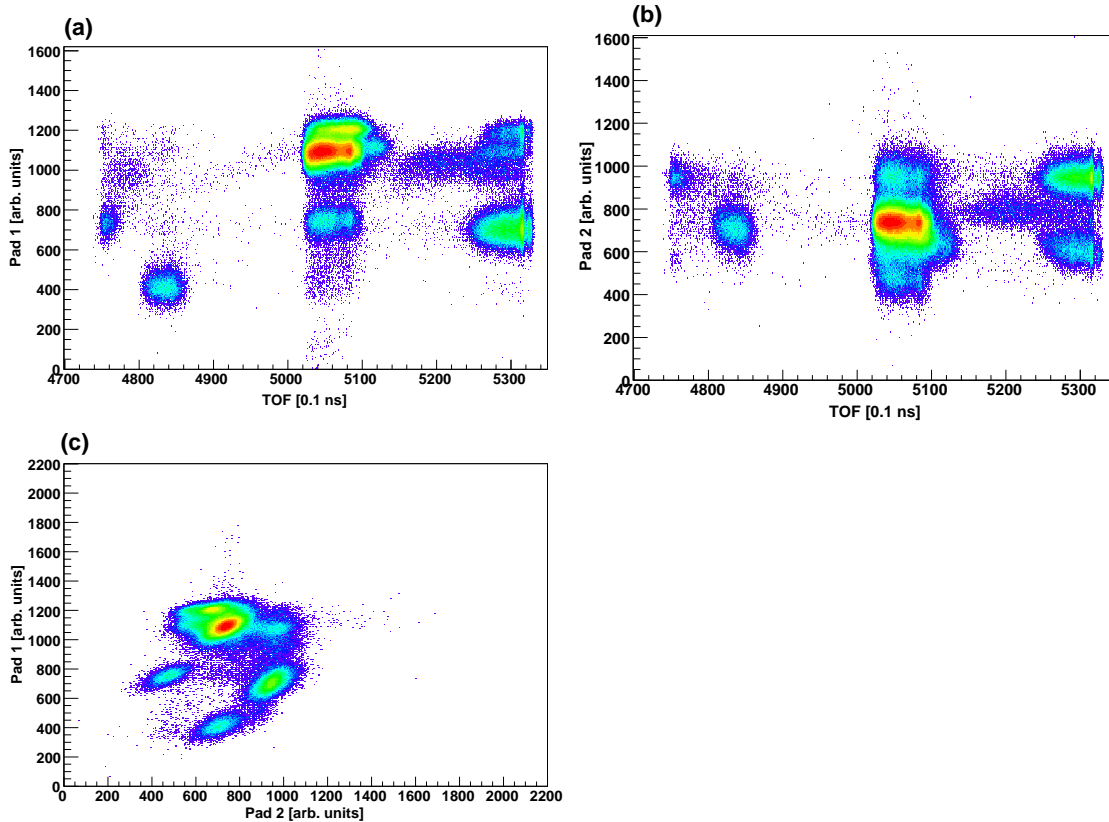


FIG. 4.12: PID spectra for the ^3He fieldset with a paddle set-up as described in the text. The Pad 1 vs TOF spectrum is shown in (a), the Pad 2 vs TOF spectrum is shown in (b), and the Pad 1 vs Pad 2 spectrum is shown in (c). Different loci all represent different particles.

a TOF range of 58.2 ns. In Table 4.1 it is seen that the TOF of many particles that reached the focal plane far exceeded this. Therefore it is possible for particles with different TOFs to be detected at the same time if they come from different beam packets. This gives rise to a ‘wrap-around’ in the TOF spectrum, i.e. an overlap of TOF regions 0 to 58.2 ns, 58.2 ns to 116.4 ns and 116.4 ns to 174.6 ns. In order to overcome this problem, calculations were performed to determine where the TOF region of each particle would fall if this overlapping of TOF regions was taken into account. These calculations indicated a unique range for ^3He around the middle of the TOF spectrum.

Energy loss calculations were performed with the program ELOSS [80] for particles traversing Paddle 1 (Pad 1) and Paddle 2 (Pad 2). The various materials in the focal plane that the particles had to pass through before reaching the paddles are shown in Table 4.2. The actual thicknesses of the materials are shown in Column 2 of Table 4.2, while the effective thicknesses, for a particle traversing the focal plane at a trajectory angle of 35.75° , are shown in Column 3.

Particle	E range [MeV]	K range [u.MeV.C ⁻²]	TOF range [ns]	TOF range pulse sel. [ns]
³ He	211.9-248.2	159.7-187.1	67.6-72.5	29.4-34.3
p	158.6-185.7	same	48.5-51.5	10.3-13.3
d	79.3-92.9	same	87.9-94.6	49.7-56.4
t	52.9-62.0	same	129.1-139.4	32.7-42.9
⁴ He	159.7-187.0	same	87.4-94.1	49.2-55.8

TABLE 4.1: TOF and rigidity calculations for the ³He fieldset. Column 3 shows the calculated rigidity for the particle of interest. The TOF range in Column 4 corresponds to the minimum and maximum estimated TOFs which are based on the minimum and maximum energies in Column 2. Column 4 shows the realistic TOF of the particles, and Column 5 shows the TOF ranges which should be measured with the overlapping of TOF ranges taken into account.

Material	Thickness [mm]	Effective thickness [mm]
Kapton	0.075	0.128
Air	620	1054
Mylar	0.050	0.085
Ar-CO ₂ gas	48.0	81.6
Al	0.118	0.201
W	0.10	0.17
Paper	0.40	0.4
Paddle 1	3.175	3.175
Air	100	100
Paper	0.4	0.4
Al	0.058	0.058
Paddle 2	6.35	6.35

TABLE 4.2: A summary of the materials seen in the focal plane by the particles exiting the K600 vacuum chamber. For the sake of simplicity, all the layers of a specific material are listed once, even though there are three Al layers, for example, representing the three VDC HV planes. The second column lists the real material thickness, and the last column lists the effective thickness as seen by particles with an incident angle of 35.75°. From the Paper layer, the values in the last column were calculated for the setup where the paddles were placed at 90° with respect to the beam and at an angle with the VDC. Hence the real and effective thicknesses have the same values from the Paper layer to Paddle 2.

The light output of a scintillation counter is a measure of its efficiency in converting ionizing radiation into light energy. For any brand of scintillation counter, each particle with a unique charge and mass will have its own unique relative light output (RLO) for given incident and outgoing energies on a material. The relative light outputs of some commonly measured particles at the kind of energies that were measured in this experiment are shown in Fig. 4.13 [76].

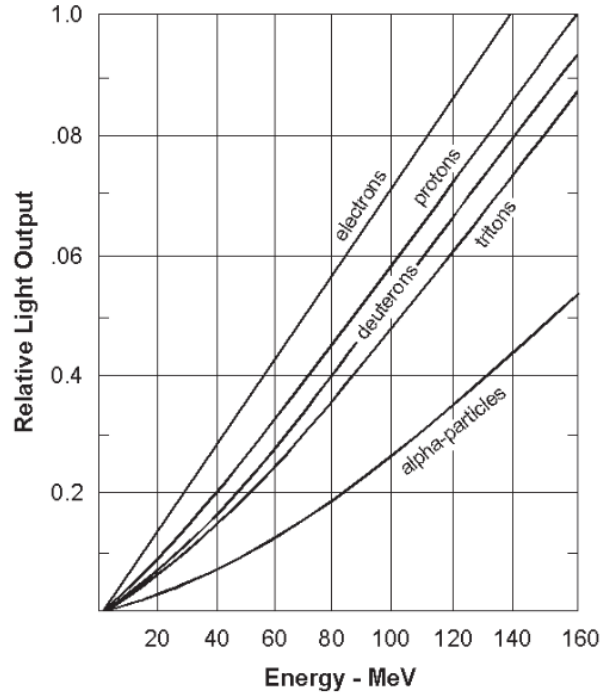


FIG. 4.13: The relative light outputs of electrons, protons, deuterons, tritons and α -particles at energies of up to 160 MeV. The RLO is approximately linear throughout this energy range for the electrons, and from around 80 MeV for the hydrogen isotopes. For the α -particles, as with other He isotopes, the RLO becomes nearly linear at energies beyond 160 MeV.

Since the scintillators measure light output and not energy, estimations were made for each of the relevant particles of the effect of the differing RLO values. The results of these estimates are shown in Table 4.3. A significant amount of energy was lost by the particles as they traversed the material in the focal plane upstream of the scintillation counters. Hence the energies of particles incident on Paddle 1 (E into Pad1), which are shown in Table 4.3, were smaller than the particle energies which reached the kapton exit window of the focal plane.

Particle	E into Pad1 [MeV]	Δ E _{Pad1} [MeV]	Δ E _{Pad2} [MeV]	Δ E _{Pad1} \times RLO [arb. units]	Δ E _{Pad2} \times RLO [arb. units]
^3He	202	13.2	29.2	0.79	4.88
p	161	1.7	3.43	0.02	0.09
d	75.5	5.07	11.2	0.2	0.9
t	42.5	12.5	28.3	0.84	2.83
^4He	140	23.2	71.4	1.7	17.49

TABLE 4.3: A summary of the calculated energy loss of various particles determined by the rigidity calculations of Table 4.1. Column 2 shows the expected particle energy incident on Paddle 1. Columns 3 and 4 show the calculated energy loss through both paddles, and Columns 5 and 6 show the corrected energy loss through the paddles with the effect of RLO taken into account.

The calculated spectra in Fig. 4.14 (a) - (d) illustrate the effect of taking the different RLOs into account on the predicted paddle spectra. The measured spectra in Fig. 4.14 (e) and (f) compare favourably with the predicted results in (a) - (d), especially in the case of Pad 1 vs TOF.

The calculated Paddle 1 vs Paddle 2 energy loss and light output corrected spectra are compared to the experimental Paddle 1 vs Paddle 2 spectrum in Fig. 4.15. The spectra in Fig. 4.16 represent plots of the focal plane position spectra, where the discrete states in ^{27}Al are clearly observed.

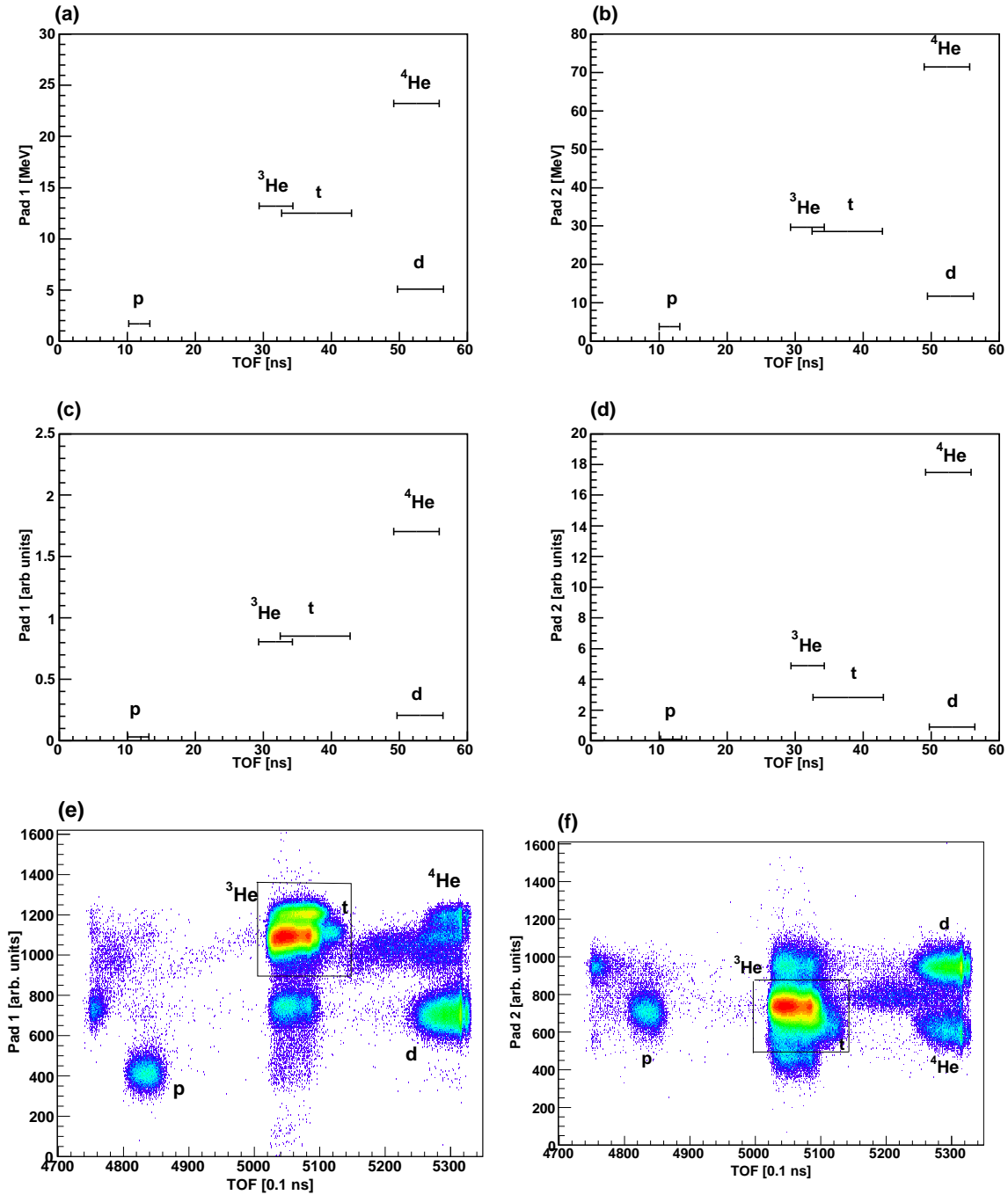


FIG. 4.14: Plots (a) and (b) are the calculated energy-loss vs TOF spectra for Paddle 1 and Paddle 2 respectively, while plots (c) and (d) are the light output corrected energy loss vs TOF spectra for Paddle 1 and Paddle 2 respectively. Note that an overlap in the TOF range could be expected in the cases of ^4He and d , since they are situated close to the edge of the TOF spectrum. The experimental energy loss vs TOF spectra are shown in (e) and (f). The black rectangles indicate the TOF and paddle gates for measuring the $^{27}\text{Al}(^3\text{He}, ^3\text{He})^{27}\text{Al}$ reaction. The TOF of p falls over a narrow range low in TOF, and the ^3He falls in the middle with the wider t -range. The d and ^4He particles are identified in the loci highest in TOF, and a bit of overlapping is seen for these particles.

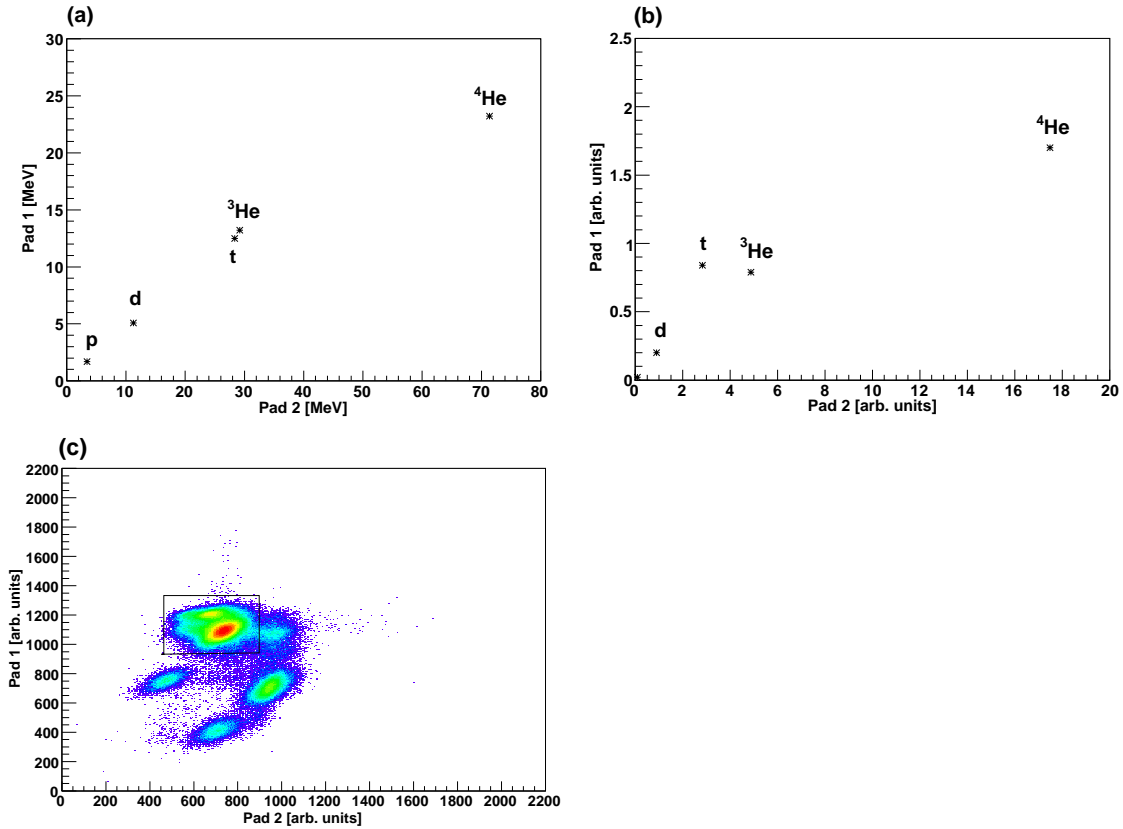


FIG. 4.15: The calculated Paddle 1 vs Paddle 2 spectra are shown in the first row, with the effect of different RLOs taken into account in (b), but not in (a). The measured spectrum is shown in (c). The black rectangle indicates the gate condition for measuring the $^{27}\text{Al}(^3\text{He}, ^3\text{He})^{27}\text{Al}$ reaction. It is noticeable that the ^3He particles appear much higher in Pad 1 than in Pad 2 in the experimental spectrum. This was not expected from the energy-loss calculations or the light-output estimates in Table 4.3. It was found that the light-output response from Paddle 2 was consistently weaker than the response from Paddle 1 during this experiment, although it was still correlated with energy loss.

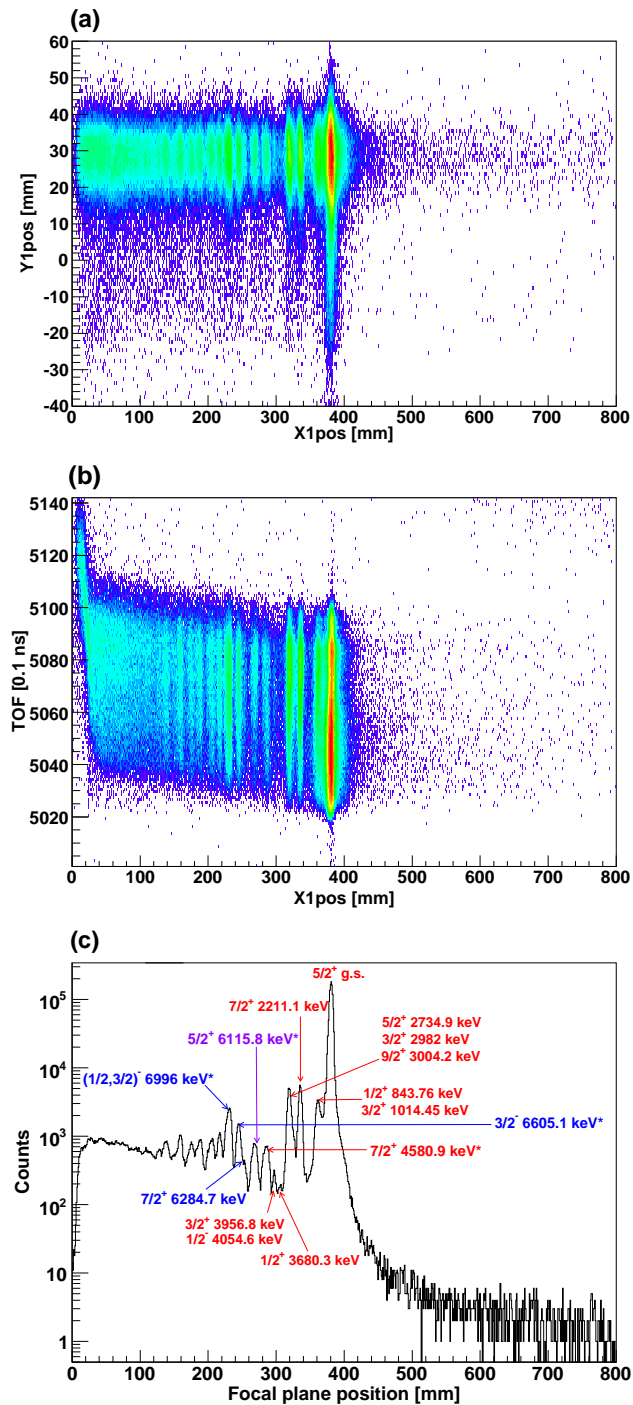


FIG. 4.16: Experimental focal plane position spectra obtained by applying the PID gates shown in Figs. 4.14 and 4.15. The plot of Y position vs X position is shown in (a), while the plot of TOF vs X position is shown in (b). Discrete states from the $^{27}\text{Al}(^3\text{He}, ^3\text{He})^{27}\text{Al}$ reaction are clearly visible in both spectra. The experimental ^{27}Al position spectrum with several states identified is shown in (c).

It was assumed that the position spectrum that is clearly visible in Fig. 4.16 is from the $^{27}\text{Al}(^3\text{He},^3\text{He})^{27}\text{Al}$ reaction, since K -value calculations predicted it to be the only reaction to have discrete structure with the appropriate magnetic field setting. The energy resolution was not optimised for this experiment since the intrinsic width of the excitation energy states to be observed were expected to be broad [35]. Therefore, the experimental resolution was not sufficient to separate some of the low lying energy states. A few assumptions had to be made about the identities of the peaks in the observed position spectrum. These assumptions, which are summarized in Table 4.4, were used to obtain the calibration curve in Fig. 4.17. A linear calibration between particle energy and focal plane position is adequate since the relationship between energy and position is approximately linear for the K600 spectrometer.

Experimental value [keV]	J^π	Position [mm]	Position w.r.t. ground state [mm]
0	$5/2^+$	380	0
843.76	$1/2^+$	361	19
1014.45	$3/2^+$		
2211.1	$7/2^+$	335	45
2734.9	$5/2^+$	319	61
2982.00	$3/2^+$		
3004.2	$9/2^+$		
3680.4	$1/2^+$	305	75
3956.8	$3/2^+$	297	83
4054.6	$1/2^-$		
4580.9*	$7/2^+$	286	94
5248.0*	$5/2^+$	268.5	111.5
5960.3*	$7/2$	253.5	126.5
6284.7	$7/2^+$	251	129
6605.1*	$3/2^-$	245	135
6996.0*	$(1/2,3/2)^-$	232	148

TABLE 4.4: The known experimental excitation energy values of the energy levels of ^{27}Al in the first column are matched to the positions of the discrete experimental peaks in the third and fourth columns. The * symbol indicates that the excited state shown in the table is not the only state that contributes to the observed peak. For the sake of simplicity, only the state that was used for the position-to-energy calibration is indicated for some of the higher excitation energy states.

The calibration of 47.8 keV/mm, which was obtained from Fig. 4.17, was used to plot the energy spectrum in Fig. 4.18. The double differential cross section of the $^{27}\text{Al}(^3\text{He},^3\text{He})^{27}\text{Al}$ reaction was calculated as a function of the energy of the ^3He particles using the following

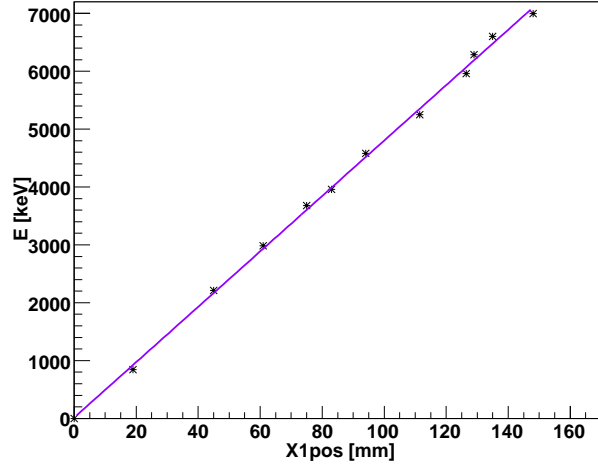


FIG. 4.17: This energy calibration curve was plotted from the observed ^{27}Al spectrum. The X position with respect to the ground state is plotted on the x-axis. An energy-to-position calibration of $47.8 \pm 6.35 \times 10^{-3}$ keV/mm was obtained.

equation:

$$\frac{d^2\sigma}{d\Omega dE} = \frac{N(\text{counts})}{I_f \cdot \rho \cdot D \cdot \varepsilon \cdot \Delta\Omega \cdot \Delta E} \times 10^{-27} \text{mb/sr} \quad (4.23)$$

where

- $N(\text{counts})$ is the number of events recorded per ΔE bin,
- I_f is the total incident flux,
- ρ is the number of target nuclei per unit area,
- D is the electronic dead time correction factor,
- ε is the VDC efficiency,
- $\Delta\Omega$ is the solid angle in sr,
- ΔE is the energy bin size in MeV.

The incident flux I_f was calculated with the following equation:

$$I_f = \frac{CII \cdot R}{2e}, \quad (4.24)$$

where

- CII is the current integrator scaler reading, which represents the number of digital pulses produced by the current integrator.

- The quantity R represents the selected range (in nA) of the current integrator.
- $2e$ is the electric charge of a Helium nucleus (in Coulomb). For hydrogen particles, this factor would be replaced by e , which represents a single proton charge.

The number of target nuclei per unit area ρ was calculated from

$$\rho = \frac{\lambda \cdot N_A}{A}, \quad (4.25)$$

where

- λ is the target thickness in $\text{mg}\cdot\text{cm}^{-2}$,
- N_A is the Avogadro number,
- A is the mass number of the target.

The result of this calculation, which was repeated for every reaction that could be identified during the experiment, is shown in Fig. 4.18. A peak cross section of $1.663 \text{ b}\cdot\text{sr}^{-1}\cdot\text{bin}^{-1}$ at the ground state of ^{27}Al , and an integrated ^{27}Al ground state cross section of $23.589 \text{ b}\cdot\text{sr}^{-1}$ were measured. A resolution of 279.5 keV was obtained for the $7/2^+$ 2211.1 keV state of ^{27}Al .

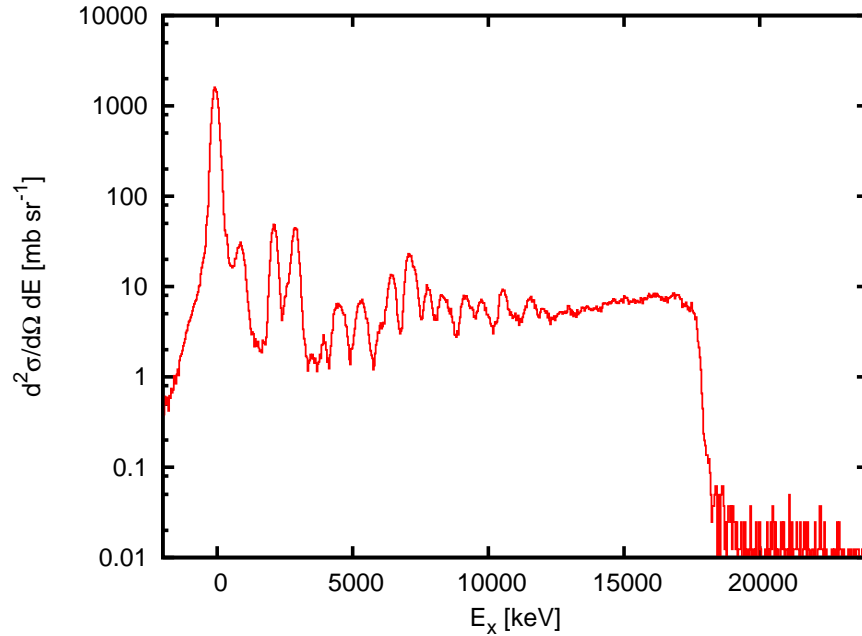


FIG. 4.18: The double differential cross section of the $^{27}\text{Al}(^3\text{He},^3\text{He})^{27}\text{Al}$ reaction. The energy bin size is 34 keV .

4.3.2 Analysis of the $^{27}\text{Al}(^3\text{He},d)^{28}\text{Si}$ fieldset

The $^{27}\text{Al}(^3\text{He},d)^{28}\text{Si}$ reaction has a Q-value of +6.091 MeV, hence the magnets were set to the 226 MeV d fieldset as shown in Table 3.1. Rigidity calculations showed that only the $^{27}\text{Al}(^3\text{He},^8\text{He})^{22}\text{Al}$ reaction could be expected to have a discrete structure, as can be seen from Table 4.5. The cross section for producing ^8He is expected to be very low. Therefore a clear visible locus on the PID spectrum could not be expected from five-neutron pick-up, considering that only 10 minutes of beam time was used for this measurement. The tritons comprised the only other locus that was expected to appear prominently in the PID spectra. The TOF calculations indicated a unique range for d about 20 ns below the expected range for t . The energy loss and light output results shown in Table 4.6 indicated that the deuterons should appear far lower in Pad 1 and Pad 2 than the tritons.

Particle	E range [MeV]	K range [u.MeV.C ⁻²]	TOF range [ns]	TOF range (pulse-sep) pulse sel. [ns]
d	207.7-242.6	418.3-488.5	57.4-61.3	19.4-23.1
t	138.7-161.9	same	81.9-88.0	43.7-49.8
^8He	209.1-244.2	same	107.5-115.7	69.3-77.5

TABLE 4.5: [

TOF and rigidity calculations for the 226 MeV d fieldset. The energy range is shown in Column 2, and the calculated rigidity for the particle of interest is shown in Column 3. Column 4 shows the calculated TOF, and Column 5 shows the TOF with the effect of overlapping taken into account.

Particle	E into Pad1 [MeV]	ΔEPad1 [MeV]	ΔEPad2 [MeV]	$\Delta\text{EPad1} \times \text{RLO}$ [arb. units]	$\Delta\text{EPad2} \times \text{RLO}$ [arb. units]
d	222	2.22	4.5	0.04	0.16
t	145	4.21	8.85	0.14	0.63
^8He	191.5	31.68	98.24	4.96	32.74

TABLE 4.6: A summary of the calculated energy loss of various particles determined by the rigidity calculations of Table 4.5. Column 2 shows the particle energy incident on Paddle 1, Columns 3 and 4 show the expected energy loss through both paddles, and Columns 5 and 6 show the expected energy loss through the paddles with the effect of RLO taken into account.

The experimental data measured with the d fieldset are shown on the left in Fig. 4.19. The data were obtained with the same paddle and trigger setup as the data for the ($^3\text{He},^3\text{He}$) reaction in Fig. 4.12. The expected PID spectra are shown on the right in Fig. 4.19. The experimental results correspond very well to what was predicted, especially in the case of Pad 1 vs TOF.

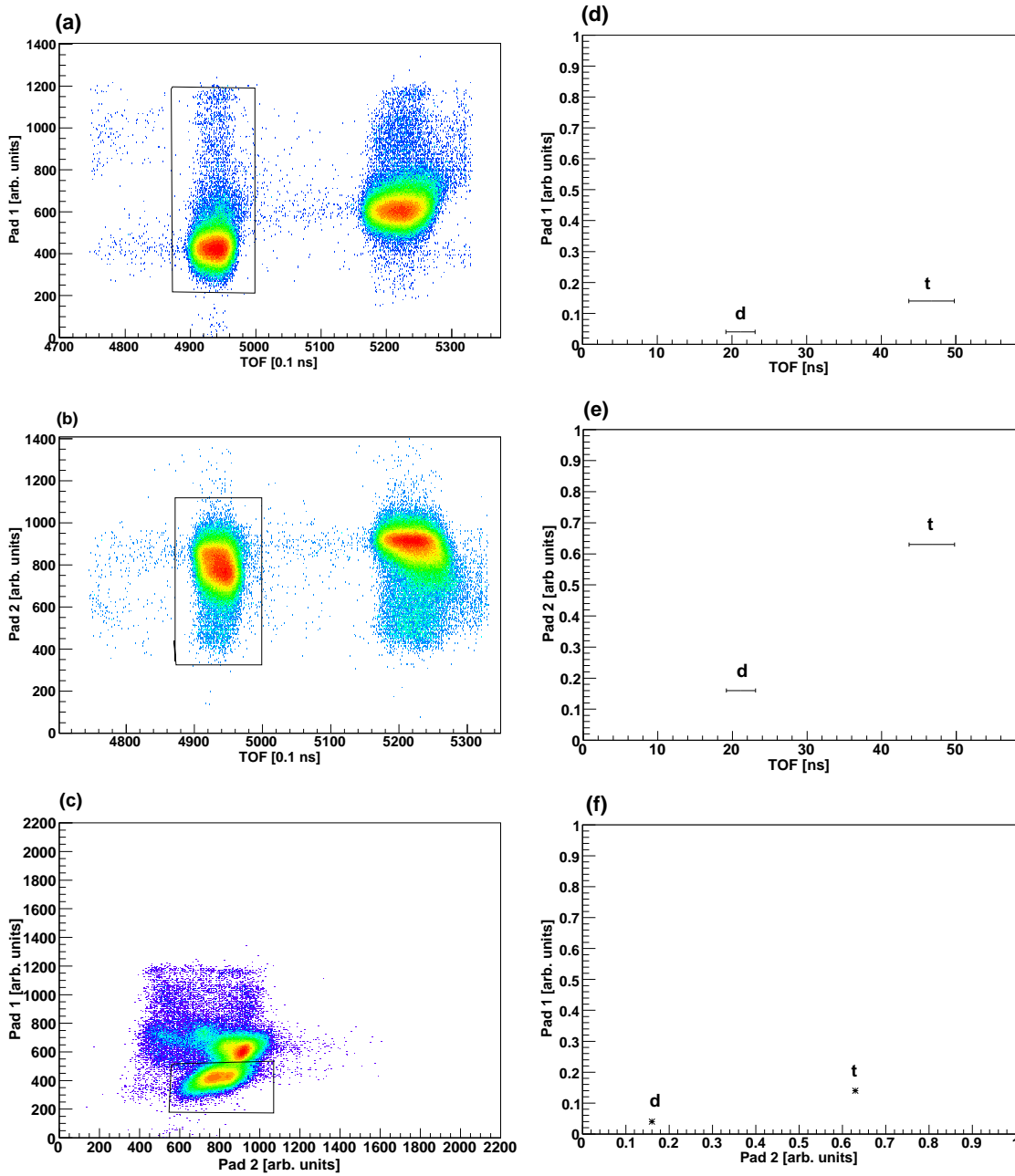


FIG. 4.19: Experimental PID spectra for the d fieldset with a paddle setup as described in section 4.3.1 are shown in (a) - (c) on the left. The expected PID spectra for the d fieldset are shown in (d) - (f) on the right. The deuteron range is easily distinguishable from the triton range in TOF since the two loci are well separated. The triton appears higher than the deuteron in both paddles. In Pad 2, the deuteron is proportionally higher with respect to the triton than what was expected. The PID gates used in the analysis are indicated by the rectangles in (a) - (c).

The X position spectrum as well as the TOF vs X position spectrum measured for deuterons is shown in Fig. 4.20. The discrete states are clearly visible in the two-dimensional spectrum. No structure is seen in a similar plot for the tritons. The data were obtained with TOF and paddle gates optimised for measuring the $^{27}\text{Al}(^3\text{He},d)^{28}\text{Si}$ reaction, as shown in Fig. 4.19. A beam current of $I_{beam}=11$ nA impinged on an 8.19 mg.cm^{-2} thick Al target for exactly 10 minutes. No veto paddle was used and a count rate of about 1 400 Hz was observed. Some of the higher excited states in the position spectrum appear to be stronger than the 0^+ ground state of ^{28}Si . This may be attributed to the fact that the cross section of the 0^+ state will have a maximum around $\theta_{lab} = 0^\circ$, while $\theta_{lab} = 8^\circ$ should be around its minimum.

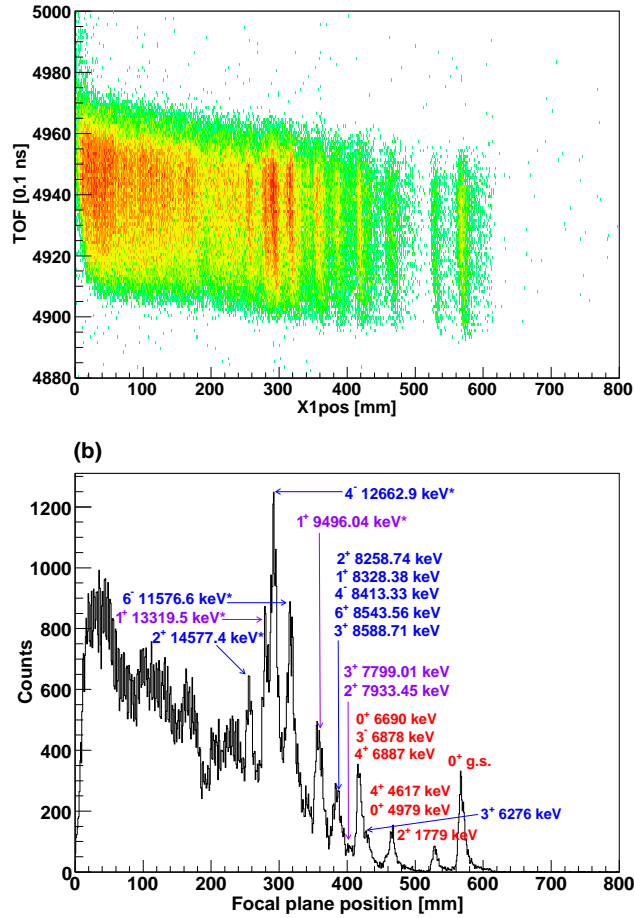


FIG. 4.20: Experimental focal plane position spectra for the d fieldset obtained by applying the PID gates shown in Fig. 4.19. TOF vs X position is shown in (a), and the X position spectrum with several states identified is shown in (b).

A few assumptions were made about the experimental peaks in Fig. 4.20, since the experimental resolution was not sufficient to separate several of the low excitation energy states. These assumptions, which are summarized in Table 4.7, were used to obtain the calibration curve in

Fig. 4.21. The calibration value of 45.6 keV/mm from Fig. 4.21 was used to obtain the energy spectrum in Fig. 4.22. This energy spectrum shows evidence of the giant dipole resonance of ^{28}Si between 15 and 24 MeV [81]. The result of the cross section calculation as a function of energy for these data is shown in Fig. 4.22. A peak cross section of $0.327 \text{ mb}\cdot\text{sr}^{-1}\cdot\text{bin}^{-1}$ was measured at the ground state, and $1.18 \text{ mb}\cdot\text{sr}^{-1}\cdot\text{bin}^{-1}$ was measured at the very tall and prominent peak, which was attributed to the 4^- 12 662.9 keV excited state. Integrated cross sections of $6.52 \text{ mb}\cdot\text{sr}^{-1}$ for the ground state, and $28.12 \text{ mb}\cdot\text{sr}^{-1}$ for the prominent peak were measured at $\theta_{lab} = 8^\circ$. A resolution of 488.2 keV was obtained for the the ground state of ^{28}Si .

Experimental value [keV]	J^π	Position [mm]	Position w.r.t. ground state [mm]
0	0^+	573	0
1779.03	2^+	533	40
4619.86	4^+	470	103
4979.92	0^+		
6276.2	3^+	430	143
6690.74	0^+	421	152
6878.79	3^-		
6887.65	4^+		
7799.01*	3^+	402	171
8258.74	2^+	389	184
8328.38	1^+		
8413.33	4^-		
8543.56	6^+		
8588.71	3^+		
9496.04*	1^+	362	211
11576.6*	6^-	319	254
12662.9*	4^-	295	278
13319.5*	1^+	281	292
14577.4*	2^+	255	318

TABLE 4.7: The known experimental excitation energy values of the energy levels of ^{28}Si in the first column are matched to the positions of the discrete experimental peaks in the third and fourth columns. The * symbol indicates that the excited state shown in the table is not the only state that contributes to the observed peak.

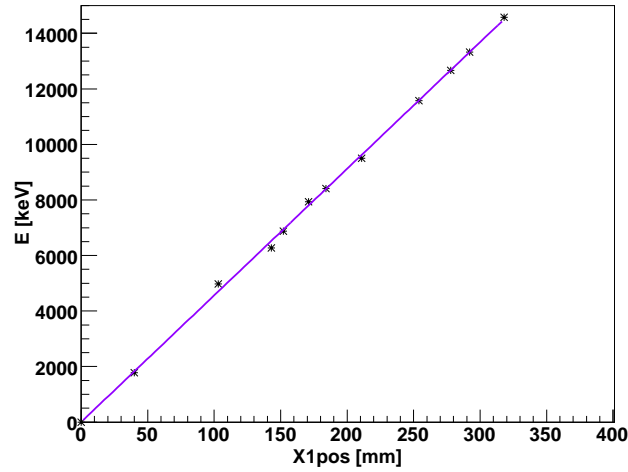


FIG. 4.21: This energy calibration curve was plotted from the observed ^{28}Si spectrum. The X position with respect to the ground state is plotted on the x-axis. An energy-to-position calibration of $45.6 \pm 3.04 \times 10^{-3}$ keV/mm was obtained.

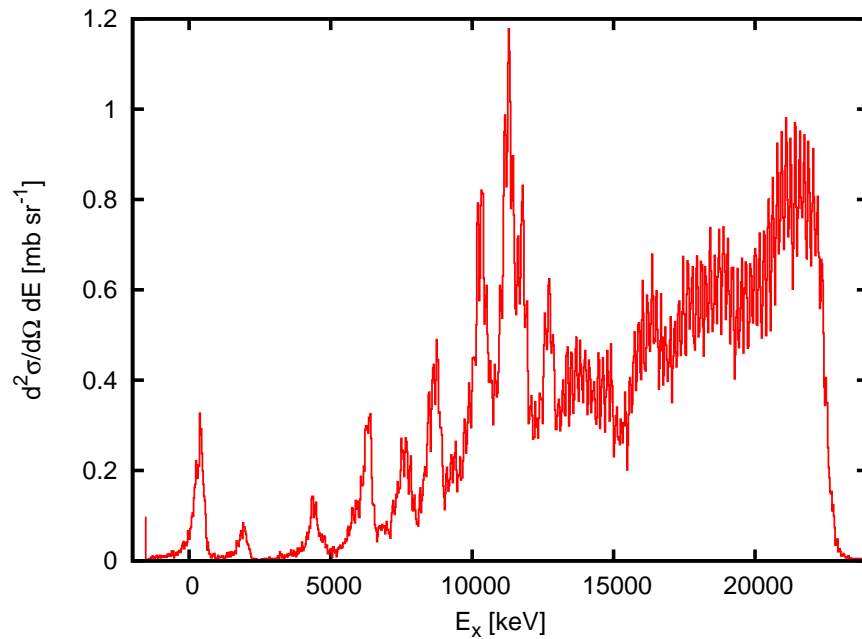


FIG. 4.22: The double differential cross section of the $^{27}\text{Al}(^3\text{He},d)^{28}\text{Si}$ reaction. The energy bin size is 26 keV.

4.3.3 Analysis of the $^{27}\text{Al}(^3\text{He},t)^{27}\text{Si}$ fieldset

The $(^3\text{He},t)$ reaction has a Q-value of -4.8 MeV, hence the magnets were set to the 215 MeV t fieldset as shown in Table 3.1. The $^3\text{He}^{1+}$ and $^4\text{He}^{1+}$ ions were found to be the best candidates for contamination of the t spectrum, but the probability is very low at energies of over 200 MeV for any electrons not to be stripped from the He nuclei while escaping the target. Table 4.8 indicates a TOF range around the middle of the spectrum for t , and Table 4.9 indicates a higher light output in Paddle 2 than in Paddle 1 for t .

Particle	E range [MeV]	K range [u.MeV.C ⁻²]	TOF range [ns]	TOF range (pulse-sep) pulse sel. [ns]
t	207.7-242.6	600-699.5	70.9-75.9	32.7-37.7
$^3\text{He}^{1+}$	199.0-232.1	same	70.9-75.9	32.7-37.7
$^4\text{He}^{1+}$	150.0-175.0	same	91.7-98.6	53.5-60.4

TABLE 4.8: TOF and rigidity calculations for the 215 MeV t fieldset. The energy range is shown in Column 2, and the calculated rigidity for the particle of interest is shown in Column 3. Column 4 shows the calculated TOF, and Column 5 shows the TOF with the effect of overlapping taken into account.

Particle	E into Pad1 [MeV]	ΔEPad1 [MeV]	ΔEPad2 [MeV]	$\Delta\text{EPad1} \times \text{RLO}$ [arb. units]	$\Delta\text{EPad2} \times \text{RLO}$ [arb. units]
t	211.0	3.15	6.41	0.08	0.33
$^3\text{He}^{1+}$	193.6	13.78	30.89	0.96	3.24
$^4\text{He}^{1+}$	134.2	24.35	88.89	2.62	26.67

TABLE 4.9: A summary of the calculated energy loss of various particles determined by the rigidity calculations of Table 4.8. Column 2 shows the particle energy incident on Paddle 1, Columns 3 and 4 show the expected energy loss through both paddles, and Columns 5 and 6 show the expected energy loss through the paddles with the effect of RLO taken into account.

The experimental PID spectra from the t field setting are shown on the left and compared to the expected PID spectra on the right in Fig. 4.23. The measurement was performed during the stage of the experiment when the paddles were parallel to the VDC, and events were triggered by a Paddle 1 and Paddle 2 coincidence. A single prominent locus is identified in all the experimental data. This locus is associated with the tritons.

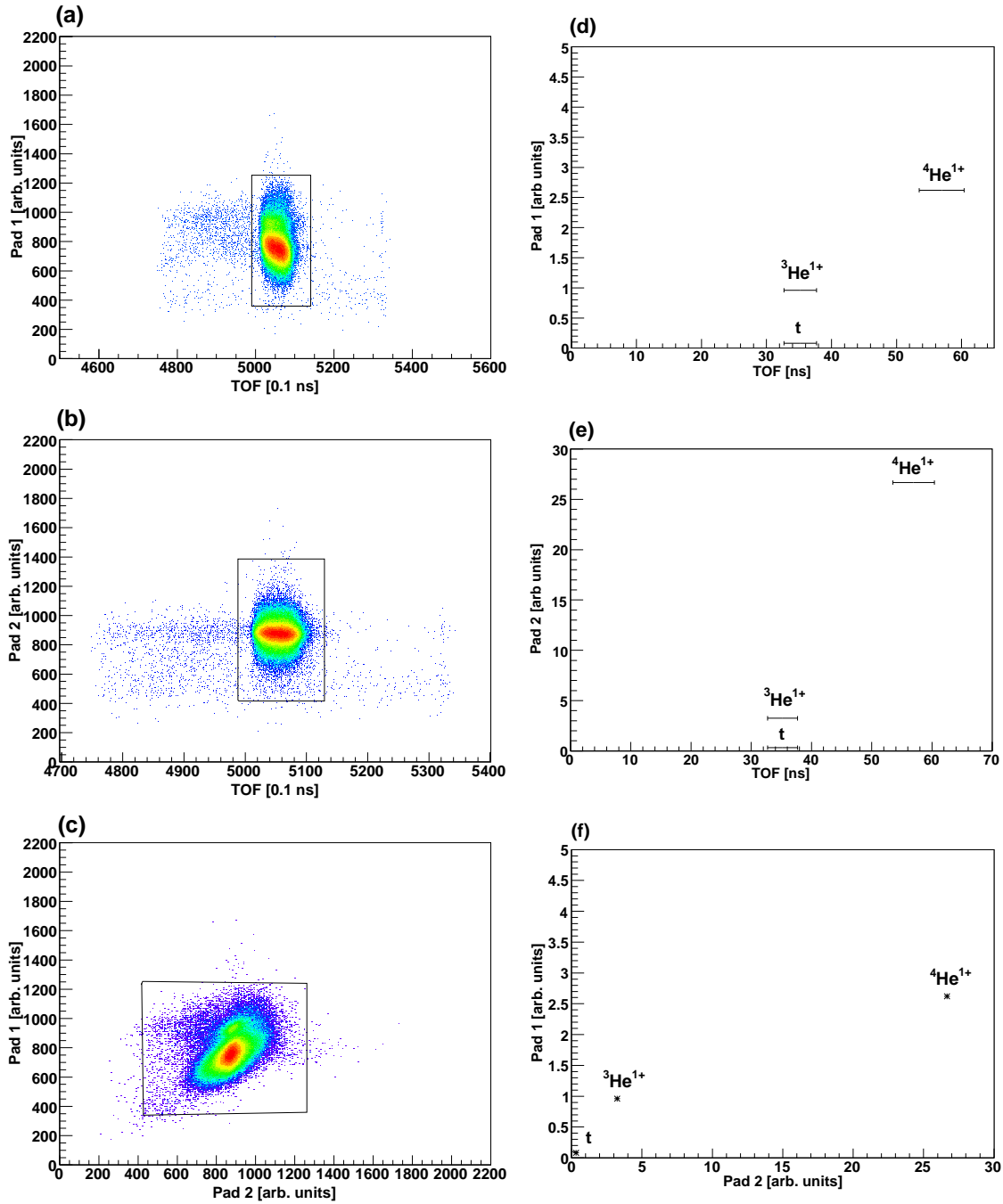


FIG. 4.23: Experimental PID spectra for the t fieldset with paddle setup as described in the text are shown in (a) - (c) on the left. Expected PID spectra are shown in (d) - (f) on the right. The single prominent locus can be expected to be t . The PID gates used in the analysis are indicated by the rectangles in (a) - (c).

The TOF vs X position and the X position spectrum measured with the t fieldset with TOF and paddle gates optimised for measuring the tritons are shown in Fig. 4.24. These data were obtained with a beam current of $I_{beam}=10$ nA impinging on a 4.43 mg.cm^{-2} Al target for a duration of 28 minutes. No paddle veto was used and an average count rate of about 400 Hz was observed. All the discrete states in TOF vs X position have the same shape, and therefore they must represent different states of the same reaction. The t was a very easy particle to identify since there was no contamination from other particles such as p , d , ${}^3\text{He}$ or ${}^4\text{He}$ in the PID spectrum. The ground state is much stronger than all the excited states, unlike the case of the ${}^{27}\text{Al}({}^3\text{He},d){}^{28}\text{Si}$ reaction. This is because the $5/2^+$ ground state is not situated at an angular minimum for cross section at $\theta_{lab} = 8^\circ$. The $({}^3\text{He},t)$ reaction is used extensively at RCNP in Osaka, Japan for Gamow-Teller studies [82]. It is known as a charge exchange reaction and in this case it populates ${}^{27}\text{Si}$, which is the mirror of ${}^{27}\text{Al}$.

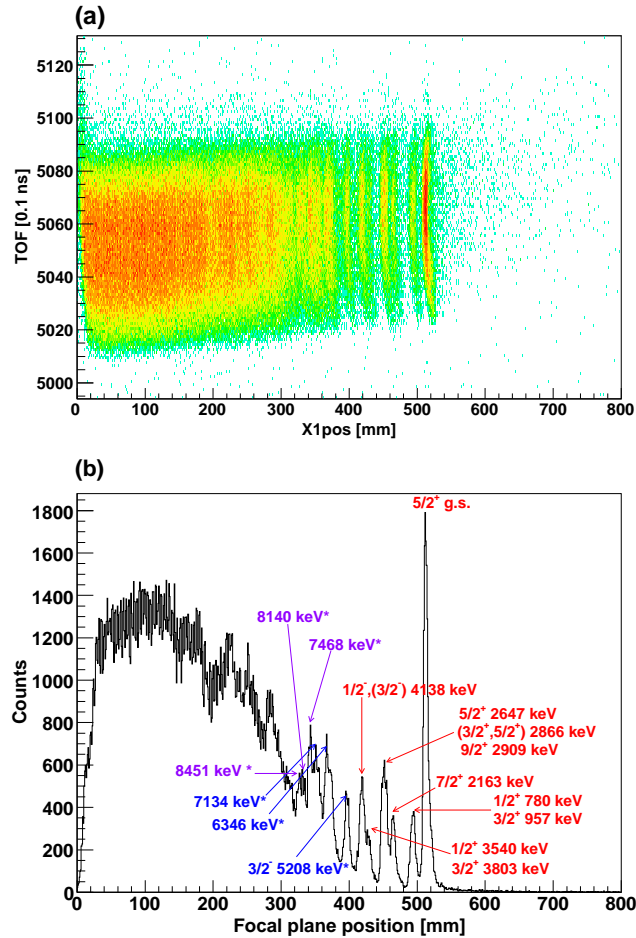


FIG. 4.24: The spectrum of TOF vs X position is shown in (a), and the experimental ${}^{27}\text{Si}$ position spectrum is shown in (b).

Some assumptions had to be made about the experimental peaks in Fig. 4.24, due to the insufficient energy resolution. These assumptions, which are summarized in Table 4.10, were used to obtain the calibration curve in Fig. 4.25. The energy-to-position calibration value which was obtained from Fig. 4.25 was used to obtain the energy spectrum of the $^{27}\text{Al}(^3\text{He},t)^{27}\text{Si}$ reaction in Fig. 4.26. The cross section for the $^{27}\text{Al}(^3\text{He},t)^{27}\text{Si}$ reaction was calculated as a function of energy. A peak cross section of $0.4453 \text{ mb}\cdot\text{sr}^{-1}\cdot\text{bin}^{-1}$ was measured at the ground state of ^{27}Si . An integrated cross section of $5.96 \text{ mb}\cdot\text{sr}^{-1}$ was found for the same state. The resolution of the ^{27}Si ground state was measured at 354.9 keV.

Experimental value [keV]	J^π	Position [mm]	Position w.r.t. ground state [mm]
0	$5/2^+$	513	0
780.9	$1/2^+$	495	18
957.4	$3/2^+$		
2163	$7/2^+$	466	47
2647.6	$5/2^+$	452	61
2866.3	$(3/2,5/2)^+$		
2909.9	$9/2^+$		
3540.2	$1/2^+$	428	85
3803.6	$3/2^+$		
4138.1	$1/2^-, (3/2^-)$	421	92
5208*	$3/2^-$	396	117
6346*		368.5	144.5
7134*		352	161
7468*		344.5	168.5
8140*		332	181
8451*	$(1/2,3/2)^+$	325	188

TABLE 4.10: The known experimental excitation energy values of the energy levels of ^{27}Si in the first column are matched to the positions of the discrete experimental peaks in the third and fourth columns. The * symbol indicates that the excited state shown in the table is not the only state that contributes to the observed peak.

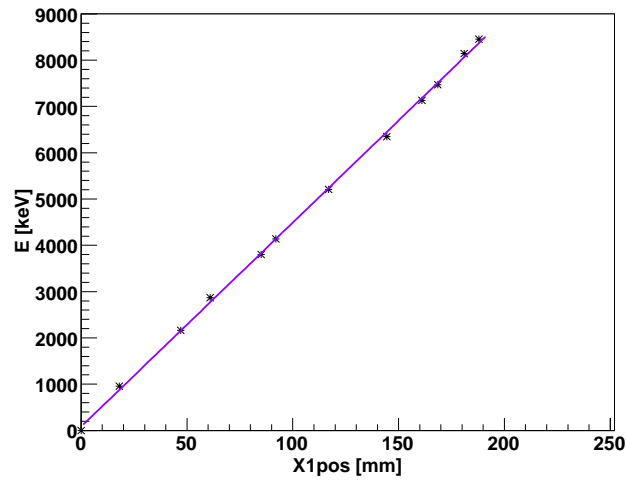


FIG. 4.25: This energy calibration curve was plotted from the observed ^{27}Si spectrum. The X position with respect to the ground state is plotted on the x-axis. An energy-to-position calibration of $44.1 \pm 4.66 \times 10^{-3}$ keV/mm was obtained. This calibration was used to plot the energy spectrum.

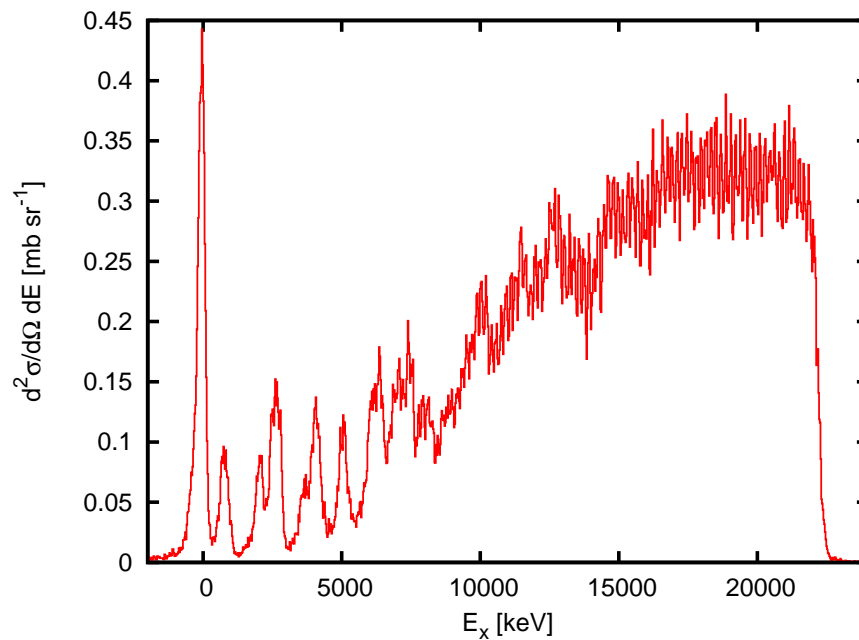


FIG. 4.26: The double differential cross section of the $^{27}\text{Al}(^3\text{He},t)^{27}\text{Si}$ reaction. The energy bin size is 26 keV.

4.3.4 Analysis of the $^{27}\text{Al}(^3\text{He},^4\text{He})^{26}\text{Al}$ fieldset

The $^{27}\text{Al}(^3\text{He},^4\text{He})^{26}\text{Al}$ one-neutron pick-up reaction has a Q-value of +7.52 MeV. The magnets were set to measure 236 MeV α particles. All three of the hydrogen isotopes (p , d and t) were expected to contaminate the ^4He -spectrum as indicated in Table 4.11. In the case of the protons, K -value calculations indicated that its energy range overlaps most of the ^4He kinetic energy range for particles with the same K -value. This means that discrete energy states for the $^{27}\text{Al}(^3\text{He},p)^{29}\text{Si}$ reaction could also be measured with the ^4He field setting. Table 4.11 indicates that the protons are well separated from the other particles in TOF. The ^4He and the deuterons fall together in TOF, but are well separated in energy loss as indicated in Table 4.12.

Particle	E range [MeV]	K range [u.MeV.C ⁻²]	TOF range [ns]	TOF range (pulse-sep) pulse sel. [ns]
^4He	208.1-244.1	271.0-244.1	77.3-83.2	39.1-45.0
p	206.5-242.4	same	44.0-46.6	5.76-8.38
d	103.3-121.2	same	77.8-83.7	39.6-45.5
t	69.0-80.9	same	113.5-122.6	17.1-26.2

TABLE 4.11: TOF and rigidity calculations for the 236 MeV α fieldset. The energy range is shown in Column 2, and the calculated rigidity for the particle of interest is shown in Column 3. Column 4 shows the calculated TOF, and Column 5 shows the TOF with the effect of overlapping taken into account.

Particle	E into Pad1 [MeV]	ΔEPad1 [MeV]	ΔEPad2 [MeV]	$\Delta\text{EPad1} \times \text{RLO}$ [arb. units]	$\Delta\text{EPad2} \times \text{RLO}$ [arb. units]
^4He	206.5	16.45	38.34	1.48	6.9
p	223	1.47	2.95	0.02	0.06
d	107.5	3.94	4.09	0.12	0.13
t	66	8.54	22.6	0.49	3.69

TABLE 4.12: A summary of the calculated energy loss of various particles determined by the rigidity calculations of Table 4.11. Column 2 shows the particle energy incident on Paddle 1, Columns 3 and 4 show the expected energy loss through both the paddles, and Columns 5 and 6 show the calculations for energy loss through the paddles with the effect of RLO taken into account.

Experimental data measured with the ^4He fieldset are shown in (a) - (c) on the left in Fig. 4.27, and expected PID spectra with the effect of RLO taken into account is shown in (d) - (f) on the right. The data were obtained with the same paddle and trigger setup as the ^3He and d data sets in Figs. 4.12 and 4.19, except that the Paddle 3 veto was not used. Several contaminants feature in the PID spectra of ^4He , unlike the case of t PID spectra. However, a one-to-one correlation can be drawn between the predictions for the four particles that were expected to have the highest cross sections (p , d , t and ^4He) on the right in Fig. 4.27 and the four most prominent loci measured on the left. PID selection gates were set around the loci which were expected to be ^4He and p particles using Pad 1 vs TOF. In the case of Pad 2 vs TOF in (b), the deuterons appear higher in Pad 2 than the ^4He particles, contrary to what was expected. Clearly the response of Paddle 2 is very different from the response of Paddle 1.

The TOF vs position spectra are shown in Fig. 4.28 and compared to the position spectra measured with PID selection gates to select the $^{27}\text{Al}(^3\text{He},^4\text{He})^{26}\text{Al}$ and $^{27}\text{Al}(^3\text{He},p)^{29}\text{Si}$ reactions. These data were measured with a beam current of $I_{beam} = 9$ nA impinging on a 4.43 mg.cm $^{-2}$ target for a duration of 37 minutes. Paddle 1 and Paddle 2 were used as trigger detectors and the veto detector was not used. A count rate of 1.74 kHz was obtained. Good statistics were obtained for the ^{26}Al spectrum, but not for the ^{29}Si spectrum. This can be explained by the fact that one-neutron pick-up has a higher cross section than deuteron stripping with a ^3He beam. In the $(^3\text{He},p)$ reaction, a deuteron is effectively stripped from the beam particle and donated to the target nucleus. Hence the ^{29}Si position spectrum does not contain enough statistics to enable for the identification of specific states, but there is some evidence of a discrete structure. Add to that the already compelling arguments which can be made from the predicted TOF range and paddle energy loss of the protons, and this locus can with certainty be assigned to the $^{27}\text{Al}(^3\text{He},p)^{29}\text{Si}$ reaction.

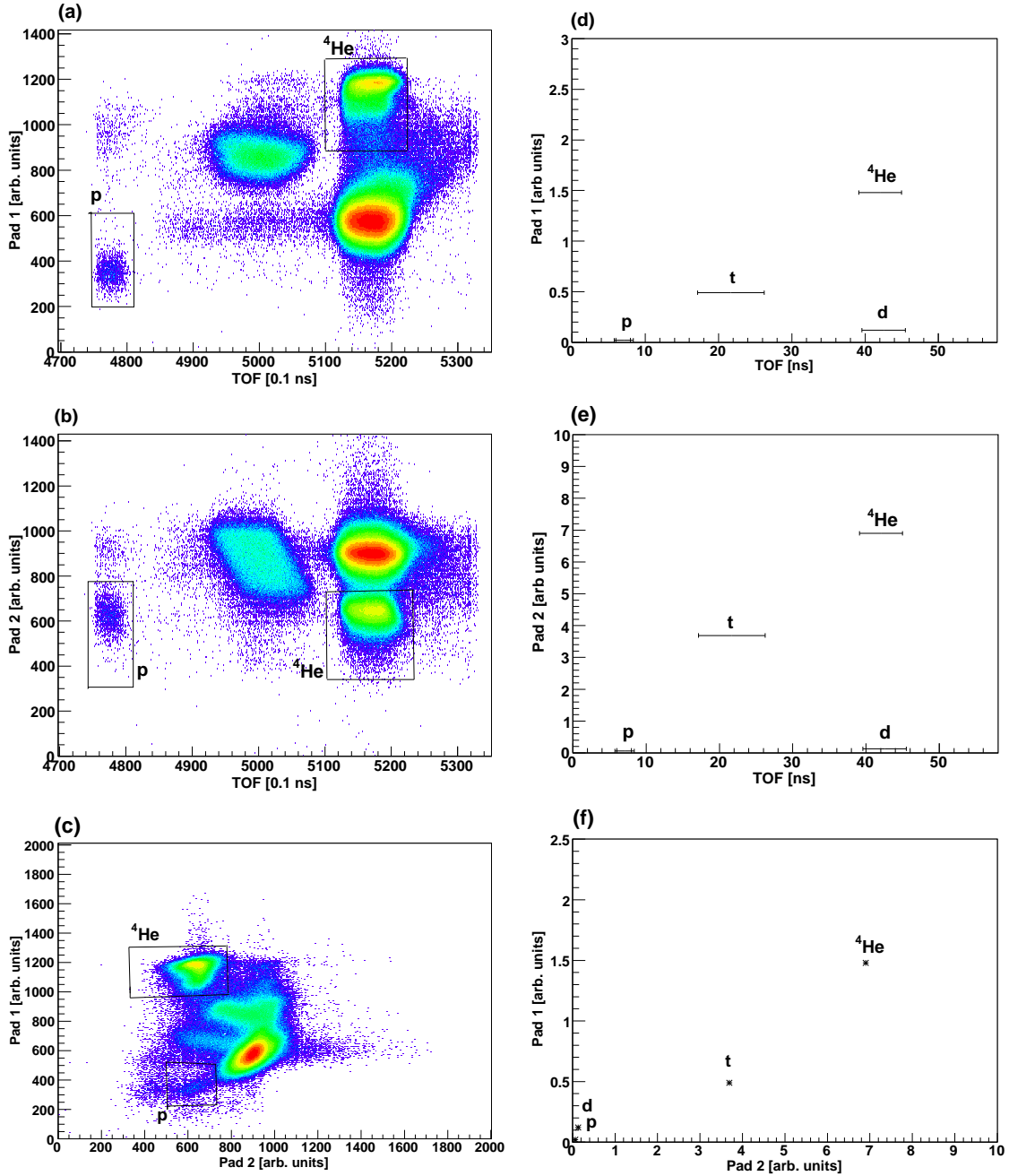


FIG. 4.27: Experimental PID spectra for the ^4He fieldset with paddle setup as described in section 4.3.1, but with the Paddle 3 veto not used. The experimental PID spectra are shown in (a) - (c) on the left, and the expected PID spectra are shown in (d) - (f) on the right. In each case, the four loci, for p , d , t and ^4He , may be separated and identified in both TOF and paddle energy. The PID gates used in the analysis are indicated by the rectangles in (a) - (c).

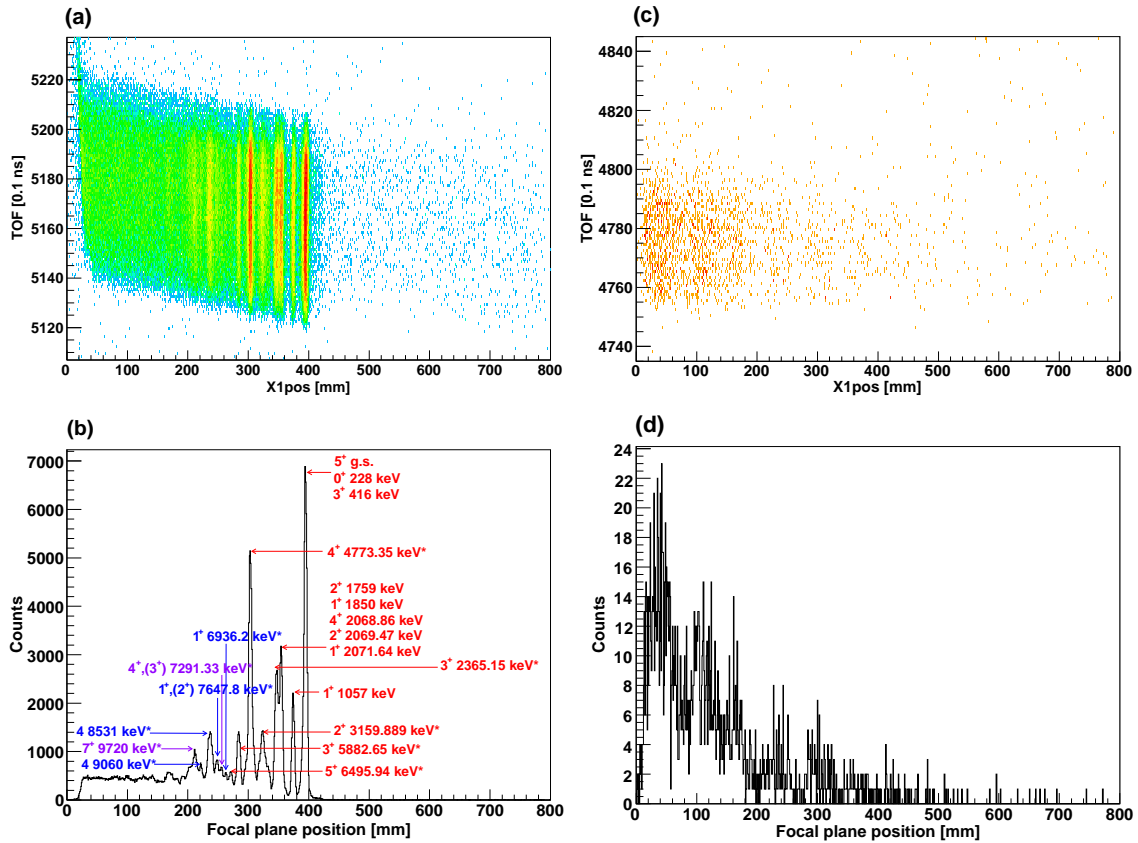


FIG. 4.28: The TOF vs X position and X position spectra are shown for the $^{27}\text{Al}(^3\text{He},^4\text{He})^{26}\text{Al}$ reaction in (a) and (b), and for the $^{27}\text{Al}(^3\text{He},p)^{29}\text{Si}$ reaction in (c) and (d). Discrete structure is evident for both reactions, although much better statistics were obtained for the ($^3\text{He},^4\text{He}$) reaction.

An energy-to-position calibration was performed for the measured spectrum of the $^{27}\text{Al}(^3\text{He},^4\text{He})^{26}\text{Al}$ one-neutron pick-up reaction. The same method was used as in the previous calibrations where assumptions were made concerning the experimental peaks in Fig. 4.28. These assumptions, which are summarized in Table 4.13, were used to obtain the calibration curve in Fig. 4.29. The energy-to-position calibration value which was obtained from Fig. 4.29 was used to plot energy spectra for both the $^{27}\text{Al}(^3\text{He},^4\text{He})^{26}\text{Al}$ and the $^{27}\text{Al}(^3\text{He},p)^{29}\text{Si}$ reactions in Figs. 4.30 and 4.31. The results of the cross section calculations which were performed for these energy spectra are shown in Figs. 4.30 and 4.31. A peak cross section of $5.23 \text{ mb}\cdot\text{sr}^{-1}\cdot\text{bin}^{-1}$ was measured at the ground state of ^{26}Al , while $1.78 \text{ mb}\cdot\text{sr}^{-1}\cdot\text{bin}^{-1}$ was measured at the top of the 1^+ 1057 keV excited state of ^{26}Al . An integrated cross section of $24.95 \text{ mb}\cdot\text{sr}^{-1}$ was measured at the 1057 keV state. A resolution of 233.61 keV was obtained at the 1057 keV state of ^{26}Al . A total integrated cross section of $3.78 \text{ mb}\cdot\text{sr}^{-1}$ was found for the entire measured ^{29}Si spectrum.

Experimental value [keV]	J^π	Position [mm]	Position w.r.t. ground state [mm]
0	5^+	394	0
228	0^+		
416	3^+		
1057	1^+	374	20
1759	2^+	356	38
1850	1^+		
2068.86	4^+		
2069.47	2^+		
2071.64	1^+		
2365.15*	3^+	348	46
3159.889*	2^+	324	70
4773.35*	4^+	302	92
5882.65*	3^+	283	111
6495.94*	5^+	271	123
6936.2*	1^+	263	131
7291.33*	$4^+, (3^+)$	256	138
7647.8*	$1^+, (2^+)$	249	145
8531*	4	235	157
9060*	4	222	170
9720*	7^+	211	181

TABLE 4.13: The known experimental excitation energy values of the energy levels of ^{26}Al in the first column are matched to the positions of the discrete experimental peaks in the third and fourth columns. The * symbol indicates that the excited state shown in the table is not the only state that contributes to the observed peak.

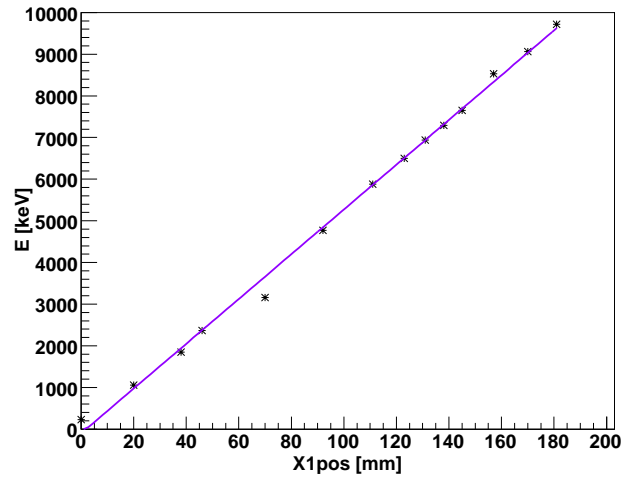


FIG. 4.29: This energy calibration curve was plotted from the observed ^{26}Al spectrum. The X position with respect to the ground state is plotted on the x-axis. An energy-to-position calibration of $53.7 \pm 4.77 \times 10^{-3}$ keV/mm was obtained.

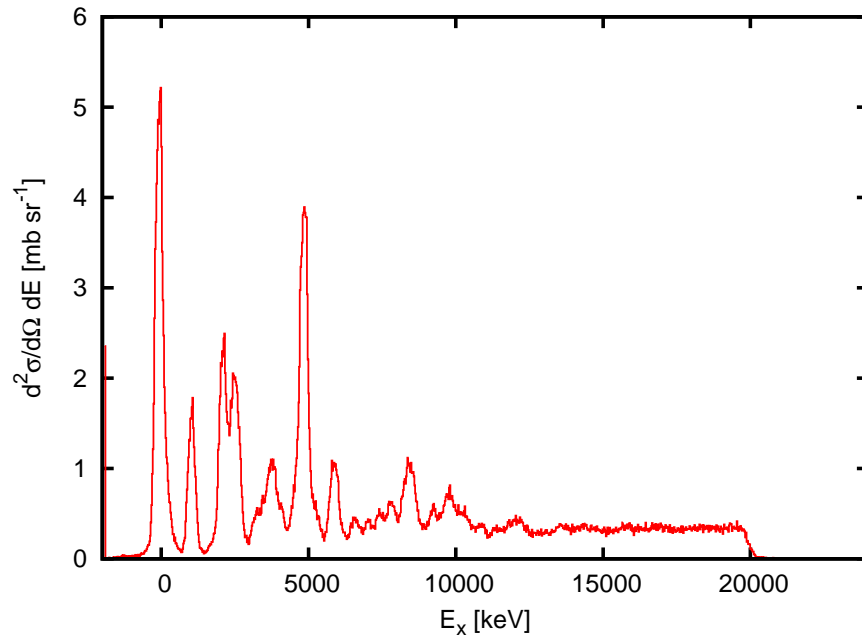


FIG. 4.30: The double differential cross section of the $^{27}\text{Al}(^3\text{He}, ^4\text{He})^{26}\text{Al}$ reaction. The energy bin size is 24 keV.

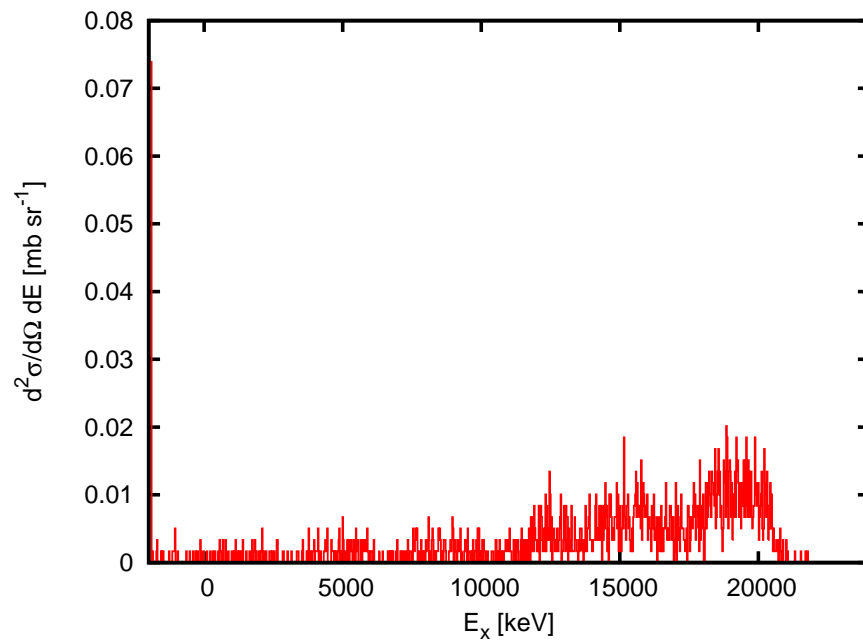


FIG. 4.31: The double differential cross section of measuring the $^{27}\text{Al}(^3\text{He},p)^{29}\text{Si}$ reaction. The energy bin size is 24 keV.

4.3.5 Analysis of the $^{27}\text{Al}(^3\text{He}, ^6\text{He})^{24}\text{Al}$ fieldset

The $^{27}\text{Al}(^3\text{He}, ^6\text{He})^{24}\text{Al}$ three-neutron pick-up reaction has a Q-value of -19.8 MeV, hence the magnets in Table 3.1 were set to measure 196 MeV ^6He particles. Table 4.14 indicates a unique energy range for ^6He . It also indicates that t and $^3\text{He}^{1+}$ will fall in a very similar TOF range to that of ^6He , while d and ^8He will not. With a ^3He beam, the probability of having an outgoing $^3\text{He}^{1+}$ ion is not negligible compared to that of obtaining a three-neutron pick-up reaction with $^6\text{He}^{2+}$ as the outgoing particle. Table 4.15 indicates a significant difference in the relative light outputs of ^6He and $^3\text{He}^{1+}$.

Particle	E range [MeV]	K range [u.MeV.C ⁻²]	TOF range [ns]	TOF range (pulse-sep) pulse sel. [ns]
^6He	183.9-216.3	275.9-324.4	98.7-106.6	60.5-68.4
d	137.0-161.1	same	68.5-73.6	30.3-35.4
t	91.5-107.6	same	99.2-107.1	61.0-68.9
^8He	137.9-162.2	same	130.0-140.6	53.6-64.6
$^3\text{He}^{1+}$	91.5-107.6	same	99.0-107.1	60.8-68.7

TABLE 4.14: TOF and rigidity calculations for the 196 MeV ^6He fieldset. The energy range is shown in Column 2, and the calculated rigidity for the particle of interest is shown in Column 3. Column 4 shows the calculated TOF, and Column 5 shows the TOF with the effect of overlapping taken into account.

Particle	E into Pad1 [MeV]	ΔEPad1 [MeV]	ΔEPad2 [MeV]	$\Delta\text{EPad1} \times \text{RLO}$ [arb. units]	$\Delta\text{EPad2} \times \text{RLO}$ [arb. units]
^6He	165	28.51	52.75	3.8	10.55
d	146	3.07	6.29	0.08	0.32
t	90.5	5.91	12.84	0.28	0.98
^8He	99	76.31	22.69	7.63	0.0267
$^3\text{He}^{1+}$	64	48.66	15.34	3.41	0.0133

TABLE 4.15: A summary of the calculated energy loss of various particles determined by the rigidity calculations of Table 4.14. Column 2 shows the particle energy incident on Paddle 1, Columns 3 and 4 show the expected energy loss through both paddles, and Columns 5 and 6 show the expected energy loss through the paddles with the effect of RLO taken into account.

4.3.5.1 Paddles perpendicular to the beam

Experimental data measured with the 196 MeV ${}^6\text{He}$ fieldset are shown in Fig. 4.32. These data were obtained with the same paddle and trigger setup as the data in Figs. 4.12, 4.19 and 4.27 from sections 4.3.1, 4.3.2 and 4.3.4. Paddle 1 and Paddle 2 were used as trigger detectors and Paddle 3 as a veto detector. A beam current of $I_{beam} = 11$ nA impinged on an 8.19 mg.cm^{-2} Al target for a duration of 34 minutes, and a count rate of 430 Hz was obtained.

The ${}^6\text{He}$ particles appear very close to ${}^3\text{He}^{1+}$ in Pad 1 in the predictions with RLO taken into account in Fig. 4.32 (d) - (f). This means that they may be very difficult to separate.

The predictions in Fig. 4.32 (d) and (e) indicate that ${}^6\text{He}$ will have a TOF range which is very similar to that of t and ${}^3\text{He}^{1+}$, and that it might be difficult to separate from these particles. The TOF range indicated in (a) and (b) of Fig. 4.32 is investigated in Fig. 4.33. The position spectrum corresponding to all events that fall within this TOF range is shown in Fig. 4.33 ii). A very prominent peak appears very close to the margin on the low energy side of this position spectrum. This same peak appears in the position spectrum that contains an additional gate in Paddle 1 for eliminating vi), which was expected to contain the tritons, in Fig. 4.33 iii). It also appears in the PID selected region where the ${}^3\text{He}^{1+}$ was expected to fall in Fig. 4.33 iv), but not as strongly as it does in the region where the ${}^6\text{He}$ particles could be expected in v). The background is much reduced in v) from what it is in iii). It was thought that this peak might be from the ${}^{27}\text{Al}({}^3\text{He}, {}^6\text{He}){}^{24}\text{Al}$ reaction, and that the rest of the discrete spectrum was lost because of the energy range that arose from the choice of field settings (optimised for 196 MeV ${}^6\text{He}$ particles). The spectrum in Fig. 4.33 vi) shows the position spectrum obtained with PID selection gates for seeing the tritons. No discrete structure is evident in this spectrum.

The events outside of the TOF range that was investigated in Fig. 4.33 are investigated in Fig. 4.34. A peak is seen at the same position, near the low energy margin, in ii), iv), v) and vi) of Fig. 4.34 as the one that was seen in Fig. 4.33. This suggests that the peak may arise from an edge effect of the VDC.

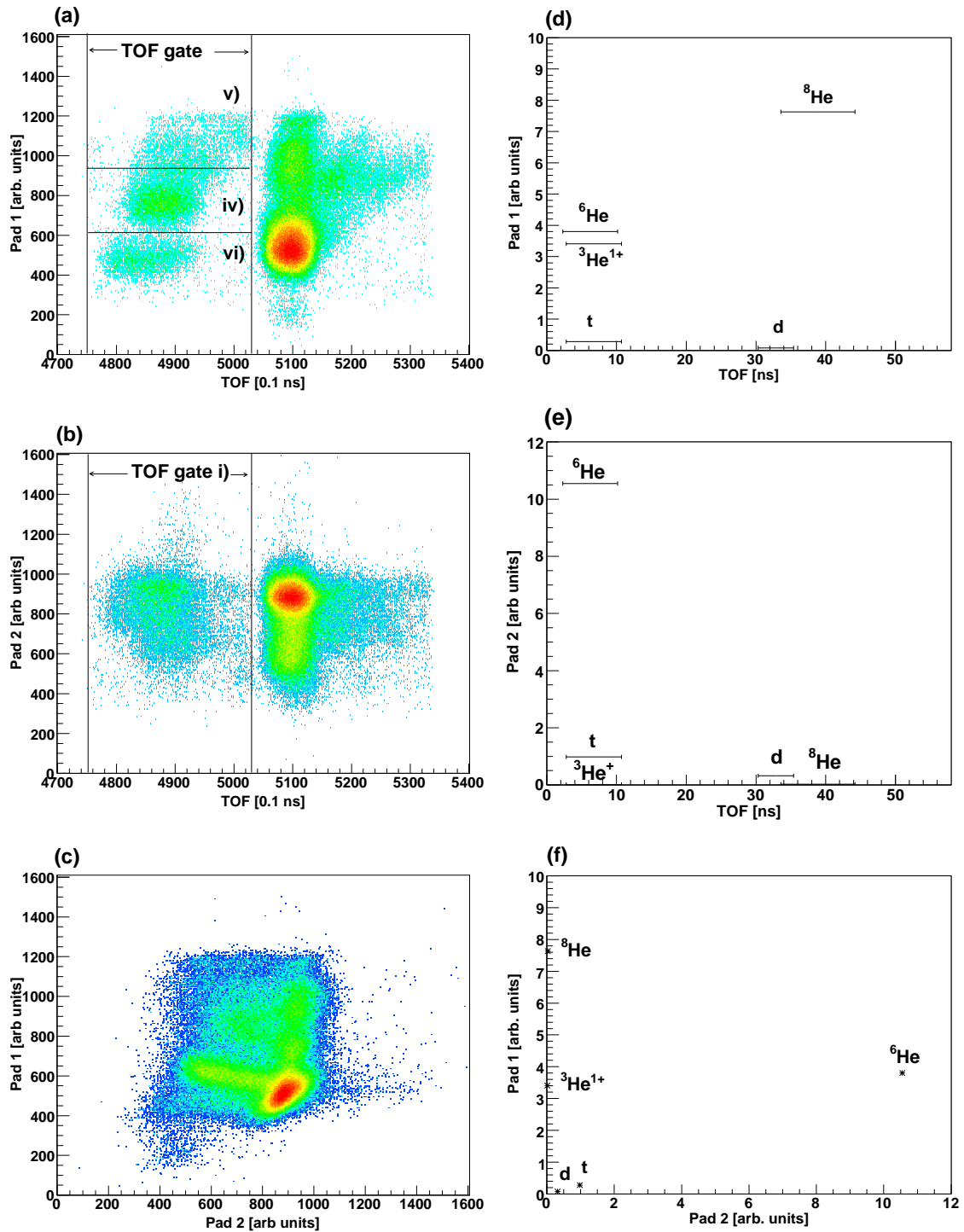


FIG. 4.32: Experimental PID spectra for the 196 MeV ${}^6\text{He}$ fieldset with a paddle setup as described in section 4.3.1 are shown in (a) - (c) on the left. The expected PID spectra for the ${}^6\text{He}$ fieldset are shown in (d) - (f) on the right.

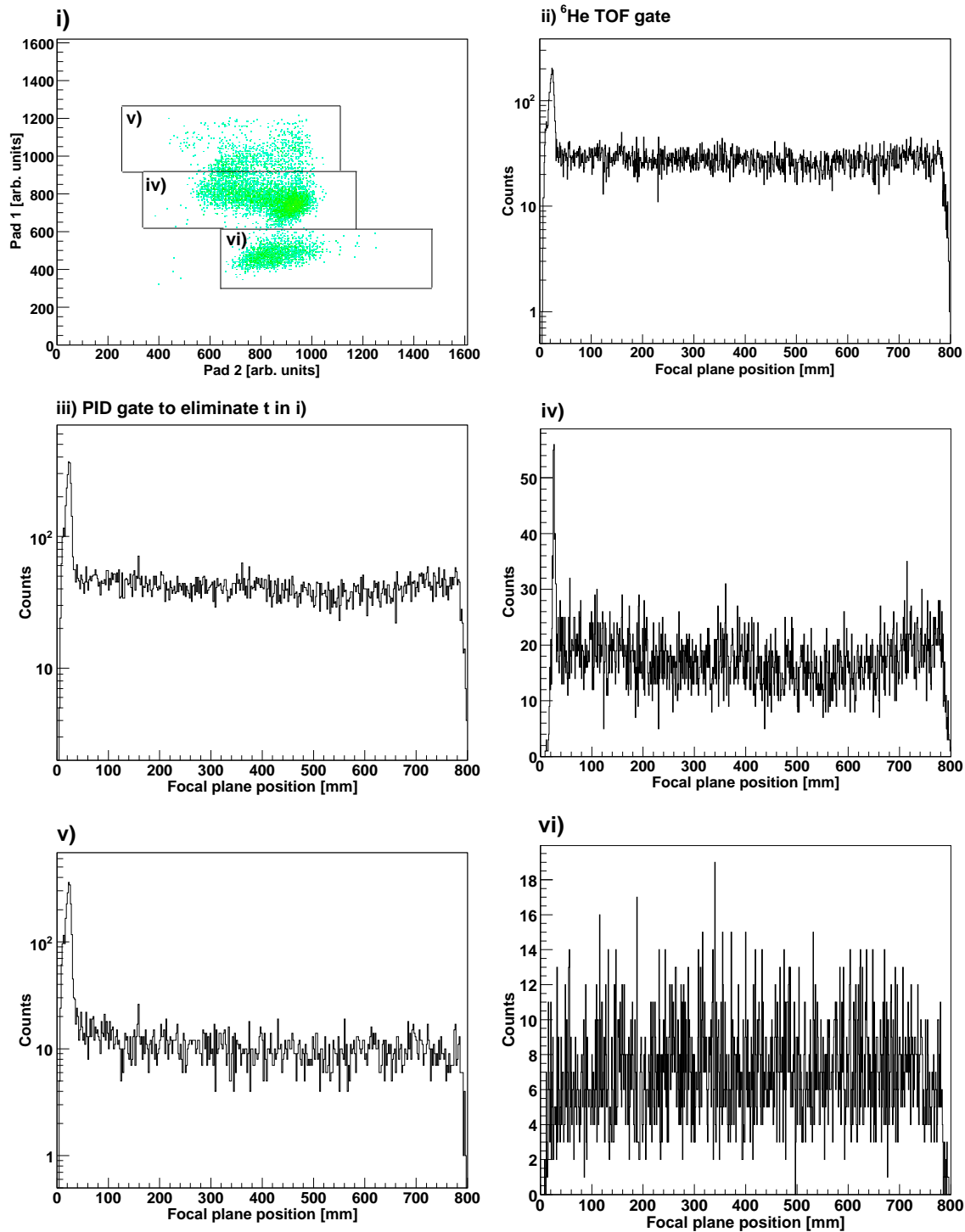


FIG. 4.33: The experimental Paddle 1 vs Paddle 2 spectrum for events that fall within the TOF gate in Fig. 4.32 is shown in i). The position spectrum corresponding to this TOF gate is shown in ii), while the position spectrum in iii) corresponds to an additional paddle gate to eliminate tritons (area vi)). The position spectra corresponding to the PID selection gates indicated in i) are shown in iv) - vi).

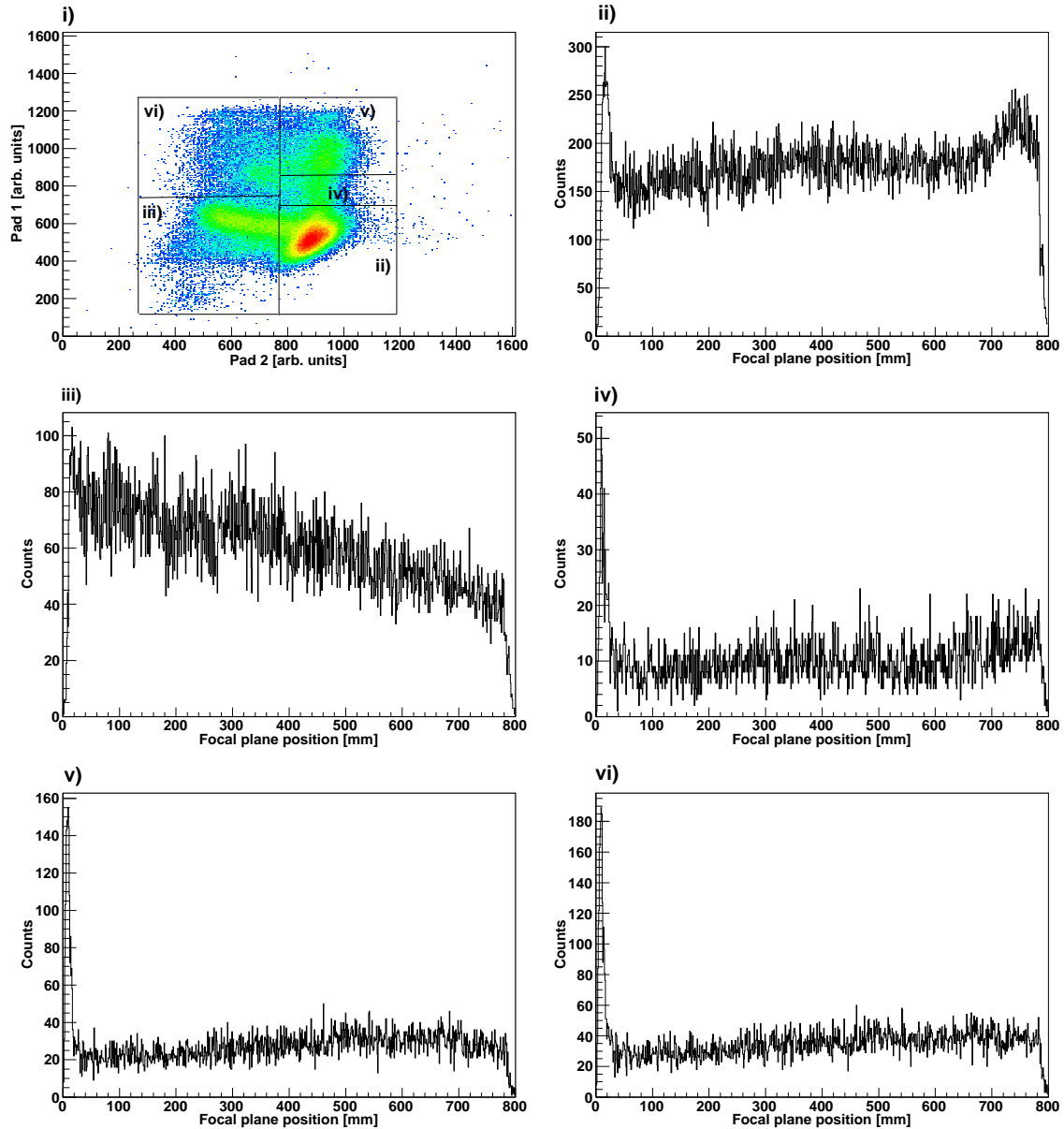


FIG. 4.34: The experimental Paddle 1 vs Paddle 2 spectrum for events that do not fall within the TOF gate in Fig. 4.32 is shown in i). The position spectra corresponding to the PID selection gates indicated in i) are shown in ii) - vi).

4.3.5.2 Paddles parallel to the VDC

As mentioned in the experimental procedure, a measurement was also taken for the $^{27}\text{Al}(^3\text{He},^6\text{He})^{24}\text{Al}$ reaction with the paddles parallel to the VDC and only Paddle 1 and Paddle 2 used as trigger detectors. A beam current of about 10 nA impinged on a 4.43 mg.cm^{-2} Al target for a duration of 54 minutes. Data obtained from this measurement are shown in Fig. 4.35. A slightly different field setting, namely the 202 MeV ^6He fieldset in Table 3.1, was used in order to look at a different energy range. This was done to test whether the peak from the position spectra in Fig. 4.33 was from the $^{27}\text{Al}(^3\text{He},^6\text{He})^{24}\text{Al}$ reaction. Moving the paddles to be parallel with the VDC causes them to be at an angle with the incident particles, thus increasing the effective thickness of material that the particles must pass through. It was hoped that some of the lower energy particles would no longer reach Paddle 2, thus enabling for more clear observation of some of the higher energy particles i.e. the ^6He in this case. It is difficult to conclude from the data in Fig. 4.35 whether there were any specific particles that no longer reached Paddle 2. The same loci seemed still to be present. The ^6He particles could again be expected to be found in the lower TOF range as indicated in Fig. 4.35. A position spectrum from this TOF range is shown in Fig. 4.36 ii). This spectrum is flat, with no definite peak on the low energy side or anywhere else.

The position spectra with PID gates for

1. viewing events that fall within the TOF range for ^6He excluding the lowest locus in Pad 1, which is probably t , is shown in Fig. 4.36 iii),
2. viewing events that correspond to the upper (in Pad 1) of the two remaining candidates for ^6He is shown in Fig. 4.36 iv),
3. and for events that correspond to the lower of the two candidates is shown in Fig. 4.36 v).

The position spectrum in iii) has a trough in the middle and two wide “hills” at around 0 - 200 mm and 500 - 800 mm, but no clear evidence of a discrete structure. The prominent peak from the spectra in Fig. 4.33 is not clearly seen in any of these spectra, but might well be related to the hill at 0 - 200 mm in iii). The field settings were changed to detect ^6He with a higher energy (+ 6 MeV) to ensure that the discrete states are not out of range, and still no discrete structure appears in the focal plane, as can be seen from the data shown in Figs. 4.35 and 4.36. Hence it was concluded that the peak near the low energy margin of the focal plane in Fig. 4.33 is probably just an edge effect of the VDC. The position spectrum in iv) is mostly continuous with no evidence of a discrete structure. The spectrum in v) also seems to contain the peak

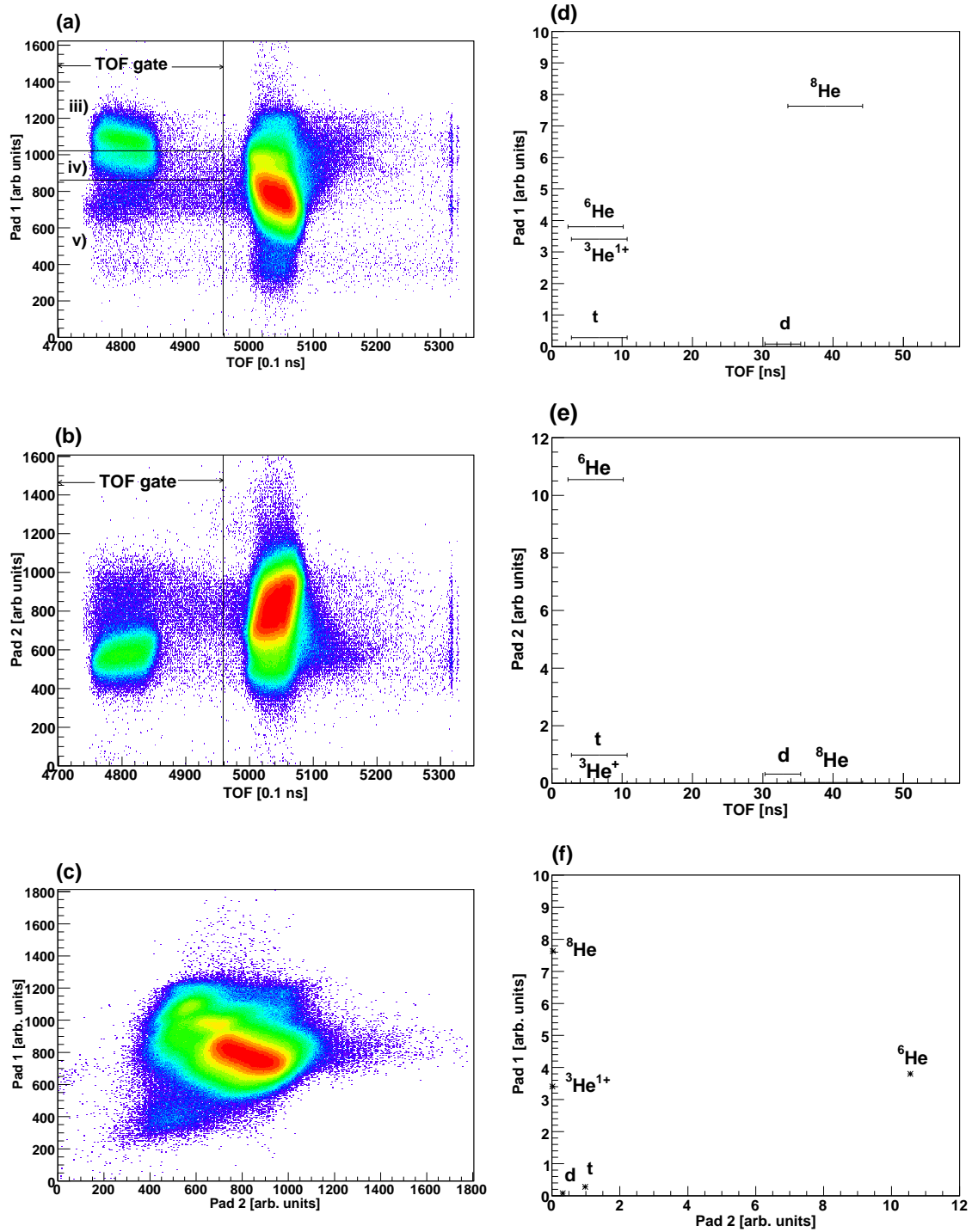


FIG. 4.35: Experimental PID spectra for the 202 MeV ${}^6\text{He}$ fieldset with a paddle setup as described in section 4.3.3 are shown in (a) - (c) on the left. The expected PID spectra for the ${}^6\text{He}$ fieldset are shown in (d) - (f) on the right.

on the low energy side. This spectrum does show a hint of a discrete structure, but it is still uncertain.

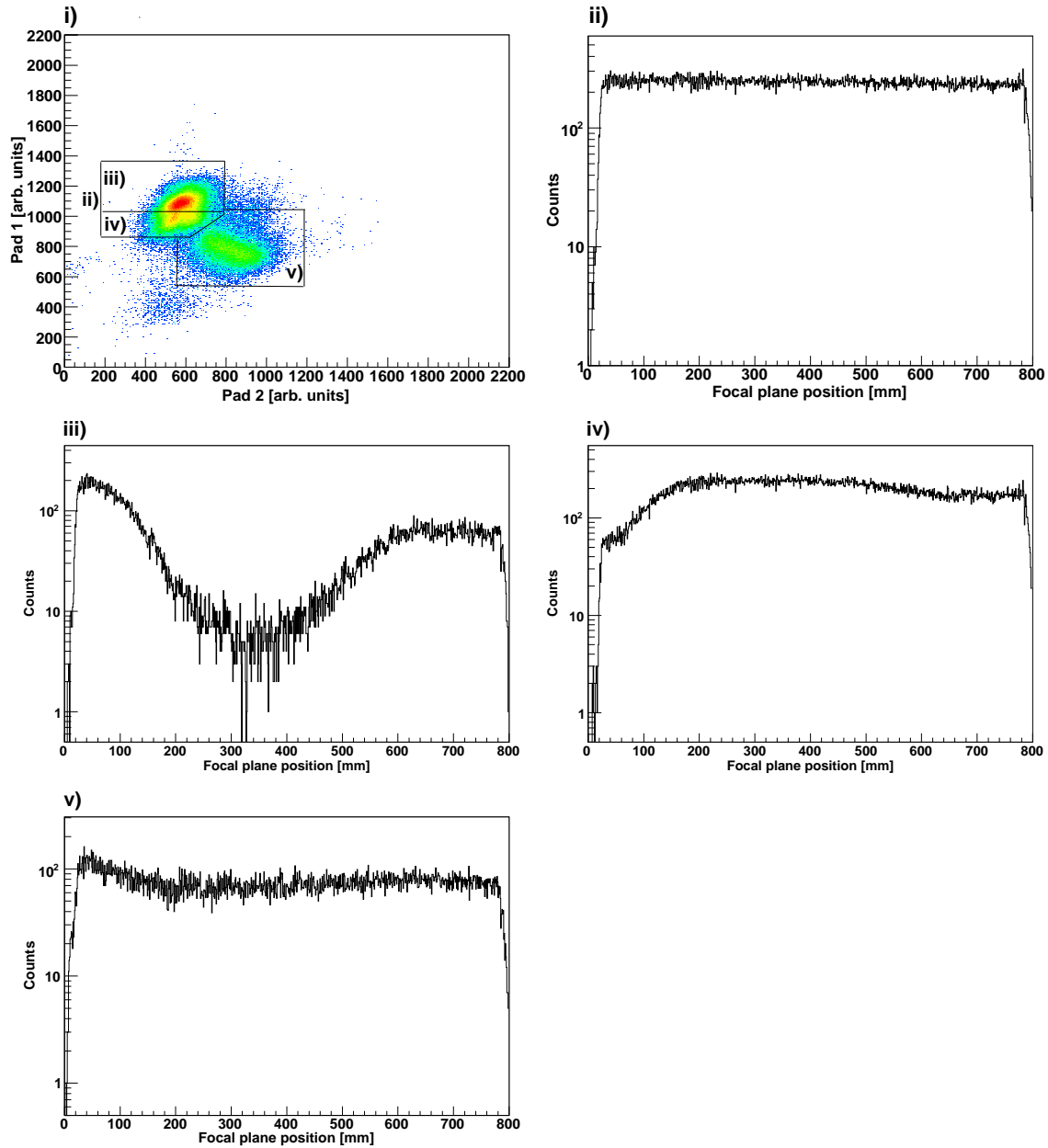


FIG. 4.36: The experimental Paddle 1 vs Paddle 2 spectrum for events that fall within the TOF gate in Fig. 4.35 is shown in i). The position spectra corresponding to the PID selection gates indicated in i) are shown in ii) - v).

Conclusive evidence of the $^{27}\text{Al}(^3\text{He},^6\text{He})^{24}\text{Al}$ reaction could not be found with either of the two paddle setups. It seems that the cross section of this reaction was too low to obtain a discrete spectrum within the beam time that was used for this measurement.

4.3.6 Analysis of the $^{27}\text{Al}(^3\text{He},^8\text{He})^{22}\text{Al}$ fieldset

The $^{27}\text{Al}(^3\text{He},^8\text{He})^{22}\text{Al}$ reaction was the original aim of the experiment and was expected to be the most difficult to measure since its cross section, which is not known but has an upper bound of $\sigma \leq 50$ pb/sr for a beam energy of $E_{lab} = 75$ MeV as mentioned in section 1.3, is lower than that of any of the other reactions that were investigated. Since the cross section for measuring the $^{27}\text{Al}(^3\text{He},^6\text{He})^{24}\text{Al}$ reaction was already too low for a successful measurement, it is unlikely that a successful measurement of the $^{27}\text{Al}(^3\text{He},^8\text{He})^{22}\text{Al}$ reaction could be made within the time that was allocated to the experiment. The measurement was performed with the optimal field settings for measuring 175 MeV ^8He particles, which are shown in Table 3.1.

Table 4.16 indicates an effective TOF range similar to that of the deuterons for ^8He . Table 4.17 indicates that ^8He has by far the highest light output in Paddle 1, but is much lower in Paddle 2. This is due to the effect of its RLO at low energies, since it loses so much energy in Paddle 1.

Data obtained from this measurement are shown in Fig. 4.37. This measurement, along with the TOF, energy loss and light output predictions shown in Tables 4.16 and 4.17, and in Fig. 4.37 (d) - (f), may be used in future attempts at measuring this reaction with the K600 magnetic spectrometer.

Particle	E range [MeV]	K range [u.MeV.C ⁻²]	TOF range [ns]	TOF range (pulse-sep) pulse sel. [ns]
^8He	160.9-189.4	321.7-378.7	120.6-130.5	4.218-14.1
d	159.8-188.1	same	64.0-68.7	5.78-10.5
t	106.7-125.6	same	92.2-99.6	34.0-41.4
$^3\text{He}^{1+}$	106.7-125.6	same	92.2-99.5	33.9-41.3

TABLE 4.16: TOF and rigidity calculations for the 175 MeV ^8He fieldset. The energy range is shown in Column 2, and the calculated rigidity for the particle of interest is shown in Column 3. Column 4 shows the calculated TOF, and Column 5 shows the TOF with the effect of overlapping taken into account.

The experimental data in Fig. 4.37 were obtained with a 10 nA beam current impinging on a 4.43 mg.cm^{-2} Al target for a duration of 62 minutes. The paddles were still perpendicular with respect to the beam direction. Pad 1 and Pad 2 were used as trigger detectors and Pad 3 as a veto detector. The loci situated at high TOF seem to wrap around in TOF in the experimental spectra. This could be expected since the calculated TOF ranges for ^3He and t are both larger than the beam pulse separation of 58.2 ns in (d) and (e). The ^8He particles could be expected around the middle of the TOF spectrum, very high in Pad 1 and lower in Pad 2. The experimental energy loss spectrum in Fig. 4.37 (c) looks very different to those measured with all the other

Particle	E into Pad1 [MeV]	Δ E _{Pad1} [MeV]	Δ E _{Pad2} [MeV]	Δ E _{Pad1} \times RLO [arb. units]	Δ E _{Pad2} \times RLO [arb. units]
^8He	117	54	44	9.02	0.0833
d	158	2	7	0.03	0.39
t	100	5	12	0.2	1.15
$^3\text{He}^{1+}$	78	34	33	3.74	0.0333

TABLE 4.17: A summary of the calculated energy loss of various particles determined by the rigidity calculations of Table 4.16. Column 2 shows the particle energy incident on Paddle 1, Columns 3 and 4 show the expected energy loss through both the paddles, and Columns 5 and 6 show the expected energy loss through the paddles with the effect of RLO taken into account.

fieldsets. Its loci have a thin and stretched-out shape, where in other fieldsets they are oval-shaped and well-defined around points in the Paddle 1 vs Paddle 2 spectrum. This is because the measurement with the ^8He fieldset was performed before the first good pulser run was obtained. At that stage of the experiment, problems were experienced with non-zero offsets of the paddle signals into the QDC.

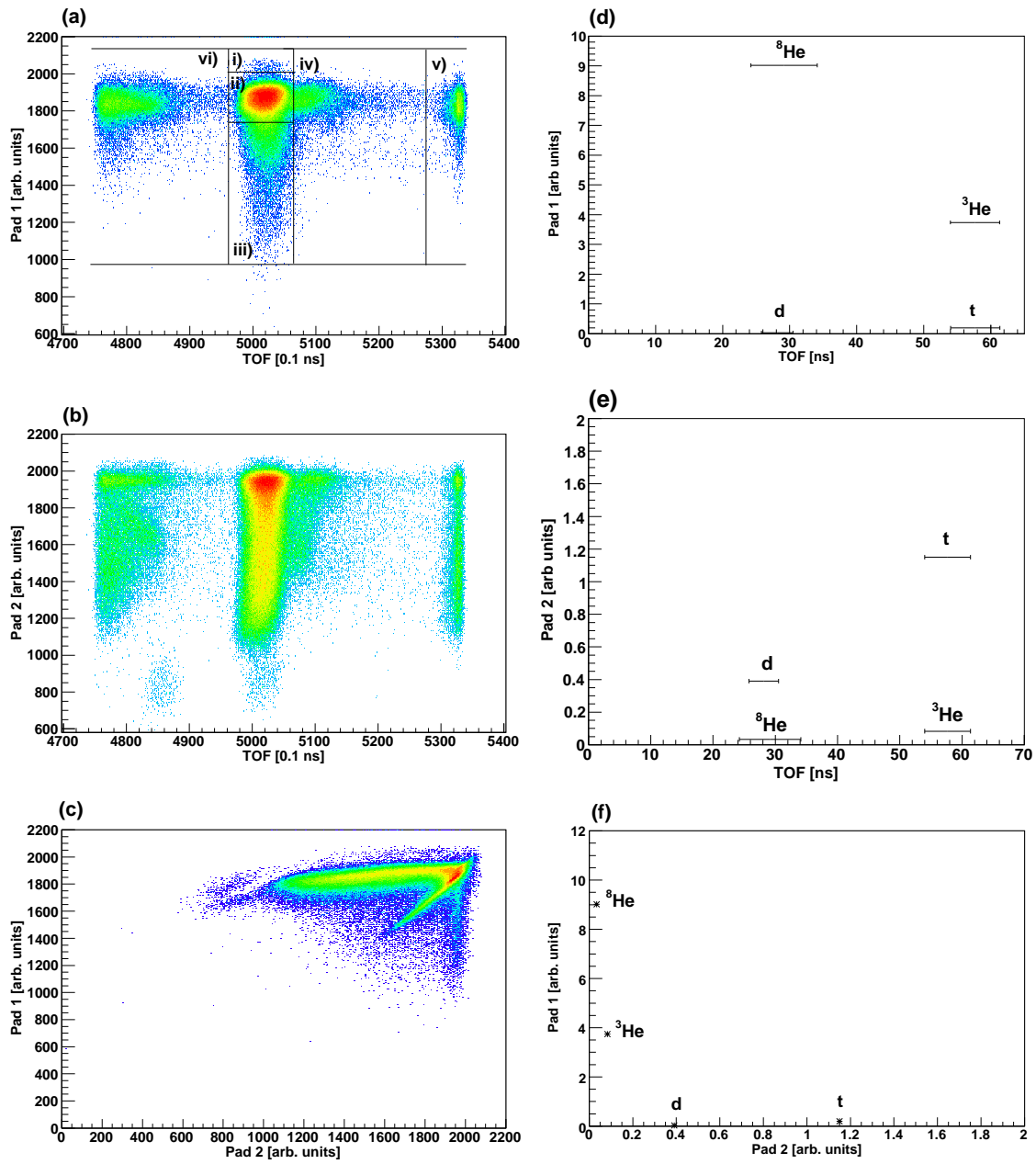


FIG. 4.37: Experimental PID spectra for the ^8He fieldset with a paddle setup as described in section 4.3.1 are shown in (a) - (c) on the left. The expected PID spectra for the ^8He fieldset are shown in (d) - (f) on the right.

The PID spectra in Fig. 4.38 are for the small locus right on top of the big locus in the middle TOF range, indicated by i) in Fig. 4.37 (a). This locus is the highest that was measured in Pad 1, but a bit lower in Pad 2. This is to be expected since ^8He loses a lot of energy in Pad 1 and its RLO is very small for low energies. One must make the assumption, however, that the effect of RLO in Pad 2 is grossly overestimated in Fig. 4.37 (e) and (f). The shape of this locus in Pad 2, with the gate applied in Pad 1, suggests that it is merely a tail of the larger deuteron locus beneath it in Pad 1. The position spectrum that was measured for this locus is shown in Fig. 4.39.

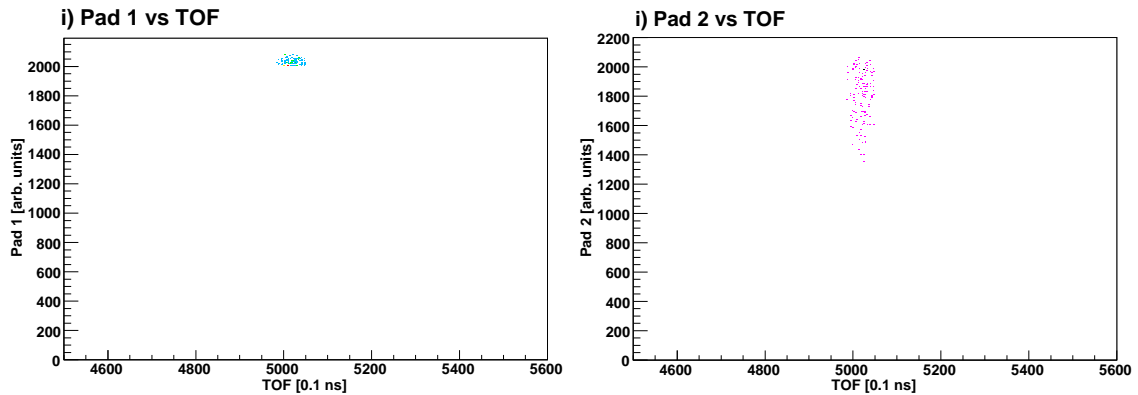


FIG. 4.38: PID spectra with TOF and paddle gates to select the most likely candidate for the $^{27}\text{Al}(^3\text{He}, ^8\text{He})^{22}\text{Al}$ reaction

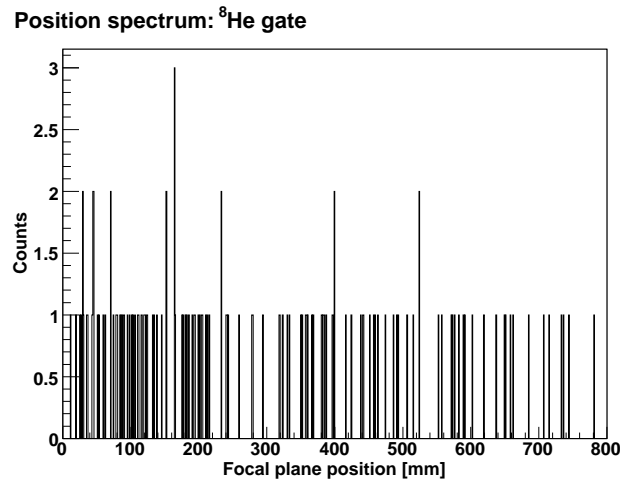


FIG. 4.39: Experimental position spectrum measured in TOF and paddle range where the $^{27}\text{Al}(^3\text{He}, ^8\text{He})^{22}\text{Al}$ reaction was expected.

The rest of the PID gates which are indicated in Fig. 4.37 (a) are investigated in Fig. 4.40. The same peak near the low energy margin that was seen with the ${}^6\text{He}$ fieldset seems to appear again in Fig. 4.40 ii), iv) and vi). There exists a possibility of discrete structure in ii), iii) and v), but no conclusive evidence of the ${}^{27}\text{Al}({}^3\text{He}, {}^8\text{He}){}^{22}\text{Al}$ reaction is to be found in any of these position spectra.

Clearly, the considerable deuteron background in the expected TOF range for ${}^8\text{He}$ is highly detrimental to the measurement of the ${}^{27}\text{Al}({}^3\text{He}, {}^8\text{He}){}^{22}\text{Al}$ reaction. The ${}^8\text{He}$ particles were predicted to have a very similar effective TOF range to the deuterons in this experiment, although their actual TOF through the spectrometer should be much longer (see Table 4.16 Columns 4 and 5). By using pulse selection of the RF signal, it is possible to increase the total TOF range measured by the detector. The ${}^8\text{He}$ particles should then be easily separable from the d particles, and a hardware veto may be applied in TOF, thus eliminating the d background from the PID spectrum.

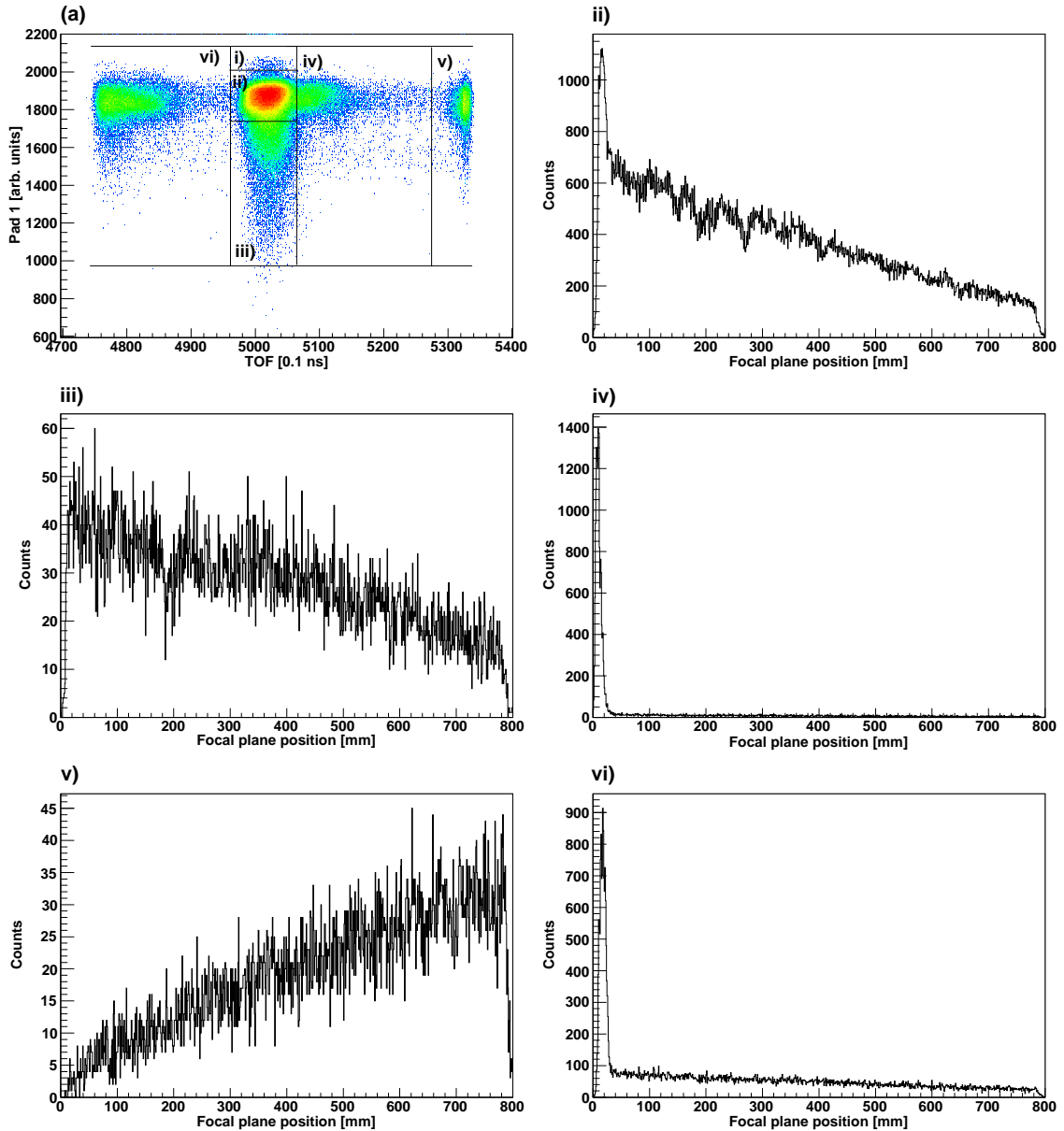


FIG. 4.40: The PID selection gates which were investigated are indicated on the experimental Paddle 1 vs TOF spectrum for the ^8He fieldset in (a). The position spectra from events that fall within these gates are shown in ii) - vi).

CHAPTER 5

Conclusion

A measurement was made to test the feasibility of using the ($^3\text{He},^8\text{He}$) reaction as a tool to populate and study neutron-deficient nuclides in the vicinity of the proton drip line with the K600 magnetic spectrometer.

This experiment employed, for the first time, a new vertical drift chamber with the U-X wire plane configuration. In addition the new data acquisition system, with VME hardware and MIDAS software, was also used for the first time on the spectrometer during this experiment.

Furthermore, this was the first experiment on the spectrometer with a ^3He beam, therefore the experimental set-up was first tested with measurements of particles with large cross sections. The particles p , d , t , ^3He and ^4He were all identified as outgoing particles from the reaction of the incident ^3He particles with the ^{27}Al target. A discrete spectrum for the $^{27}\text{Al}(^3\text{He},^6\text{He})^{24}\text{Al}$ reaction could not be identified, possibly because the cross section was too low at such a large spectrometer angle $\theta_{lab}=8^\circ$ to allow for the accumulation of enough data within the time that was taken for the measurement. Since the cross section of the $^{27}\text{Al}(^3\text{He},^8\text{He})^{22}\text{Al}$ reaction is far lower than that of the $^{27}\text{Al}(^3\text{He},^6\text{He})^{24}\text{Al}$ reaction, it came as no surprise that a clean discrete spectrum for this reaction could not be found. The main problem, however, for the measurement of the ^8He particles was the contamination from the deuterons.

Valuable experience was gained during this experiment with the ^3He beam, and with the measurement and identification of various particles of interest with the magnetic spectrometer. The data which were measured and the predictions which were made (for energy loss and TOF) can be used as a reference for future ventures with He beams on the K600.

In the short term, this experiment may be attempted again with the same experimental setup and employing pulse selection of the RF signal to veto the d background in the ^8He fieldset by means of TOF. In the medium term it is suggested that a similar experiment, this time with a ^4He beam, could be performed since it is expected that two-neutron and four-neutron pick-up reactions will be easier to measure than three- and five-neutron pick-up reactions, due to the effect of pairing energies. In the long term, the same experiment may be repeated with the 0° mode of the K600 spectrometer, to detect the ^8He particles where the cross section is higher.

Theoretical mass calculations for some drip line nuclei were performed using the quadratic Isobaric Multiplet Mass Equation (IMME). Their results proved more favourable for odd nuclei than for even nuclei. The most probable reason for this is that no pairing energy term is included in the quadratic IMME. Predictions were made for some odd nuclei which have not been measured

yet in the vicinity of the proton drip line.

6 Bibliography

- [1] National Nuclear Data Center, Brookhaven National Laboratory, <http://www.nndc.bnl.gov/nudat2/>, (2009).
- [2] R. Kouzes, Nucl. Phys. **A286**, 253 (1977).
- [3] H. Staub *et al.*, in *Experimental Nuclear Physics*, edited by E. Segrè (John Wiley & Sons, Inc., New York, 1953), Vol. I.
- [4] A. Beiser, in *Concepts of Modern Physics*, 6th ed., edited by I. Berg (McGraw Hill, New York., 2003).
- [5] K. Heyde, in *Basic Ideas and Concepts in Nuclear Physics: An Introductory Approach*, 3rd ed., edited by R. Betts and W. Greiner (Institute of Physics Publishing, Bristol, UK., 2004).
- [6] S. S. M. Wong, *Introductory Nuclear Physics*, 2nd ed. (Wiley-VCH Verlag, Weinheim, 2004).
- [7] K. Langanke, Nuclear Astrophysics Part I, Chris Engelbrecht Summer School for Theoretical Physics, STIAS, Stellenbosch, <http://academic.sun.ac.za/somerskool/2009.html>, (2009).
- [8] C. Detráz and D. J. Vieira, Annu. Rev. Nucl. Part. Sci. **39**, 407 (1989).
- [9] A. G. Artukh *et al.*, Nucl. Phys. **A176**, 284 (1971).
- [10] V. Volkov, in *Proc. Int. Conf. on Nuclear Physics, Munich*, edited by J. de Boer and H. J. Mang (North-Holland, Amsterdam, 1972).
- [11] P. Auger *et al.*, Z. Phys. **A289**, 255 (1979).
- [12] D. Guerreau *et al.*, Z. Phys. **A295**, 105 (1980).
- [13] H. Breuer *et al.*, Phys. Rev. C **22**, 2454 (1980).
- [14] J. Gorres, J. Res. Nat. Inst. Stand. Technol. **105**, 101 (2000).
- [15] H. Schatz, Phys. Rev. Lett. **79**, 3845 (1997).

- [16] E. Roeckl, Nucl. Phys. **A488**, 95c (1988).
- [17] A. C. Mueller, An Overview of Radioactive Beam Facilities, Proc. 7th European Particle Accelerator Conference, Vienna, Austria, (2000).
- [18] C. Thibault *et al.*, Phys. Rev. C **12**, 644 (1975).
- [19] X. Campi, H. Flocard, A. K. Kerman, and S. Koonin, Nucl. Phys. **A**, 193 (1975).
- [20] C. Detráz, Proc. 4th Int. Conf. on Nuclei Far From Stability, Helsingor, (1981).
- [21] W. Nazarewicz, Nuclei as open quantum many body systems, Chris Engelbrecht Summer School for Theoretical Physics, STIAS, Stellenbosch, <http://academic.sun.ac.za/somerskool/2009.html>, (2009).
- [22] H. T. Fortune and R. Sherr, Phys. Rev. C **76**, 014313 (2007).
- [23] A. S. Jensen and A. Miranda, Nucl. Phys. **A449**, 331 (1986).
- [24] D. G. Madland and J. R. Nix, Nucl. Phys. **A476**, 1 (1988).
- [25] P. Möller and J. R. Nix, At. Data Nucl. Data Tables **39**, 213 (1988).
- [26] G. A. Leander and Y. S. Chen, Phys. Rev. C **37**, 2744 (1988).
- [27] I. Mukha *et al.*, Phys. Rev. Lett. **99**, 182501 (2007).
- [28] V. I. Goldansky, Nucl. Phys. **19**, 482 (1960).
- [29] M. Pfutzner *et al.*, Eur. Phys. J. A **14**, 279 (2002).
- [30] J. Giovinazzo *et al.*, Phys. Rev. Lett. **89**, 102501 (2002).
- [31] B. Blank *et al.*, Phys. Rev. Lett. **94**, 232501 (2005).
- [32] I. Mukha *et al.*, Nature **439**, 298 (2006).
- [33] L. V. Grigorenko *et al.*, Phys Rev. C **80**, 034602 (2009).
- [34] G. Canchel *et al.*, Eur. Phys. J. A **12**, 377 (2001).
- [35] P. Papka, Investigation of the ($^3\text{He}, ^8\text{He}$) reaction, Research proposals to iThemba LABS, (2007).
- [36] L. V. Grigorenko *et al.*, Phys. Rev. Lett. **85**, (2000).

- [37] P. Papka, private communication.
- [38] P. E. Hodgson, E. Gadioli, and E. Gadioli Erba, *Introductory Nuclear Physics* (Oxford University Press, Oxford, 2000).
- [39] R. Kouzes and W. H. Moore, *Phys. Rev. C* **12**, 1511 (1975).
- [40] V. Z. Gol'dberg, A. A. Ogloblin, and V. P. Rudakov, *Soviet J. Nucl. Phys.* **9**, 10 (1969).
- [41] V. Guimarães *et al.*, *Phys. Rev. C* **67**, 064601 (2003).
- [42] R. E. Tribble, *Phys. Rev. Lett.* **40**, 13 (1978).
- [43] R. G. H. Robertson, *Phys. Rev. Lett.* **32**, 1207 (1978).
- [44] G. Berg *et al.*, private communication.
- [45] W. Heisenberg, *Z. Phys.* **77**, 1 (1932).
- [46] W. E. Ormand, *Acta Physica Polonica B* **29**, 1 (1998).
- [47] E. P. Wigner, *Phys. Rev.* **51**, 106 (1937).
- [48] W. Greiner and B. Müller, *Quantum Mechanics: Symmetries*. (Springer-Verlag, Amsterdam, 1989).
- [49] D. H. Wilkinson, The Isobaric Mass Formula and Coulomb Energies in the 1p-Shell, *Proc. Conf. on Isobaric Spin in Nuclear Physics*, Tallahassee, Florida, (1966).
- [50] J. Jänecke, *Phys. Rev.* **147**, 735 (1966).
- [51] J. Jänecke, *Nucl. Phys. A* **128**, 632 (1969).
- [52] E. P. Wigner, *Proc. 1st Robert A. Welch Found. Conf. Chem. Res.*, Houston, Texas, (1957).
- [53] J. Britz, A. Pape, and M. S. Antony, *At. Data Nucl. Data Tables* **69**, 125 (1998).
- [54] ROOT Version 5.19/03, <http://root.cern.ch>.
- [55] I. Mukha *et al.*, *Phys. Rev. C* **77**, 061303 (2008).
- [56] P. Papka *et al.*, *Phys. Rev. C* **75**, 045803 (2007).
- [57] L. V. Grigorenko *et al.*, *Phys Lett. B* **677**, 30 (2009).

- [58] The iThemba LABS website, <http://www.tlabs.ac.za/public/default.htm>, (2009).
- [59] The Midas Data Acquisition System, Paul Sherrer Institute, Switzerland, <https://midas.psi.ch>, (2009).
- [60] Chemgas, <http://www.chemgas.com>, boulogne, France.
- [61] G. P. A. Berg, C. C. Foster, E. J. Stephenson, and B. F. Davis, K600 Transmission Mode for 0 degree Inelastic Scattering, IUCF Annual Report, (1994), 106.
- [62] H. E. Wegner *et al.*, in *Nuclear and Particle Physics Source Book*, edited by S. Parker (McGraw-Hill, New York, 1987).
- [63] D. L. Hendrie, Nucl. Spectroscopy and Reactions **A**, 365 (1974).
- [64] R. Neveling, Master's thesis, University of Stellenbosch, (1998), unpublished.
- [65] H. A. Enge and J. E. Spencer, Nucl. Instr. Meth. **49**, 181 (1967).
- [66] R. Neveling, F. D. Smit, H. Fujita, and R. T. Newman, Guide to the K600 Magnetic Spectrometer, unpublished, (2009).
- [67] W. Bertozzi *et al.*, Nucl. Instr. Meth. **141**, 457 (1977).
- [68] The Ganil website, <http://www.ganil-spiral2.eu/>, (2006).
- [69] J. F. Ziegler, Nucl. Instr. Meth. **B 219**, 1027 (2004).
- [70] Stesalit AG Kunststoffwerk, <http://www.stesalit.com>, cH-4234 Zullwill SO, Switzerland.
- [71] K. G. Fissum *et al.*, Nucl. Instr. Methods **A474**, 108 (2001).
- [72] R. T. Newman, Ph.D. thesis, University of Cape Town, (1996), unpublished.
- [73] R. Veenhof, GARFIELD, A Drift-chamber simulation program: User's Guide Version 5.18, Internal Report, CERN, unpublished), (1995).
- [74] R. Neveling, K600 website, <http://www.k600.tlabs.ac.za>, (2009).
- [75] R. Bouclier *et al.*, Nucl. Instr. Meth. **88**, 149 (1970).
- [76] Saint Gobain Crystals, <http://www.detectors.saint-gobain.com>, (2009).
- [77] G. de Villiers, Spexcit, iThemba LABS, (2009).

- [78] G. F. Knoll, Radiation Detection and Measurement, 3rd Edition, John Wiley and Sons, Hoboken, USA, (2000).
- [79] A. Breskin *et al.*, Nucl. Instr. Meth. **119**, (1974).
- [80] P. Jipsen and J. Maritz, Program ELOSS V2.0, iThemba LABS (1992), *z* H. Andersen and J. F. Ziegler, The Stopping and Ranges of Ions in Matter, Volumes 3, 4 and 5, Pergamon Press, New York (1977).
- [81] S. S. Dietrich and B. L. Berman, At. Data Nucl. Data Tables **38**, 199 (1988).
- [82] Y. Fujita, Y. Shimbara, and T. Adachi, Phys. Rev. C **70**, 054311 (2004).